

## Forces and symmetries in cells and tissues Eckert, J.

#### Citation

Eckert, J. (2022, December 6). Forces and symmetries in cells and tissues. Casimir PhD Series. Retrieved from https://hdl.handle.net/1887/3492626

Version: Publisher's Version

Licence agreement concerning inclusion of doctoral

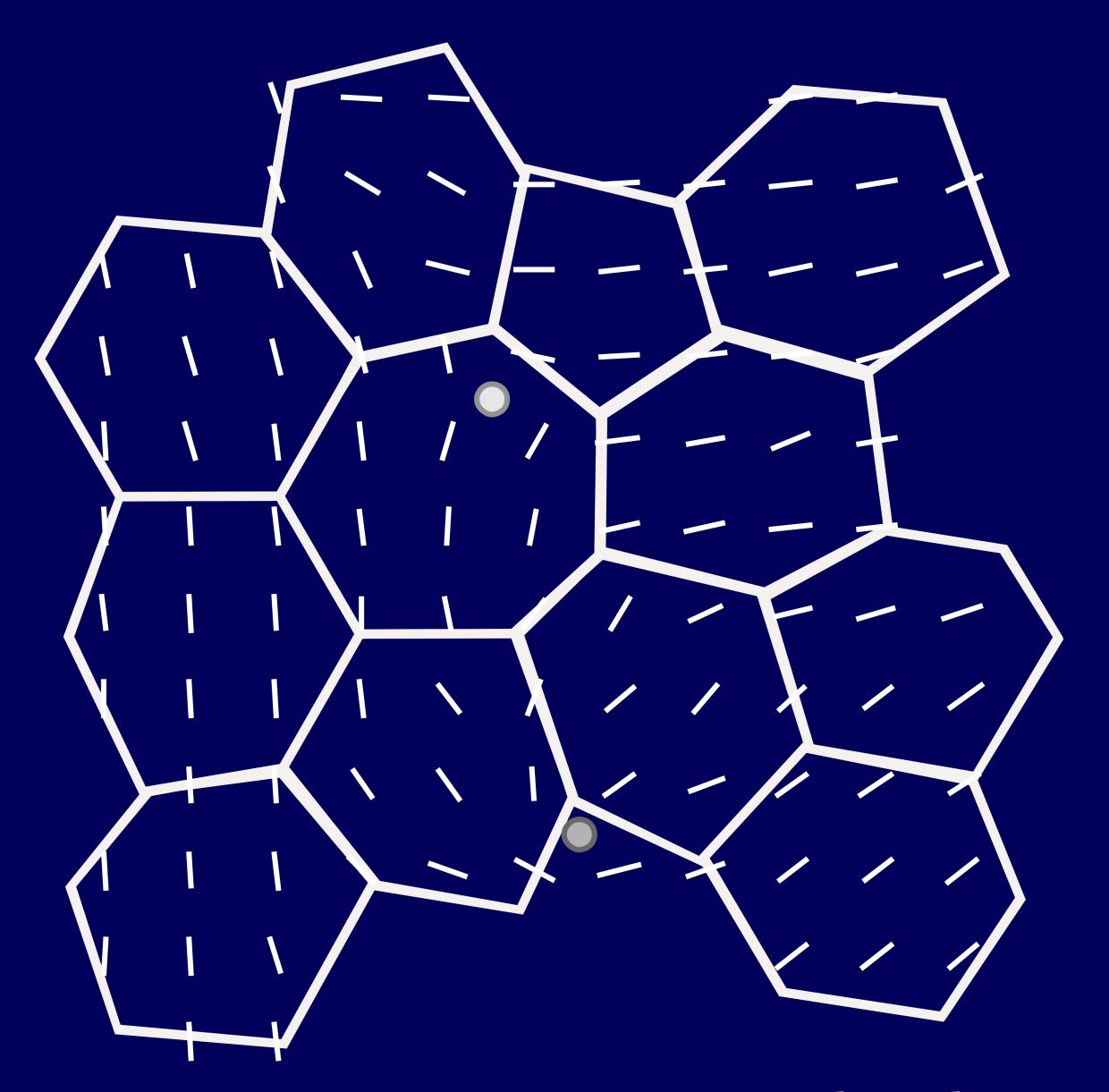
License: thesis in the Institutional Repository of the University of

Leiden

Downloaded from: https://hdl.handle.net/1887/3492626

**Note:** To cite this publication please use the final published version (if applicable).

# Forces and Symmetries in Cells and Tissues



Julia Eckert

## Forces and Symmetries in Cells and Tissues

Julia Eckert

## Forces and Symmetries in Cells and Tissues

#### Proefschrift

ter verkrijging van de graad van doctor aan de Universiteit Leiden, op gezag van rector magnificus prof.dr.ir. H. Bijl, volgens besluit van het college voor promoties te verdeding op dinsdag 6 december 2022 klokke 10.00 uur

door

Julia Eckert

geboren te Dresden, Duitsland in 1991

Promotor: Prof. dr. T. Schmidt

Promotiecommissie: Dr. M. Gloerich (UMC Utrecht)

Dr. B. Ladoux (DR CNRS, Institut Jacques Monod)

Prof. dr. J. Aarts

Prof. dr. ir. S.J.T. van Noort Prof. dr. B.E. Snaar-Jagalska

@2022 by J. Eckert. All rights reserved.

Cover: Polygonal shape of cells in a monolayer. The front cover shows the nematic director field as rods superimposed to the apical part of cells, forming two topological defects represented as dots. After moving the focus through all pages of this thesis, the back cover ends with the basal part of the monolayer in which actin stress fibers are connected to micropillars.

Casimir PhD Series, Delft-Leiden, 2022-28 ISBN 978-90-8593-536-0 An electronic version of this thesis can be found at https://openaccess.leidenuniv.nl The only source of knowledge is experience.

- Albert Einstein -

### Contents

O	utline	e of this thesis	1
1	Hole	ding it together: when cadherin meets cadherin	3
	1.1	Introduction	5
	1.2	The toolbox of adhesion	6
		1.2.1 Biological components of cell-cell adhesion	6
		1.2.2 Mechanical characterization of cell-cell adhesion	8
	1.3	Cell-cell contact formation: from molecules to cells and tissues	10
		1.3.1 The role of molecular interactions over the contact .	11
		1.3.2 The role of intercellular forces arising at the contact	13
		1.3.3 The role of interfacial tension in cell aggregates	16
	1.4	Conclusion and perspectives	20
2	Sing	gle cell micro-pillar-based characterization of endothe-	
	-	-	33
	2.1	Introduction	35
	2.2	Results	36
		2.2.1 Endothelial cells apply less traction forces compared	
			36
		2.2.2 Averaged force dipole distribution is independent of	07
		0.1	37
	0.0		38
	2.3		39
	2.4	Materials and methods	40
3	Cell	l-Cell Separation Device: measurement of intercellular	
	deta	achment forces	<b>49</b>
	3.1	Introduction	51
	3.2	Results	52
		3.2.1 The intercellular adhesion strength increases with an	
		increase of the total traction force	52
		3.2.2 Stretching a homogeneous elastic micropillar field cau-	
		ses deformations	53

Publications 1				151
				149
				141
Sa	men	vatting	g	135
Sι	ımm	ary		129
	5.5	Supple	ementary	119
	5.4		ials and methods	116
	5.3		ssion and conclusion	115
			of the hexatic order driven by cell-matrix and cell-cell adhesions	113
		5.2.5	nolayer density	111
		5.2.4	crossover towards small length scales	110
		5.2.2 5.2.3	Hexagonality in epithelia increases with density The absence of E-cadherin shifts the hexanematic	108
		<b>.</b>	and decreases the monolayer density	106
		5.2.1	Reduced cell-cell adhesion increases the shape index	
	5.2		ts	106
	5.1		luction	105
5			atic crossover in epithelial monolayers depends o ion and cell density	n 103
_	тт.			
			Defect representation in $p$ -atic liquid crystals	94
	4.4		ementary	89 89
	4.3		ials and methods	84
	4.2		ssion and conclusion	83
	4.1		luction and results	77
4	_		are multiscale active liquid crystals	<b>75</b>
	3.5	Supple	ementary	65
	3.4	Mater	ials and methods	61
	3.3	Discus	ssion and conclusion	60
		3.2.3	CC-SD: the Cell-Cell Separation Device	55

### Outline of this thesis

The way organisms develop from the initial single-cellular state to a complex final assembly like the human body, and how the final body is maintained throughout life, is one of the greatest mysteries and it's understanding one of the biggest scientific challenges. What has been surprising in the last decade is that the initial assembly and also later maintenance of integrity is not only determined by intricate biochemical communication networks, but in part by physical forces that cells, their neighbors, and their environment apply in a bidirectional manner. The resulting collectivity of cells determines the development of organisms and are crucial to the health and disease state of the organism.

In this thesis, we develop and utilize concepts from physics to quantitatively understand forces that develop between cells and their environment and neighboring cells, and how the interplay between these forces regulates the arrangement, shape, and topology of tissue. These topics range from the development of novel experimental methods to the combination of experimental observations with theoretical descriptions. Thus, this thesis is at the interface of physics and biology, for which we collaborated with groups from both fields. Our results contribute to a better understanding of cell and tissue integrity.

Chapter 1 reviews the current knowledge about cell-cell adhesion from the molecular and cellular level to tissue and organs. The central focus is set on finding a common base for understanding the biological and physical principles of cell-cell adhesion. This chapter covers a description of the molecular interaction between cells and describes the role of intracellular signaling processes. The chapter appeared as a scientific review article written in a collaboration with the Heisenberg lab in Klosterneuburg (ISTA, Austria).

In **Chapter 2**, we compare the mechanics of single endothelial and fibroblast cells. Using elastic micropillar arrays, we study differences in traction forces of both cell lines. Comparing the morphology-dependent force distribution, we find that endothelial cells exert less traction forces

on substrates and tend to be more circular in their morphology with a broader force distribution when compared to fibroblasts. This study is conducted in collaboration with the Mashaghi lab in Leiden (LACDR, Leiden University).

In **Chapter 3**, we develop a novel methodology to measure the maximum intercellular adhesion force between two cells adhered to a substrate. We name our design the Cell-Cell Separation Device (CC-SD). The CC-SD makes it possible to separate cells in doublet configurations while simultaneously measuring the traction forces, and hence the modulation of intercellular forces. It allows us to get information about the maximum resistance against detachment of cells in tissues. For this project, we collaborate with Stefan Partel and his team in Dornbirn (FHV, Austria).

In **Chapter 4**, we describe the methodology to study the symmetry of tissues by combining *in vitro* experiments with numerical simulations. By detecting the orientational order of cells in monolayers, we identify that the nematic and hexatic order in epithelial monolayers coexist at different length scales. Cells are hexatic at small length scales, changing to nematic at larger length scales. This novel description creates the basis for a correct identification of topological defects, which were identified as location of biological functionality. The project is performed in collaboration with the Giomi group in Leiden (LION, Leiden University).

In Chapter 5, we study the hexatic and nematic symmetry of epithelial monolayers as a function of the cell-cell adhesion, monolayer density, and the influence of the underlying substrate stiffness. We find that the crossover from the dominant hexatic order at short length scales to the nematic one at larger length scales strongly depends on the monolayer density and is affected by the cell-cell adhesion. Our results indicate that the length scale of the crossover is controlled by the interplay of the cell-matrix and cell-cell adhesion in confluent monolayers. The work resulted from a collaborative project with Ladoux - Mège lab in Paris (Institut Jacques-Monod, France) and Luca Giomi in Leiden (LION, Leiden University).

## Holding it together: when cadherin meets cadherin

Intercellular adhesion is the key to multicellularity, and its malfunction plays an important role in various developmental and disease-related processes. Although it has been intensively studied by both biologists and physicists, a commonly accepted definition of cell-cell adhesion is still being debated. Cell-cell adhesion has been described at the molecular scale as a function of adhesion receptors controlling binding affinity, at the cellular scale as resistance to detachment forces or modulation of surface tension, and at the tissue scale as a regulator of cellular rearrangements and morphogenesis. In this review, we aim to summarize and discuss recent advances in the molecular, cellular, and theoretical description of cell-cell adhesion, ranging from biomimetic models to the complexity of cells and tissues in an organismal context. In particular, we will focus on cadherin-mediated cell-cell adhesion and the role of adhesion signaling and mechanosensation therein, two processes central for understanding the biological and physical basis of cell-cell adhesion.

Arslan, F. N., **Eckert, J.**, Schmidt, T., and Heisenberg, C.-P. (2021). Holding it together: when cadherin meets cadherin. *Biophysical Journal* 120, 4182-4192.

1.1 Introduction 5

#### 1.1 Introduction

The basic unit of living systems is the cell, which gives rise to unicellular colonies and multicellular organisms. In multicellular organisms, cells are assembled into tissues (1), the formation of which depends on cell-cell adhesion complexes that couple cells to each other. Cell-cell adhesion plays essential roles in organismal development and homeostasis, such as tissue compaction (2), cell sorting (3), and cell migration (4), and misregulation of cell-cell adhesion is a hallmark of many developmental disorders and diseases (5-7).

Specific cell-cell adhesion receptors help two cells to interact and recognize each other (8). Among them, the cadherin family of cell-cell adhesion receptors was most intensively studied in the past and was shown to be essential for the formation and maintenance of tissues in countless organisms (9). Cadherins function by mechanically coupling cells to each other and modulating a wide array of effector processes that range from the regulation of the cytoskeleton to gene expression. Cadherin adhesion complexes typically consist of hundreds of proteins, some of which change their conformation and stoichiometry under mechanical stress, thereby linking the interacting surfaces of cells to their cytoskeleton and giving cells the ability to sense and respond to extracellular and intracellular signals (10).

Cell-cell adhesion is a complex and dynamic process. For years, physicists have been trying to measure and model cell-cell contacts, and biologists have identified new components, functions, and regulators of the cell-cell adhesion machinery. This led to various descriptions and interpretations of cell-cell adhesion as, for instance, the adhesion energy of molecular interactions at adhesive interfaces (11, 12) or the resistance to cell-cell detachment forces (13, 14). Moreover, adhesion-mediated cell-cell contact formation was proposed to be driven by the balance of interfacial/surface tensions, which again depend on tension exerted by the actomyosin cortex and its modulation via adhesion receptor signaling and the binding of adhesion molecules over the contact (15–18). In this review, we will summarize and discuss recent progress in defining cell-cell adhesion at multiple scales by both experiment and theory, predominantly focusing on the role of classical cadherins (generally referred to as cadherins) therein.

#### 1.2 The toolbox of adhesion

#### 1.2.1 Biological components of cell-cell adhesion

#### Cadherin adhesion complex

Cadherin adhesion complexes are protein assemblies consisting of cadherin adhesion receptors and their cytoplasmic interactors, such as catenins (19). Classical cadherins, such as E-cadherin (cdh1) and N-cadherin (cdh2), consist of an ectodomain of five repetitive extracellular cadherin (EC) subdomains with rigidity-providing Ca<sup>2+</sup>-binding pockets in between those domains, a single-pass transmembrane domain, and a cytoplasmic tail. The ectodomains of cadherins of opposing cells interact by binding in trans over the contact, first by engaging in EC1-EC2 interactions, leading to the formation of intermediate fast binding X-dimers, followed by strand swapping to form the so-called S-dimers. Cadherins also interact in *cis* with other cadherins on the same cell surface, a process important for cadherin clustering (20, 21). Intracellularly, the cadherin cytoplasmic tail interacts with adaptor proteins, such as p120- and β-catenins. They directly bind to subdomains in the cadherin tail and recruit other molecules, such as  $\alpha$ -catenins, which, by binding to filamentous actin (F-actin), connect cadherins to the actomyosin cytoskeleton (10). As new contacts form, cadherins, catenins, and hundreds of other components and interaction partners of the cadherin adhesion complex get recruited to the contact (19), where they control the establishment, strength, and stability of the contact by regulating cadherin clustering, turnover, and cytoskeletal anchoring. The cadherin adhesion complex also regulates downstream signaling mediators, which again modulate cytoskeletal organization and other cellular functions.

#### Actin cortex

The actin cortex is a thin, contractile F-actin network tethered to the plasma membrane shaping animal cells. The actin cortex can readily adapt to the microenvironment by rapidly turning over. Besides actin, the cortex contains various actin-binding proteins, such as actin nucleators (e.g., Arp2/3 and formins), which assemble and disassemble the F-actin network, actin cross-linkers, and motor proteins (most prominently myosin II), which can both pull and cross-link actin filaments. The coaction of these different proteins regulates the actin network architecture and function, thereby defining the mechanical properties of the cortex (22).

#### Cell membrane

The cell membrane (plasma membrane) is a phospholipid bilayer surround-

ing the cell, and forms the border between the interior and exterior of the cell. The cell membrane has a dynamically changing heterogeneous composition and structure. In particular, transient nanodomains of distinct lipid compositions were proposed to function as organizational hubs for recruiting proteins and thereby spatially restricting and modulating their activity (23, 24).

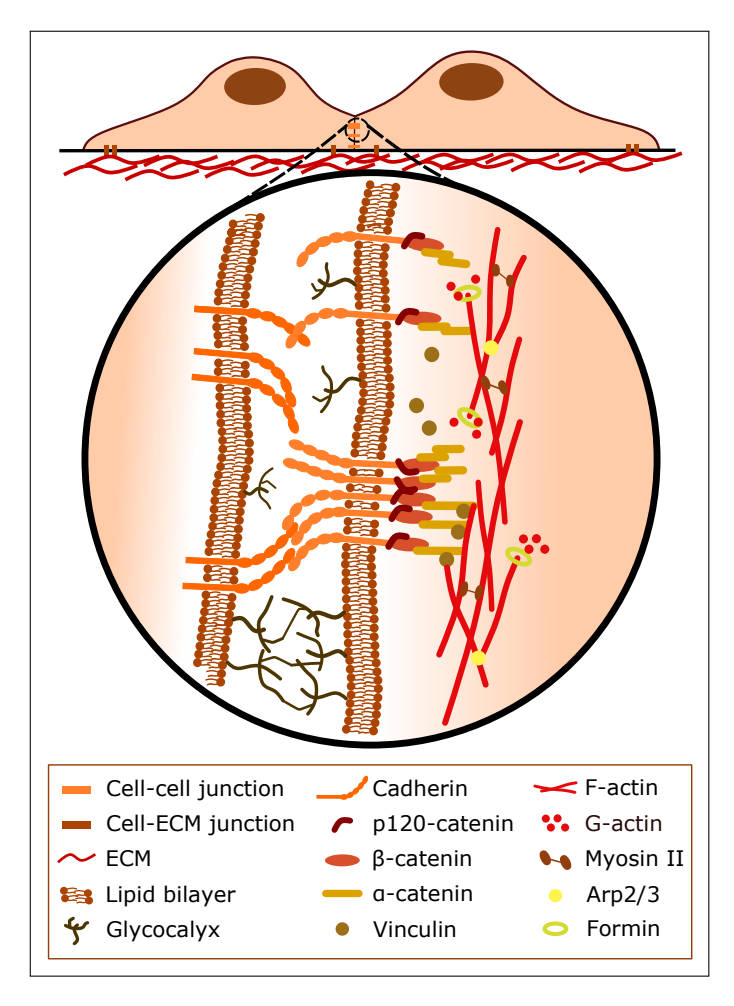


Figure 1.1: Cells can undergo adhesions with other cells and the extracellular matrix (ECM) via junctions. Cadherins mediate specific cell-cell adhesions via trans interactions in the extracellular space, where glycocalices act as a repulsive barrier. Cadherins indirectly bind to the underlying actomyosin cortex via  $\beta$ - and  $\alpha$ -catenins. Mechanosensitive cadherin adhesion complexes can change their binding strength to the actin cortex by cis clustering and by recruiting adaptor proteins such as vinculin. These complexes can also lead to local changes in actomyosin contractility by regulating the architecture of the cortex.

#### Glycocalyx

The glycocalyx (pericellular matrix) is a carbohydrate-rich meshwork covering the cell membrane and consisting primarily of glycopolymer chains decorated with bulky glycoproteins. Depending on the cell type, the glycocalyx can extend up to several micrometers from the cell membrane (25) and is thought to modulate cell-cell adhesion by physically keeping the cell membranes (and adhesion molecules therein) of adjacent cells at a distance.

#### Extracellular matrix

The extracellular matrix (ECM) is a three-dimensional network composed of proteoglycans (proteins with polysaccharide chains), fibrous proteins, and water, which is locally secreted by cells, connecting and surrounding them. The ECM supports cells structurally and regulates their activities. Cell-ECM adhesion is mediated through ECM receptors, mainly integrins (26).

#### Junctions

Junctions are cellular structures/multiprotein complexes that connect neighboring cells or cells with the ECM and are connected through adaptor proteins to the cytoskeleton (8). Most common cell-cell junctions are adherens junctions (containing cadherins), tight junctions, and gap junctions. Junctions experience mechanical forces and can convert those into biochemical signals in a process called mechanotransduction, which leads to changes in cell signaling and adhesion (Fig.1.1; (14)).

#### 1.2.2 Mechanical characterization of cell-cell adhesion

#### Mechanical stress

Mechanical stress (Pascal, Pa) is equivalent to the force per surface area (Newton per square meter,  $N/m^2$ ) on an object applied by a neighboring object. At intercellular contacts, tensile stress and compressive stress act normally to the contact area. Tensile stress occurs when cells are pulled away from each other (Fig.1.2A), whereas compressive stress exists when cells are squeezed toward each other. In comparison, shear stress arises when forces act parallel to the contact area, as in the case of cells that move alongside each other. Furthermore, mechanical stress is equal to the mechanical energy per volume (Joule per cubic meter,  $J/m^3$ ).

#### Cortical tension

Cortical tension (Joule per square meter,  $J/m^2$ ) is the tension generated mainly by myosin motors contracting the thin actin cortex coupled to the

cell membrane (27). Cortical tension is modulated by the composition and architecture of the actin cortex (22). Cortical tension must be in balance with the internal cellular pressure, thereby together controlling the cell shape. Cortical tension tends to decrease the surface and the contact area of a cell (Fig.1.2B).

#### Surface tension

Analogous to water droplets, the surface tension (Joule per square meter,  $J/m^2$ ), as energy per surface area, acts to minimize the surface area of cells (28). Cortical tension together with the typically lower tension of the plasma membrane are the main regulators of cell surface tension. The concept of surface tension can also be applied to describe the mechanical properties of tissues. An aggregate of cells develops tissue surface tension, resulting from the difference in adhesion between cells of the aggregate and their surroundings (Fig.1.3; (3)).

#### Cell-cell interfacial tension

Cell-cell interfacial tension (Joule per square meter,  $J/m^2$ ) is the tension that is developed between two cells, described by the energy per contact area. The cell-cell interfacial tension is increased by the cortical tension, which shrinks the contact area, and decreased by adhesion tension because of the binding of adhesion molecules, which increases the contact area (Fig.1.2B; (18, 29)).

#### Adhesion tension

Adhesion tension (Joule per square meter,  $J/m^2$ ) is the total energy per unit area released when two cells come into contact (Fig.1.2B). The total adhesion energy (Joule, J) is given by the integral of the adhesion tension on the interaction area. Sometimes, the adhesion energy is translated as the detachment force (Newton, N), which determines the total work (Newton meter, Nm) needed to separate two objects.

#### Cellular traction forces

Cellular traction forces (Newton, N) are in-plane pulling forces applied by adherent cells on substrates. They are generated by actomyosin contraction transmitted through the cell-matrix adhesion complexes to the ECM.

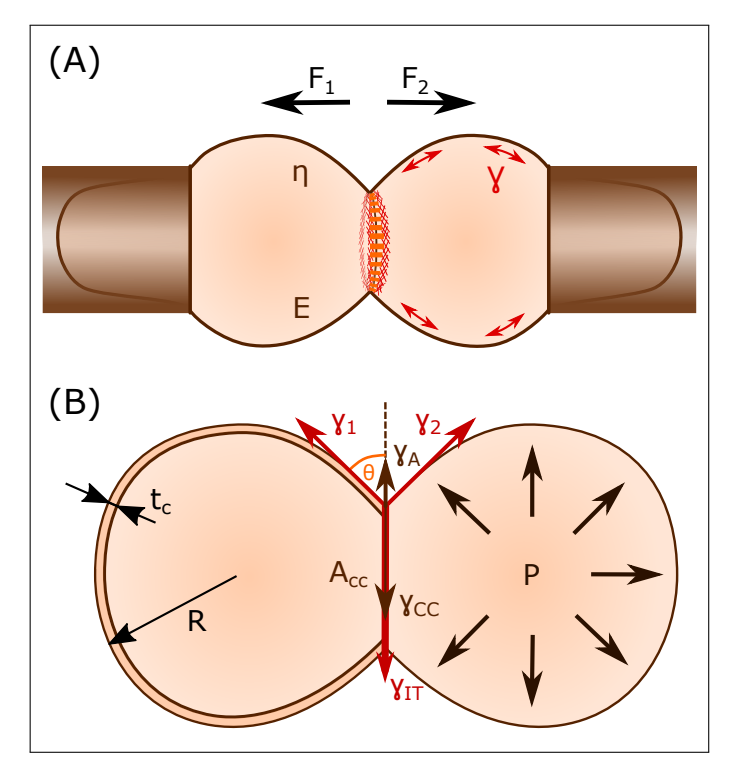


Figure 1.2: (A), A schematic representation of dual pipette aspiration (DPA) is shown. Applied detachment forces,  $F_1 + F_2$ , on suspended cells with a given viscoelasticity (viscosity,  $\eta$ , and Young's modulus, E) forming a contact, where E-cadherin and actin accumulate at the contact rim. (B), Radius, R, and the cortex thickness,  $t_C$ , define the cortical tensions,  $\gamma_1$  and  $\gamma_2$ , of the connected cells. For  $\gamma_1 = \gamma_2 = \gamma$ , cortical tensions at the contact-free area are counteracted by the interfacial tension,  $\gamma_{IT} = 2 \cdot \gamma \cdot \cos(\theta)$ , at the cell-cell adhesion area,  $A_{CC}$ . The interfacial tension,  $\gamma_{IT}$ , is determined by the difference in magnitude between the cortical tension of both cells at the cell-cell interface,  $2 \cdot \gamma_{CC}$ , and the adhesion tension,  $\gamma_A$ , acting in antiparallel directions. The cortical tension is in balance with the internal cellular pressure, P.

## 1.3 Cell-cell contact formation: from molecules to cells and tissues

In the following section, we summarize and discuss how cell-cell adhesion is described by integrating biological components with quantitative terms inspired by polymer physics. We start with descriptions of cell-cell adhesion based on molecular interactions at the contacting membranes and then move on to descriptions on the cellular and tissue/organismal scale.

#### 1.3.1 The role of molecular interactions over the contact

For describing cell-cell adhesion on the molecular scale, biomimetic systems such as phospholipid membranes and vesicles were initially used. Here, adhesion is described based on the formation of specific molecular bonds and the role that the plasma membrane and the glycocalyx play therein. The theoretical basis for such description of cell-cell adhesion was first established by Bell (30), arguing that, aside from weak electrical forces between two cell membranes, attractive forces, generated by the specific binding of integral membrane proteins, must be considered to explain cell-cell detachment forces. This was soon followed by the identification of cadherin adhesion receptors capable of mediating attractive forces between cells (31). On the experimental side, various biomimetic systems were established that allowed controlling the identity, density, and mobility of adhesion molecules on surfaces. Specifically, giant vesicles and planar membranes decorated with adhesion molecules (attractive forces) and polymer cushions (repellent forces – inspired by glycocalyx) were employed to mimic interactions between two cells (32). On the theoretical side, various frameworks were developed to explain different aspects of adhesion in those biomimetic settings. They showed that the distance of an adhering vesicle to the contacting membrane is determined by the minimum of the free adhesion energy (11, 12). At high receptor concentrations, contacts formed a homogenous tight adhesion zone, whereas at low receptor concentrations, contacts were composed of tight adhesion domains conferring strong adhesion separated by weak adhesion domains containing glycocalyx, corresponding to two minima of the free energy (33). Using a thermodynamic framework in which the adhesion energy depends on both the gain of enthalpy by the formation of bonds and the cost of entropy through the immobilization of receptors and suppression of membrane fluctuations, adhesion domains were predicted to preferentially localize to the rim of vesicle-bilayer contacts (34). This configuration is a result of bond dynamics, receptor crowding, and slowed-down diffusion upon adhesion molecule binding. These predictions were subsequently confirmed by experimental observations in a physiological context showing that cadherin adhesion molecules preferentially accumulate at the rim of cell-cell contacts (Fig.1.2A; (35, 36)).

Biomimetic studies were also crucial for unraveling the role of cadherin clustering and mobility in cell-cell adhesion. Cadherins are known to form nanoclusters, which increase the cooperativity and stability of those molecules (37). Cadherin clustering depends on cis interactions of cadherins within the same cell and does not necessarily require cadherin trans binding given that cadherin ectodomains can form those clusters without

engaging in trans interactions over the contact (21). Changing the ability of cadherins to engage in cis clustering through membrane fluctuations was further found to influence their ability to form trans bonds, which are required for nucleation and growth of adhesion domains in model membranes (38). In a cellular context, intracellular interactions of cadherin nanoclusters with the cortical actomyosin network were shown to be critical for cadherin-mediated contact formation by decreasing the mobility of those clusters within the membrane (39). Yet, biomimetic studies predicted that some mobility of adhesion receptors is still required to form stronger contacts by allowing diffusion of those receptors into the contact zone and thus increasing their likelihood to participate in bond formation (33).

Finally, through biomimetic, single-molecule, and cell culture studies, the sensitivity of adhesion molecules to mechanical forces was shown to be a critical determinant of cell-cell adhesion strength. In contacts between bilayers and vesicles carrying mobile adhesion proteins, adhesion sites were found to enlarge and become more immobile in response to a pulling force at the contact as a result of the acquisition of new bonds at edges of alreadydense sites or condensation of existing bonds (33). In addition to those general effects on adhesion site assembly, mechanical forces also affect the bonds between individual adhesion receptors. Typically, molecular interactions between adhesion receptors are studied by atomic force microscopy at the millisecond timescale, which is well below the timescale of molecular offrates at which bond dissociation occurs even if no external force is applied (30). Atomic force microscopy measurements of cadherin bonds revealed that detachment forces between cadherins typically range from a few tens to hundreds of pN (40) and that the bond strength of cadherins depends on the type of cadherin and its specific off-rate. The analysis of detachment forces further showed that cadherin molecules preferably form homotypic bonds, with, for instance, homotypic E-cadherin bonds being stronger than homotypic N-cadherin bonds (41). Moreover, cadherin bonds also become more resistant to detachment with increased loading, a phenomenon explained by cadherin ectodomains forming X-dimers that function as catch bonds (42), increasing bond lifetime as a function of pulling force (43, 44).

Collectively, biomimetic studies using model membranes and vesicles, together with single-molecule studies probing the characteristics of adhesion molecules, paved the way for understanding the molecular and physical processes by which cell-cell contacts are initiated and maintained. In particular, they provided insight into the role of several cell structures and processes, such as the glycocalyx and membrane fluctuations, for cell-cell contact formation, which is still difficult to rigorously address in a

more physiological cell setting. By stepwise increasing the complexity of biomimetic assays - e.g., by encapsulating cytoskeletal components within vesicles to study the interaction between adhesion molecules and the cytoskeleton - those reconstituted systems might become even more powerful and provide a platform for systematically analyzing cell-cell adhesion independently from the specific features of entire cells, tissues, or organisms.

#### 1.3.2 The role of intercellular forces arising at the contact

In the following section, we discuss how experimental and theoretical studies of cell-cell adhesion forces on the cellular scale provided insight into the role of cell mechanics in cell-cell adhesion and contact formation. It is well established that most biological tissues are viscoelastic, behaving predominantly elastic at short timescales and viscous at long timescales (45). Consequently, cells have been modeled as solid elastic spheres or viscous liquid droplets depending on the specific cellular process studied. Assuming that the contacting cells behave as solid elastic spheres able to establish short-interaction-range adhesion, the Johnson-Kendall-Roberts (JKR) model used in polymer adhesion was applied to describe cell-cell contact detachment. The model permits the adhesion energy to be determined based on the pulling force needed to detach two spherical objects and their harmonic mean radii. For measuring detachment forces between contacting cells in the nN range, the dual pipette aspiration (DPA) technique is most commonly used (Fig.1.2A; (46)). Interestingly, the detachment force measured by DPA for nonspecific adhesion between culture cells displaying high elasticity could be well explained using the JKR model (47). However, for other cell types that display lower elasticity, only an extended version of the JKR model, in which cells are represented as thin shells with liquid cores that could be deformed as pulling forces were applied, was able to recapitulate experimental data (48, 49).

The advantage of those coarse-grained theoretical models of cell detachment forces over the molecular-interaction-based theoretical models described in the previous chapter is the inclusion of the mechanical properties of cells. However, a caveat of taking detachment forces as a proxy for adhesion energy is the observation that cells can respond to mechanical forces by modulating their adhesion apparatus and thus adhesive properties. For instance, pulling on the contact zone increases E-cadherin and actin recruitment (Fig.1.2A; (50)), and applied forces can alter the mechanical properties of the cell cytoskeleton (51). Given that the detachment forces are thought to depend on mechanical properties of the actomyosin cortex of the adhering cells, such as its thickness, stiffness, and contractility (52); the

equilibrium adhesion energy would be expected to change when detachment forces are applied.

The linkage of cadherins to the actomyosin cortex plays a central role for mechanosensation at cell-cell contacts (Fig.1.1; (10)). Anchorage of cadherins to the actomyosin cortex is mediated by various molecules, including  $\beta$ -catenin,  $\alpha$ -catenin, and vinculin, and strengthens under force, a behavior characteristic of catch bonds (53). Specifically, whereas a single  $\beta$ -catenin/ $\alpha$ -catenin heterodimer forms a slip bond with F-actin, cooperativity of several heterodimers results in a catch-bond behavior (54). This is due to several  $\beta$ -catenin/ $\alpha$ -catenin heterodimers mediating longer-lasting contacts with F-actin, thereby allowing the tension-mediated unfolding of  $\alpha$ -catenin (55), which in turn reveals cryptic binding sites to vinculin, a molecule directly linking the cadherin/catenin complex to the actin cytoskeleton (56). This internal amplification mechanism, together with the observation that vinculin itself forms a catch bond with F-actin (57), provides an explanation for the mechanosensitivity of cadherin-mediated cell-cell contact sites.

Measured cell-cell detachment forces not only might change because of mechanosensitive feedback but also are dependent on the main direction of forces applied to the contact (normal or shear forces). Recent work suggests the direction of force to have different effects on cell-cell contacts: during Drosophila embryonic axis elongation, normal forces on cell-cell junctions, exerted by a medial actomyosin network within the apex of epithelial cells, increase E-cadherin levels and thus cell-cell adhesion, whereas shear forces through a junctional actomyosin network decrease E-cadherin levels (58). Such differential effects of normal versus shear forces might explain why detachment forces can vary depending on the specific measurement methods used, such as centrifugation, shear flow, or DPA.

In addition to cell-cell detachment force measurements, intercellular forces were determined by measuring traction forces of adhering cells through traction force microscopy (59) and micropillar arrays (60), both of which allow the extraction of intercellular forces on the basis of the two-dimensional force balance (61, 62). Those intercellular forces were found to positively correlate with cadherin levels at cell-cell contacts (63). Likewise, for endothelial cell doublets on a defined spreading area, intercellular forces linearly increased with cell-cell contact size (62). In contrast, epithelial cells grown on a free spreading area showed no apparent scaling between intercellular forces and cell-cell contact size (61), suggesting that the relation of contact size and intercellular forces is highly context dependent.

The analysis of traction forces might also give important insights into

the interplay between cell-cell and cell-matrix adhesions. In migrating cell clusters, traction forces dominate at the edge (64, 65) and intercellular stresses increase toward the center of the cluster as a result of traction forces of the outwardly moving cells being transmitted as intercellular forces to the trailing cells behind (66, 67). Recently, the interplay between cell-celladhesion-mediated intercellular and cell-ECM-adhesion-mediated intracellular tension was found to be responsible for cell monolayers displaying either contractile or extensile behavior (68), suggesting that the nature of active forces in tissues depends on the cross talk between cell-cell and cell-ECM adhesion. In line with this, knockout of E-cadherin in epithelial cells caused a crossover from extensile to contractile tissue behavior along with relocalization of vinculin from cell-cell to cell-ECM contacts and an increase in cell-ECM adhesion (68). Thus, the strength of cell-cell adhesion - and, with that, the tissue behavior - strongly depends on the interactions with the extracellular environment and the adaptation of intracellular contractility.

Collectively, the analysis of cell-cell detachment forces was instrumental in identifying the adhesion energy and thus cell-intrinsic adhesion of adherent cells when separated. However, to understand the discrepancies in the adhesive behavior of different cell types, more parametric tests and models need to be developed to incorporate effects of cell viscoelasticity, contractility, and adhesion receptor mobility. In particular, changes in the distribution of adhesion molecules at heterogeneous cell-cell contact sites and the effect of cytoskeletal rearrangements that occur upon force application need to be quantified and incorporated in future computational models. Finally, the observation that intracellular bonds, linking the adhesion complex to the actomyosin cytoskeleton, break first when cell-cell contacts are being separated suggests that deadhesion and adhesion energies might be different (18, 29). Current models of cell-cell detachment, however, do not distinguish between the two. In line with this, recent observations showed that experimentally measured detachment forces are higher than theoretically predicted on the basis of the adhesion energy, pointing at the possibility that cell-cell detachment forces might depend more on dissipative processes associated with the detachment process rather than the adhesion energy (69). Emerging tools for determining cell-cell adhesion forces, such as Förster resonance energy transfer sensors to measure endogenous molecular forces (70, 71), DNA-based fluorescent force probes (72), oil droplets decorated with cadherin receptor ligands (73), and pressure probes that deform with local stresses (74), might lead to a deeper understanding of intercellular adhesion.

#### 1.3.3 The role of interfacial tension in cell aggregates

In analogy to liquids minimizing their surface area through surface tension as a result of the cohesion of their constituent molecules, the surface tension of cells and tissues is used as a proxy for cell-cell adhesion strength. In the following section, we discuss how cell-cell adhesion can be interpreted by the extent of surface tension, how surface tension is determined by tensions at different cellular interfaces, and how those surface/interfacial tensions were used in various models explaining cell/tissue shape changes and cell sorting. Originally, tissue surface tension was assumed to be determined by the adhesion energy, for instance, emerging from cadherin binding over the contact, a view supported with experiments in cell aggregates, which showed cadherin expression levels to linearly correlate with tissue surface tension (15, 75). Subsequent work showed that, in addition or as an alternative to adhesion energy, tissue surface tension critically depends on the function of cortical actomyosin tension (17, 59) and its modulation at cell-cell contacts (Fig.1.3; (36, 76)). Cortical tension is modulated not only by the binding of cadherin adhesion molecules over the contact (18) but also by unbound cadherins not engaged in trans binding, suggesting that a dynamic interplay between cadherins and the cortical actomyosin network determines the balance of interfacial tensions and thus surface tension of tissues (69).

At the cell-cell contact interface, interfacial tension is determined by both adhesion tension (a negative tension as a result of adhesion molecules binding over the contact), which expands the contact area, and cortical tension, which reduces it (Fig.1.2B). At contact-free interfaces, in contrast, surface tension is predominantly determined by cortical tension. Notably, cortical tension can differ at contact-free and adhering interfaces. Studies on zebrafish germ layer progenitor cells suggest that tissue surface tension arises from the difference between the two (77). This difference in tensions between the cell-cell versus contact-free interfaces is due to adhesion receptor signaling changing the actomyosin cortex, and thus cortical tension, at the cell-cell interface rather than adhesion tension lowering cell-cell interfacial tension (36). In line with adhesion receptors lowering cortical tension at the cell-cell contact are observations showing that E-cadherinmutant mouse embryos fail in reducing myosin II from cell-cell contacts (78). Likewise, downregulation of C-cadherin in Xenopus embryonic aggregates prevents proper reduction of actin from contacts (79). This suggests that adhesion receptor signaling reduces cortical tension at contacts by both diminishing myosin II activity and/or localization and modifying cortical actin density and organization. The molecular composition of the signaling cascade downstream of cadherin adhesion receptors modulating the actomyosin cortex is not yet entirely clear. The actin-severing protein cofilin was found to colocalize with E-cadherin at punctate adherens junctions (80), whereas other studies reported that interaction of the cadherin adhesion complex through  $\alpha$ -E-catenin with actin inhibits cofilin binding in vitro (81). Similarly, the branched actin nucleator Arp2/3 was proposed to be not only suppressed at nascent contacts through  $\alpha$ -E-catenin (81) but also recruited to cortical actin underlying cell-cell contacts (80, 82). Moreover, the linear actin nucleator formin was shown to be recruited to adherens junctions by  $\alpha$ -E-catenin (83). These data suggest that cadherin adhesion receptors affect the cortical actin cytoskeleton by dynamically recruiting different types of actin nucleators, which could potentially control cortical tension by regulating actin filament length (84), and network density (85). Changes in cortical actin at cell-cell contacts might feed back on cortical myosin II recruitment given that, for instance, in mouse oocytes, cortical Arp2/3 enrichment leads not only to cortex thickening but also to myosin II depletion and, consequently, reduction in cortical tension (86).

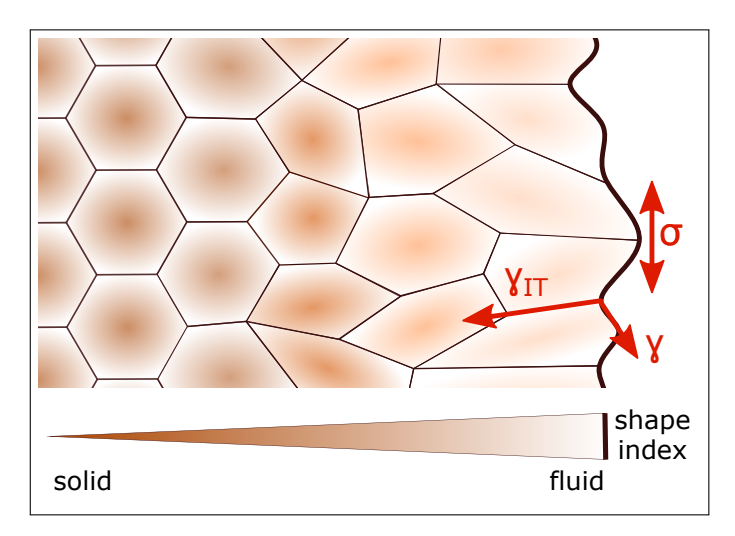


Figure 1.3: The tissue surface tension,  $\sigma$ , at the tissue edge results from the difference between the interfacial tension,  $\gamma_{IT}$ , at the cell-cell contact and the cortical tension,  $\gamma$ , at the contact-free surface. It minimizes the contact-free surface area by smoothing the tissue edge. Interfacial tension also contributes to determining the cell shape index, an indicator of tissue fluidity: cells within the cluster typically display more regular hexagonal shapes, are densely packed by surrounding neighbors, and thus behave more solid-like. Cells at the tissue edge, in contrast, are more elongated and mobile, and thus show a fluid-like behavior.

The Rho family GTPases Rac, Cdc42, and RhoA play an important role in remodeling the actomyosin cortex at cell-cell adhesion sites. Rac, for instance, is transiently activated by cadherins at the edges of an expanding contact, leading to local activation of the Arp2/3 complex and thus branched actin polymerization (87, 88). Activation of both Rac and Cdc42 were observed during the formation of cell aggregates, which contributed to the strengthening of cell-cell contacts (13). Cdc42 was also found to be involved in the initiation of cell-cell adhesion (89), possibly by promoting the formation of E-cadherin-containing filopodia, facilitating contact formation (90). RhoA is recruited to adherens junctions, where it activates cortical actomyosin contractility and recruits formins, promoting linear actin polymerization (91). At nascent contacts, in contrast, RhoA activity is inhibited by Rac, decreasing cortical actomyosin contraction and thus tension (88, 92). Yet the exact spatiotemporal regulation and function of Rho family GTPases as signaling effectors of cadherin adhesion receptors in contact formation and maintenance remain to be fully explored.

To explain the effects of interfacial tension regulation by different effector mechanisms, several microscopic mechanical models based on energy minimization and interfacial tension balance were employed describing cellcell contact dynamics both in vitro and in vivo. For instance, the cellular Potts model, in which each cell is defined as connected pixels, was developed to test the contribution of different levels of adhesion receptor expression in cell-sorting experiments and the role of cell motility therein (93). Later, cortical tension was added to this model to capture the role of differential cell cortical tension in cell sorting (94, 95). To more realistically capture the dynamics of confluent tissues on a cellular scale, vertex models, in which cells are defined as polygons whose vertices can move with mechanical forces, were developed. Vertex models were successfully applied for describing various morphogenetic processes, such as boundary formation, epithelial buckling, and wound healing, because of their ability to capture specific cellular processes, such as cell shape changes, divisions, extrusions, and rearrangements, as well as viscoelastic cell properties (96). As a hybrid of vertex models and self-propelled particle models, Voronoi models were recently developed in which not vertices but cell centers are tracked (97). These models were able to incorporate single-cell motility, missing from the vertex models, and predict more diverse shape distributions (98) and cellular rearrangements (99). More recently, vertex and Voronoi models were also used to describe abrupt and drastic changes in tissue material properties that might resemble transitions in states of matter, commonly referred to as phase transitions (100-102). Interestingly, phase transitions in confluent tissues appear to correlate to a 'cell shape index', a quantity that describes the cell geometry (Fig.1.3; (100)). The cell geometry is regulated by the competition between cell-cell adhesion energy and cortical tension. An increase in cell-cell adhesion and a decrease in cortical tension lead to a change in cell shape and in turn to a transition of the whole tissue from solid-like to fluid-like behavior in a process called 'unjamming transition'. The unjamming transition is characterized by increased irregularity in cell shapes and reduced number of contacts with neighboring cells, allowing cellular rearrangements (100, 102). Recent studies also suggest the unjamming transition to be dominated by cellular traction forces (103). At the level of cell-cell contacts, force-mediated  $\alpha$ -catenin clustering was found to trigger a fluid-to-solid phase transition, suggesting that changes in the composition of cadherin adhesion complexes can locally modulate rheological properties of the contact (54). Tissue-scale phase transitions were observed not only in cultures but also within the physiologically relevant context of the developing embryo (104-107) and in disease-related processes such as wound healing (108) and tumor metastasis (109). Extension of existing vertex models (110) and application of new theoretical frameworks, such as rigidity percolation theory (111), were recently shown to accurately describe tissue phase transitions in nonconfluent embryonic tissues to understand these phenomena mechanistically.

So far, research on interfacial tensions of cells and tissues primarily focused on the role of adhesion tension and cortical tension in regulating interfacial tension. However, other factors might also be involved. Membrane tension, for instance, also contributes to surface tension, although its specific contribution is difficult to determine because the plasma membrane is mechanically coupled to the underlying actomyosin cortex through proteins mediating membrane-to-cortex attachment and thus is difficult to disentangle from cortical tension. Although membrane tension was shown to be typically much smaller than cortical tension, there is increasing evidence in different cell types, such as keratocytes, that suggests membrane tension still significantly contributes to the overall surface tension of those cells (112). In addition to membrane tension, high adhesion tension between dynamically cross-linking components of interacting glycocalices was recently proposed to contribute to tissue surface tension in systems such as chick embryos and various mammalian cell lines, in which surface tension clearly exceeds the theoretically expected values based on cadherinmediated adhesion and cortical tension alone (113). Finally, external factors, such as the presence of ECM and the osmolarity of the interstitial fluid, were shown to affect interfacial tensions of cells and tissues. ECM interactions can contribute to cell sorting by regulating cell-ECM and cell-cell interfacial tensions in monolayers and surface tension in cell aggregates (68, 114), whereas osmolarity was recently demonstrated as an important regulator of tissue surface tension by regulating membrane tension and cortical tension via changes in the internal cellular pressure and volume (115).

Beyond cadherins, comparably little is known about upstream regulators of cell/tissue interfacial tensions. Living tissues have a remarkably diverse cell surface proteome, suggesting that several other of those proteins might be involved in controlling interfacial tensions. For instance, the differential expression of proteins mediating cell repulsion, such as Ephephrin receptor-ligand pairs, or signaling receptors, such as leucine-rich repeat family receptors (including Toll-like receptors), were shown to mediate differences in cortical tension, which is important for boundary formation in developing vertebrate and invertebrate embryos (116, 117). The potential role of those and many other cell surface proteins in regulating interfacial tensions in different model systems remains to be investigated.

#### 1.4 Conclusion and perspectives

Cell-cell adhesion has been studied for many decades by both biologists and physicists. In those studies, different views of adhesion emerged, which can be roughly categorized as 1) the affinity of molecular bonds, 2) a cohesive force supported by a force-sensing and force-transducing machinery, and 3) the modulation of interfacial tensions through adhesion receptor signaling. These different views are nonexclusive because they simply emphasize different functions of the adhesion apparatus that together define adhesion. In evolution, these different functions seem to have coevolved because, for instance, the core adhesion complex, consisting of cadherins and catenins that bind to F-actin, emerged together with the appearance of metazoans (118). Moreover, cadherins predating this complex already carry intracellular domains that can possibly interact with actin-binding proteins (119), suggesting that cadherin extracellular binding and intracellular signaling could have been directly adapted with the appearance of multicellularity.

Initially, the degree of cell-cell adhesion was thought to correspond to the adhesion strength of cell-cell contacts at steady state. However, observations of cell-cell contacts in their physiological context show that cell-cell adhesion is a rather dynamic process, with the duration and size of cell-cell contacts constantly changing. Contact size and duration represent critical parameters modulating not only the extent by which cells rearrange in cohesive tissues (120) but also the activity of various signaling pathways

involved in cell fate specification in embryos (121, 122). Recently, cell-cell contact dynamics were shown to be important parameters determining tissue material properties and the transitions between different material phases (45). How those dynamic cell-cell contact properties are regulated on a molecular and cellular scale have only begun to be understood. For example, the size of cell-cell contacts was originally thought to increase with the ratio of cortical tension at the contact-free to the cell-cell interfaces (36). Surprisingly, most recently, this view was challenged by showing that the relationship between cell-cell contact size and cortical tension of the contact-free cortex is nonmonotonic, reversing at high levels of cortical tension because of tension-mediated E-cadherin stabilization, which limits contact expansion (123). Further work is needed to elucidate the relationship between various features of cell-cell contacts to determine their multifaceted functions in multicellular settings.

Cell-cell adhesion is regulated through both intracellular and extracellular cues, possibly involving various feedback loops between them. For instance, myosin II activity was shown not only to increase cytoskeletal anchoring of cadherins (70) but also to slow down actin turnover, which affects E-cadherin mobility at the cell-cell contacts and thus contact expansion (35, 123). In turn, the stability of cadherin clusters was shown to regulate actin turnover, suggesting a bidirectional coupling between actin and cadherin dynamics (80). Many questions remain as to the regulation and function of cell-cell adhesion. What distinguishes the adhesion apparatus from the cell cytoskeleton? Does cell-cell adhesion simply function as a molecular linker connecting the cytoskeleton of neighboring cells? That said, could the adhesion complex be regarded as a specialized cytoskeletal component needed for the assembly, dynamic regulation, and coordination of supracellular cytoskeletal networks? Would such supracellular cytoskeletal networks just represent a permutation of intracellular cytoskeletal networks, or would the addition of cell-cell adhesion sites provide emergent features that cannot be found in unconnected cytoskeletal networks? To answer those questions, synthetic approaches for engineering cell-cell contacts might be helpful because they would allow the systematic study of different properties of cell-cell contacts in the presence and absence of cytoskeletal anchoring. Likewise, theoretical models need to be developed to connect molecular-scale interactions and dynamics of adhesion and cytoskeletal molecules to tissue-scale functions of cell-cell adhesion, such as tissue morphogenesis and material properties (124).

Cell-cell adhesion is integral to the evolution of multicellularity. Studying cell-cell adhesion, therefore, provides the basis for understanding how

multicellularity has emerged. Although in the past, cell-cell adhesion has been predominantly studied on the basis of the extracellular bindings of adhesion receptors and their affinity and strength, it becomes increasingly clear that the coupling of those receptors to the cytoskeleton is equally important. This highlights two essential and tightly intertwined functions of adhesion: providing selectivity in cellular interactions and regulating the mechanical and biochemical cross talk between neighboring cells. This naturally involves both biochemical and mechanical signals; thus, understanding their interaction through mechanosensation will be indispensable for elucidating the basis of cell-cell adhesion.

### References

- Miller, J. G. (1973). Living Systems: The Organism. The Quarterly Review of Biology 48, 92–276.
- (2) Turlier, H., and Maître, J.-L. (2015). Mechanics of tissue compaction. Seminars in Cell & Developmental Biology 47-48, 110-117.
- (3) Lecuit, T., and Lenne, P.-F. (2007). Cell surface mechanics and the control of cell shape, tissue patterns and morphogenesis. Nature Reviews Molecular Cell Biology 8, 633-644.
- (4) Collins, C., and Nelson, W. J. (2015). Running with neighbors: coordinating cell migration and cell-cell adhesion. Current Opinion in Cell Biology 36, 62-70.
- (5) Berx, G., and van Roy, F. (2009). Involvement of members of the cadherin superfamily in cancer. *Cold Spring Harbor perspectives in biology* 1, a003129–a003129.
- (6) El-Amraoui, A., and Petit, C. (2010). Cadherins as targets for genetic diseases. Cold Spring Harbor perspectives in biology 2, a003095–a003095.
- (7) Janiszewska, M., Primi, M. C., and Izard, T. (2020). Cell adhesion in cancer: Beyond the migration of single cells. *Journal of Biological Chemistry* 295, 2495–2505.
- (8) Yamada, S., and Nelson, W. J. (2007). Synapses: Sites of Cell Recognition, Adhesion, and Functional Specification. Annual Review of Biochemistry 76, 267–294.
- (9) Halbleib, J. M., and Nelson, W. J. (2006). Cadherins in development: cell adhesion, sorting, and tissue morphogenesis. *Genes & development 20*, 3199–3214.
- (10) Huveneers, S., and de Rooij, J. (2013). Mechanosensitive systems at the cadherin-Factin interface. *Journal of Cell Science* 126, 403–413.
- (11) Bell, G., Dembo, M., and Bongrand, P. (1984). Cell adhesion. Competition between nonspecific repulsion and specific bonding. *Biophysical Journal* 45, 1051–1064.
- (12) Bruinsma, R., Behrisch, A., and Sackmann, E. (2000). Adhesive switching of membranes: Experiment and theory. Phys. Rev. E 61, 4253–4267.
- (13) Chu, Y.-S., Thomas, W. A., Eder, O., Pincet, F., Perez, E., Thiery, J. P., and Dufour, S. (2004). Force measurements in E-cadherin-mediated cell doublets reveal rapid adhesion strengthened by actin cytoskeleton remodeling through Rac and Cdc42. The Journal of cell biology 167, 1183–1194.
- (14) Charras, G., and Yap, A. S. (2018). Tensile Forces and Mechanotransduction at Cell-Cell Junctions. Current Biology 28, R445-R457.

24 References

(15) Steinberg, M. S. (1963). Reconstruction of Tissues by Dissociated Cells. Science 141, 401–408.

- (16) Harris, A. K. (1976). Is cell sorting caused by differences in the work of intercellular adhesion? A critique of the steinberg hypothesis. *Journal of Theoretical Biology* 61, 267–285.
- (17) Brodland, G. W. (2002). The Differential Interfacial Tension Hypothesis (DITH): A Comprehensive Theory for the Self-Rearrangement of Embryonic Cells and Tissues. *Journal of Biomechanical Engineering* 124, 188–197.
- (18) Winklbauer, R. (2015). Cell adhesion strength from cortical tension an integration of concepts. Journal of Cell Science 128, 3687–3693.
- (19) Zaidel-Bar, R. (2013). Cadherin adhesome at a glance. Journal of Cell Science 126, 373–378.
- (20) Brasch, J., Harrison, O. J., Honig, B., and Shapiro, L. (2012). Thinking outside the cell: how cadherins drive adhesion. *Trends in cell biology* 22, 299–310.
- (21) Thompson, C. J., Vu, V. H., Leckband, D. E., and Schwartz, D. K. (2019). Cadherin Extracellular Domain Clustering in the Absence of Trans-Interactions. The Journal of Physical Chemistry Letters 10, 4528–4534.
- (22) Chugh, P., and Paluch, E. K. (2018). The actin cortex at a glance. *Journal of Cell Science* 131.
- (23) Simons, K., and Ikonen, E. (1997). Functional rafts in cell membranes. *Nature* 387, 569–572.
- (24) Truong-Quang, B.-A., and Lenne, P.-F. (2014). Membrane microdomains: from seeing to understanding. Frontiers in plant science 5, 18–18.
- (25) Clarris, B., and Fraser, J. (1968). On the pericellular zone of some mammalian cells in vitro. Experimental Cell Research 49, 181–193.
- (26) Frantz, C., Stewart, K. M., and Weaver, V. M. (2010). The extracellular matrix at a glance. *Journal of Cell Science* 123, 4195–4200.
- (27) Salbreux, G., Charras, G., and Paluch, E. (2012). Actin cortex mechanics and cellular morphogenesis. *Trends in Cell Biology* 22, 536–545.
- (28) Helfrich, W. (1973). Elastic Properties of Lipid Bilayers: Theory and Possible Experiments. Zeitschrift für Naturforschung C 28, 693–703.
- (29) Maître, J.-L., and Heisenberg, C.-P. (2013). Three Functions of Cadherins in Cell Adhesion. Current Biology 23, R626–R633.
- (30) Bell, G. (1978). Models for the specific adhesion of cells to cells. Science 200, 618–627.
- (31) Takeichi, M., Atsumi, T., Yoshida, C., Uno, K., and Okada, T. (1981). Selective adhesion of embryonal carcinoma cells and differentiated cells by Ca2+dependent sites. Developmental Biology 87, 340–350.
- (32) Sackmann, E. (1996). Supported Membranes: Scientific and Practical Applications. Science 271, 43–48.
- (33) Smith, A.-S., and Sackmann, E. (2009). Progress in Mimetic Studies of Cell Adhesion and the Mechanosensing. *ChemPhysChem* 10, 66–78.

References 25

(34) Schmidt, D., Bihr, T., Fenz, S., Merkel, R., Seifert, U., Sengupta, K., and Smith, A.-S. (2015). Crowding of receptors induces ring-like adhesions in model membranes. Biochimica et Biophysica Acta (BBA) - Molecular Cell Research 1853, 2984–2991.

- (35) Engl, W., Arasi, B., Yap, L. L., Thiery, J. P., and Viasnoff, V. (2014). Actin dynamics modulate mechanosensitive immobilization of E-cadherin at adherens junctions. *Nature Cell Biology* 16, 584–591.
- (36) Maître, J.-L., Berthoumieux, H., Krens, S. F. G., Salbreux, G., Jülicher, F., Paluch, E., and Heisenberg, C.-P. (2012). Adhesion Functions in Cell Sorting by Mechanically Coupling the Cortices of Adhering Cells. *Science* 338, 253–256.
- (37) Yap, A. S., Gomez, G. A., and Parton, R. G. (2015). Adherens Junctions Revisualized: Organizing Cadherins as Nanoassemblies. *Developmental Cell* 35, 12–20.
- (38) Fenz, S. F., Bihr, T., Schmidt, D., Merkel, R., Seifert, U., Sengupta, K., and Smith, A.-S. (2017). Membrane fluctuations mediate lateral interaction between cadherin bonds. *Nature Physics* 13, 906–913.
- (39) Chandran, R., Kale, G., Philippe, J.-M., Lecuit, T., and Mayor, S. (2021). Distinct actin-dependent nanoscale assemblies underlie the dynamic and hierarchical organization of E-cadherin. *Current Biology* 31, 1726–1736.e4.
- (40) Baumgartner, W., Hinterdorfer, P., Ness, W., Raab, A., Vestweber, D., Schindler, H., and Drenckhahn, D. (2000). Cadherin interaction probed by atomic force microscopy. *Proceedings of the National Academy of Sciences* 97, 4005–4010.
- (41) Panorchan, P., Thompson, M. S., Davis, K. J., Tseng, Y., Konstantopoulos, K., and Wirtz, D. (2006). Single-molecule analysis of cadherin-mediated cell-cell adhesion. *Journal of Cell Science* 119, 66–74.
- (42) Dembo, M., Torney, D. C., Saxman, K., and Hammer, D. (1988). The Reaction-Limited Kinetics of Membrane-to-Surface Adhesion and Detachment. Proceedings of the Royal Society of London. Series B, Biological Sciences 234, 55–83.
- (43) Pittet, P., Lee, K., Kulik, A. J., Meister, J.-J., and Hinz, B. (2008). Fibrogenic fibroblasts increase intercellular adhesion strength by reinforcing individual OB-cadherin bonds. *Journal of Cell Science* 121, 877–886.
- (44) Rakshit, S., Zhang, Y., Manibog, K., Shafraz, O., and Sivasankar, S. (2012). Ideal, catch, and slip bonds in cadherin adhesion. Proceedings of the National Academy of Sciences 109, 18815–18820.
- (45) Petridou, N. I., and Heisenberg, C.-P. (2019). Tissue rheology in embryonic organization. *The EMBO Journal 38*, e102497.
- (46) Sung, K., Sung, L., Crimmins, M., Burakoff, S., and Chien, S. (1986). Determination of junction avidity of cytolytic T cell and target cell. *Science* 234, 1405–1408.
- (47) Chu, Y.-S., Dufour, S., Thiery, J. P., Perez, E., and Pincet, F. (2005). Johnson-Kendall-Roberts Theory Applied to Living Cells. *Phys. Rev. Lett.* 94, 028102.
- (48) Pierrat, S., Brochard-Wyart, F., and Nassoy, P. (2004). Enforced Detachment of Red Blood Cells Adhering to Surfaces: Statics and Dynamics. *Biophysical Journal* 87, 2855–2869.

(49) Brochard-Wyart, F., and de Gennes, P.-G. (2003). Unbinding of adhesive vesicles. Comptes Rendus Physique 4, 281–287.

- (50) Gao, X., Acharya, B. R., Engl, W. C. O., De Mets, R., Thiery, J. P., Yap, A. S., and Viasnoff, V. (2018). Probing compression versus stretch activated recruitment of cortical actin and apical junction proteins using mechanical stimulations of suspended doublets. *APL Bioengineering* 2, 026111.
- (51) Schwarz, U. S., and Safran, S. A. (2013). Physics of adherent cells. Rev. Mod. Phys. 85, 1327–1381.
- (52) Smeets, B., Cuvelier, M., Pešek, J., and Ramon, H. (2019). The Effect of Cortical Elasticity and Active Tension on Cell Adhesion Mechanics. *Biophysical Journal* 116, 930–937.
- (53) Buckley, C. D., Tan, J., Anderson, K. L., Hanein, D., Volkmann, N., Weis, W. I., Nelson, W. J., and Dunn, A. R. (2014). The minimal cadherin-catenin complex binds to actin filaments under force. *Science* 346, 1254211.
- (54) Arbore, C., Sergides, M., Gardini, L., Bianchi, G., Kashchuk, A. V., Pertici, I., Bianco, P., Pavone, F. S., and Capitanio, M. (2022). α-catenin switches between a slip and an asymmetric catch bond with F-actin to cooperatively regulate cell junction fluidity. Nature Communications 13, 1146.
- (55) Yonemura, S., Wada, Y., Watanabe, T., Nagafuchi, A., and Shibata, M. (2010). α-Catenin as a tension transducer that induces adherens junction development. Nature Cell Biology 12, 533–542.
- (56) Huveneers, S., Oldenburg, J., Spanjaard, E., van der Krogt, G., Grigoriev, I., Akhmanova, A., Rehmann, H., and de Rooij, J. (2012). Vinculin associates with endothelial VE-cadherin junctions to control force-dependent remodeling. *Journal of Cell Biology* 196, 641–652.
- (57) Huang, D. L., Bax, N. A., Buckley, C. D., Weis, W. I., and Dunn, A. R. (2017). Vinculin forms a directionally asymmetric catch bond with F-actin. *Science 357*, 703–706.
- (58) Kale, G. R., Yang, X., Philippe, J.-M., Mani, M., Lenne, P.-F., and Lecuit, T. (2018). Distinct contributions of tensile and shear stress on E-cadherin levels during morphogenesis. *Nature Communications* 9, 5021.
- (59) Harris, A. K., Stopak, D., and Wild, P. (1981). Fibroblast traction as a mechanism for collagen morphogenesis. *Nature* 290, 249–251.
- (60) Tan, J. L., Tien, J., Pirone, D. M., Gray, D. S., Bhadriraju, K., and Chen, C. S. (2003). Cells lying on a bed of microneedles: An approach to isolate mechanical force. Proceedings of the National Academy of Sciences 100, 1484–1489.
- (61) Maruthamuthu, V., Sabass, B., Schwarz, U. S., and Gardel, M. L. (2011). Cell-ECM traction force modulates endogenous tension at cell-cell contacts. Proceedings of the National Academy of Sciences 108, 4708–4713.
- (62) Liu, Z., Tan, J. L., Cohen, D. M., Yang, M. T., Sniadecki, N. J., Ruiz, S. A., Nelson, C. M., and Chen, C. S. (2010). Mechanical tugging force regulates the size of cell-cell junctions. *Proceedings of the National Academy of Sciences of the United States of America 107*, 9944–9949.

(63) Ng, M. R., Besser, A., Brugge, J. S., and Danuser, G. (2014). Mapping the dynamics of force transduction at cell–cell junctions of epithelial clusters. eLife 3, e03282.

- (64) du Roure, O., Saez, A., Buguin, A., Austin, R. H., Chavrier, P., Siberzan, P., and Ladoux, B. (2005). Force mapping in epithelial cell migration. *Proceedings of the National Academy of Sciences* 102, 2390–2395.
- (65) Mertz, A. F., Che, Y., Banerjee, S., Goldstein, J. M., Rosowski, K. A., Revilla, S. F., Niessen, C. M., Marchetti, M. C., Dufresne, E. R., and Horsley, V. (2013). Cadherin-based intercellular adhesions organize epithelial cell-matrix traction forces. Proceedings of the National Academy of Sciences 110, 842–847.
- (66) Trepat, X., Wasserman, M. R., Angelini, T. E., Millet, E., Weitz, D. A., Butler, J. P., and Fredberg, J. J. (2009). Physical forces during collective cell migration. Nature Physics 5, 426–430.
- (67) Tambe, D. T., Corey Hardin, C., Angelini, T. E., Rajendran, K., Park, C. Y., Serra-Picamal, X., Zhou, E. H., Zaman, M. H., Butler, J. P., Weitz, D. A., Fredberg, J. J., and Trepat, X. (2011). Collective cell guidance by cooperative intercellular forces. *Nature Materials* 10, 469–475.
- (68) Balasubramaniam, L., Doostmohammadi, A., Saw, T. B., Narayana, G. H. N. S., Mueller, R., Dang, T., Thomas, M., Gupta, S., Sonam, S., Yap, A. S., Toyama, Y., Mège, R.-M., Yeomans, J. M., and Ladoux, B. (2021). Investigating the nature of active forces in tissues reveals how contractile cells can form extensile monolayers. *Nature Materials* 20, 1156–1166.
- (69) Aladin, D. M. K., Chu, Y. S., Shen, S., Robinson, R. C., Dufour, S., Viasnoff, V., Borghi, N., and Thiery, J. P. (2021). Extracellular domains of E-cadherin determine key mechanical phenotypes of an epithelium through cell- and non-cell-autonomous outside-in signaling. PLOS ONE 16, 1–22.
- (70) Borghi, N., Sorokina, M., Shcherbakova, O. G., Weis, W. I., Pruitt, B. L., Nelson, W. J., and Dunn, A. R. (2012). E-cadherin is under constitutive actomyosingenerated tension that is increased at cell-cell contacts upon externally applied stretch. Proceedings of the National Academy of Sciences 109, 12568–12573.
- (71) Conway, D. E., Breckenridge, M. T., Hinde, E., Gratton, E., Chen, C. S., and A Schwartz, M. (2013). Fluid shear stress on endothelial cells modulates mechanical tension across VE-cadherin and PECAM-1. Current biology: CB 23, 1024–1030.
- (72) Zhao, B., Li, N., Xie, T., Bagheri, Y., Liang, C., Keshri, P., Sun, Y., and You, M. (2020). Quantifying tensile forces at cell-cell junctions with a DNA-based fluorescent probe. *Chemical Science* 11, 8558–8566.
- (73) Campàs, O., Mammoto, T., Hasso, S., Sperling, R. A., O'Connell, D., Bischof, A. G., Maas, R., Weitz, D. A., Mahadevan, L., and Ingber, D. E. (2014). Quantifying cell-generated mechanical forces within living embryonic tissues. *Nature methods* 11, 183–189.
- (74) Chan, C. J., and Hiiragi, T. (2020). Integration of luminal pressure and signalling in tissue self-organization. *Development 147*.
- (75) Foty, R. A., and Steinberg, M. S. (2005). The differential adhesion hypothesis: a direct evaluation. *Developmental Biology* 278, 255–263.

(76) Youssef, J., Nurse, A. K., Freund, L. B., and Morgan, J. R. (2011). Quantification of the forces driving self-assembly of three-dimensional microtissues. *Proceedings* of the National Academy of Sciences 108, 6993–6998.

- (77) Manning, M. L., Foty, R. A., Steinberg, M. S., and Schoetz, E.-M. (2010). Coaction of intercellular adhesion and cortical tension specifies tissue surface tension. Proceedings of the National Academy of Sciences 107, 12517–12522.
- (78) Maître, J.-L., Niwayama, R., Turlier, H., Nédélec, F., and Hiiragi, T. (2015). Pulsatile cell-autonomous contractility drives compaction in the mouse embryo. Nature Cell Biology 17, 849–855.
- (79) David, R., Luu, O., Damm, E. W., Wen, J. W. H., Nagel, M., and Winklbauer, R. (2014). Tissue cohesion and the mechanics of cell rearrangement. *Development* 141, 3672–3682.
- (80) Indra, I., Troyanovsky, R. B., Shapiro, L., Honig, B., and Troyanovsky, S. M. (2020). Sensing Actin Dynamics through Adherens Junctions. *Cell Reports* 30, 2820–2833.e3.
- (81) Hansen, S. D., Kwiatkowski, A. V., Ouyang, C.-Y., Liu, H., Pokutta, S., Watkins, S. C., Volkmann, N., Hanein, D., Weis, W. I., Mullins, R. D., and Nelson, W. J. (2013). αE-catenin actin-binding domain alters actin filament conformation and regulates binding of nucleation and disassembly factors. Molecular Biology of the Cell 24, 3710–3720.
- (82) Kovacs, E. M., Goodwin, M., Ali, R. G., Paterson, A. D., and Yap, A. S. (2002). Cadherin-Directed Actin Assembly: E-Cadherin Physically Associates with the Arp2/3 Complex to Direct Actin Assembly in Nascent Adhesive Contacts. Current Biology 12, 379–382.
- (83) Kobielak, A., Pasolli, H. A., and Fuchs, E. (2004). Mammalian formin-1 participates in adherens junctions and polymerization of linear actin cables. Nature Cell Biology 6, 21–30.
- (84) Chugh, P., Clark, A. G., Smith, M. B., Cassani, D. A. D., Dierkes, K., Ragab, A., Roux, P. P., Charras, G., Salbreux, G., and Paluch, E. K. (2017). Actin cortex architecture regulates cell surface tension. *Nature Cell Biology* 19, 689–697.
- (85) Xia, S., Lim, Y. B., Zhang, Z., Wang, Y., Zhang, S., Lim, C. T., Yim, E. K. F., and Kanchanawong, P. (2019). Nanoscale Architecture of the Cortical Actin Cytoskeleton in Embryonic Stem Cells. Cell Reports 28, 1251–1267.e7.
- (86) Chaigne, A., Campillo, C., Gov, N., Voituriez, R., Sykes, C., Verlhac, M., and Terret, M. (2015). A narrow window of cortical tension guides asymmetric spindle positioning in the mouse oocyte. *Nature communications* 6, 6027.
- (87) Kitt, K. N., and Nelson, W. J. (2011). Rapid suppression of activated Rac1 by cadherins and nectins during de novo cell-cell adhesion. PloS One 6, e17841.
- (88) Yamada, S., and Nelson, W. J. (2007). Localized zones of Rho and Rac activities drive initiation and expansion of epithelial cell–cell adhesion. *Journal of Cell Biology* 178, 517–527.
- (89) Collins, C., Denisin, A. K., Pruitt, B. L., and Nelson, W. J. (2017). Changes in E-cadherin rigidity sensing regulate cell adhesion. Proceedings of the National Academy of Sciences 114, E5835–E5844.

(90) Biswas, K. H. et al. (2015). E-cadherin junction formation involves an active kinetic nucleation process. Proceedings of the National Academy of Sciences 112, 10932–10937.

- (91) Acharya, B. R., Wu, S. K., Lieu, Z. Z., Parton, R. G., Grill, S. W., Bershadsky, A. D., Gomez, G. A., and Yap, A. S. (2017). Mammalian Diaphanous 1 Mediates a Pathway for E-cadherin to Stabilize Epithelial Barriers through Junctional Contractility. Cell Reports 18, 2854–2867.
- (92) Wildenberg, G. A., Dohn, M. R., Carnahan, R. H., Davis, M. A., Lobdell, N. A., Settleman, J., and Reynolds, A. B. (2006). p120-catenin and p190RhoGAP regulate cell-cell adhesion by coordinating antagonism between Rac and Rho. *Cell* 127, 1027–1039.
- (93) Glazier, J. A., and Graner, F. (1993). Simulation of the differential adhesion driven rearrangement of biological cells. *Physical Review E* 47, 2128–2154.
- (94) Krieg, M., Arboleda-Estudillo, Y., Puech, P.-H., Käfer, J., Graner, F., Müller, D. J., and Heisenberg, C.-P. (2008). Tensile forces govern germ-layer organization in zebrafish. *Nature Cell Biology* 10, 429–436.
- (95) Glazier, J. A., Balter, A., and Popławski, N. J. In Single-Cell-Based Models in Biology and Medicine; Birkhäuser Basel: Basel, 2007, pp 79–106.
- (96) Alt, S., Ganguly, P., and Salbreux, G. (2017). Vertex models: from cell mechanics to tissue morphogenesis. Philosophical transactions of the Royal Society of London. Series B, Biological sciences 372, 20150520.
- (97) Bi, D., Yang, X., Marchetti, M. C., and Manning, M. L. (2016). Motility-driven glass and jamming transitions in biological tissues. *Physical review. X* 6, 021011.
- (98) Sánchez-Gutiérrez, D., Tozluoglu, M., Barry, J. D., Pascual, A., Mao, Y., and Escudero, L. M. (2016). Fundamental physical cellular constraints drive self-organization of tissues. *The EMBO Journal 35*, 77–88.
- (99) Barton, D. L., Henkes, S., Weijer, C. J., and Sknepnek, R. (2017). Active Vertex Model for cell-resolution description of epithelial tissue mechanics. PLOS Computational Biology 13, e1005569.
- (100) Bi, D., Lopez, J. H., Schwarz, J. M., and Manning, M. L. (2015). A density-independent rigidity transition in biological tissues. *Nature Physics* 11, 1074–1079.
- (101) Farhadifar, R., Röper, J.-C., Aigouy, B., Eaton, S., and Jülicher, F. (2007). The Influence of Cell Mechanics, Cell-Cell Interactions, and Proliferation on Epithelial Packing. Current Biology 17, 2095–2104.
- (102) Park, J.-A. et al. (2015). Unjamming and cell shape in the asthmatic airway epithelium. Nature Materials 14, 1040–1048.
- (103) Saraswathibhatla, A., and Notbohm, J. (2020). Tractions and Stress Fibers Control Cell Shape and Rearrangements in Collective Cell Migration. Physical Review X 10, 011016.
- (104) Petridou, N. I., Grigolon, S., Salbreux, G., Hannezo, E., and Heisenberg, C.-P. (2019). Fluidization-mediated tissue spreading by mitotic cell rounding and non-canonical Wnt signalling. *Nature Cell Biology* 21, 169–178.

(105) Mongera, A., Rowghanian, P., Gustafson, H. J., Shelton, E., Kealhofer, D. A., Carn, E. K., Serwane, F., Lucio, A. A., Giammona, J., and Campàs, O. (2018). A fluid-to-solid jamming transition underlies vertebrate body axis elongation. Nature 561, 401–405.

- (106) Jain, A., Ulman, V., Mukherjee, A., Prakash, M., Cuenca, M. B., Pimpale, L. G., Münster, S., Haase, R., Panfilio, K. A., Jug, F., Grill, S. W., Tomancak, P., and Pavlopoulos, A. (2020). Regionalized tissue fluidization is required for epithelial gap closure during insect gastrulation. *Nature Communications* 11, 5604.
- (107) Saadaoui, M., Rocancourt, D., Roussel, J., Corson, F., and Gros, J. (2020). A tensile ring drives tissue flows to shape the gastrulating amniote embryo. Science 367, 453–458.
- (108) Tetley, R. J., Staddon, M. F., Heller, D., Hoppe, A., Banerjee, S., and Mao, Y. (2019). Tissue fluidity promotes epithelial wound healing. *Nature Physics* 15, 1195–1203.
- (109) Oswald, L., Grosser, S., Smith, D. M., and Käs, J. A. (2017). Jamming transitions in cancer. *Journal of Physics D: Applied Physics* 50, 483001.
- (110) Kim, S., Pochitaloff, M., Stooke-Vaughan, G. A., and Campàs, O. (2021). Embryonic tissues as active foams. *Nature Physics* 17, 859–866.
- (111) Petridou, N. I., Corominas-Murtra, B., Heisenberg, C.-P., and Hannezo, E. (2021). Rigidity percolation uncovers a structural basis for embryonic tissue phase transitions. *Cell* 184, 1914–1928.e19.
- (112) Sens, P., and Plastino, J. (2015). Membrane tension and cytoskeleton organization in cell motility. *Journal of Physics: Condensed Matter* 27, 273103.
- (113) Winklbauer, R. (2019). Dynamic cell-cell adhesion mediated by pericellular matrix interaction a hypothesis. *Journal of Cell Science* 132, jcs231597.
- (114) Caicedo-Carvajal, C. E., Shinbrot, T., and Foty, R. A. (2010).  $\alpha 5\beta 1$  Integrin-Fibronectin Interactions Specify Liquid to Solid Phase Transition of 3D Cellular Aggregates. *PLoS ONE 5*, e11830.
- (115) Krens, S. F. G., Veldhuis, J. H., Barone, V., Čapek, D., Maître, J.-L., Brodland, G. W., and Heisenberg, C.-P. (2017). Interstitial fluid osmolarity modulates the action of differential tissue surface tension in progenitor cell segregation during gastrulation. Development (Cambridge, England) 144, 1798–1806.
- (116) Fagotto, F. (2020). Tissue segregation in the early vertebrate embryo. Seminars in Cell & Developmental Biology 107, 130–146.
- (117) Sharrock, T. E., and Sanson, B. (2020). Cell sorting and morphogenesis in early Drosophila embryos. Seminars in Cell & Developmental Biology 107, 147–160.
- (118) Miller, P. W., Clarke, D. N., Weis, W. I., Lowe, C. J., and Nelson, W. J. (2013). The Evolutionary Origin of Epithelial Cell-Cell Adhesion Mechanisms. Current topics in membranes 72, 267–311.
- (119) Abedin, M., and King, N. (2008). The Premetazoan Ancestry of Cadherins. Science 319, 946–948.
- (120) Guirao, B., and Bellaïche, Y. (2017). Biomechanics of cell rearrangements in Drosophila. Current Opinion in Cell Biology 48, 113–124.

(121) Barone, V., Lang, M., Krens, S. G., Pradhan, S. J., Shamipour, S., Sako, K., Sikora, M., Guet, C. C., and Heisenberg, C.-P. (2017). An Effective Feedback Loop between Cell-Cell Contact Duration and Morphogen Signaling Determines Cell Fate. Developmental Cell 43, 198–211.e12.

- (122) Shaya, O., Binshtok, U., Hersch, M., Rivkin, D., Weinreb, S., Amir-Zilberstein, L., Khamaisi, B., Oppenheim, O., Desai, R. A., Goodyear, R. J., Richardson, G. P., Chen, C. S., and Sprinzak, D. (2017). Cell-Cell Contact Area Affects Notch Signaling and Notch-Dependent Patterning. Developmental Cell 40, 505–511.e6.
- (123) Slováková, J., Sikora, M., Arslan, F. N., Caballero-Mancebo, S., Krens, S. F. G., Kaufmann, W. A., Merrin, J., and Heisenberg, C.-P. (2022). Tension-dependent stabilization of E-cadherin limits cell–cell contact expansion in zebrafish germ-layer progenitor cells. *Proceedings of the National Academy of Sciences 119*, e2122030119.
- (124) Lenne, P.-F., Rupprecht, J.-F., and Viasnoff, V. (2021). Cell Junction Mechanics beyond the Bounds of Adhesion and Tension. *Developmental Cell* 56, 202–212.

# Single cell micro-pillar-based characterization of endothelial and fibroblast cell mechanics

Mechanotransduction, the ability of cells to sense and respond to the mechanical cues from their microenvironment, plays an important role in numerous cellular processes, ranging from cell migration to differentiation. Several techniques have been developed to investigate the underlying mechanisms of mechanotransduction, in particular, force measurement-based techniques. However, we still lack basic single cell quantitative comparison on the mechanical properties of commonly used cell types, such as endothelial and fibroblast cells. Such information is critical to provide a precedent for studying complex tissues and organs that consist of various cell types. In this short communication, we report on the mechanical characterization of the commonly used endothelial and fibroblast cells at the single cell level. Using a micropillar-based assay, we measured the traction force profiles of these cells. Our study showcases differences between the two cell types in their traction force distribution and morphology. The results reported can be used as a reference and to lay the groundwork for future analysis of numerous disease models involving these cells.

**Eckert, J.**, Abouleila, Y., Schmidt, T., and Mashaghi, A. (2021). Single Cell Micro-Pillar-Based Characterization of Endothelial and Fibroblast Cell Mechanics, *Micro* 1, 242-249.

2.1 Introduction 35

#### 2.1 Introduction

Mechanics is a fundamental property of biological cells with implications for various biological functions, ranging from single cell migration to organlevel functions, such as tissue barrier integrity regulation. The emergence of bio-printed and organ on chip models was a response to the need for modeling of mechanical alterations in numerous diseases (1). In particular, mechanical dysregulation of endothelial cells is involved in several functions and is attributed to various conditions including, autoimmune vasculopathies, viral hemorrhagic syndromes, allergic reactions, and cancer. Similar to endothelial cells, mechanical regulation of fibroblasts is involved in various cellular functions. Among these are, extracellular matrix (ECM) remodeling (2), tissue regeneration (3) and angiogenesis (4). Mechanotransduction has been closely linked to inflammation, wound healing and fibrosis (5, 6). There is increasing evidence that mechanical forces heavily influence all phases of wound healing, ranging from post-injury inflammation to fibrosis (7). Mechanical cues from the microenvironment modulate vascular endothelium permeability and ECM synthesis. Stresses from the microenvironment are then translated to adhesion forces created between cells, and cellular traction forces applied on the ECM (8, 9). Traction forces generated by the actomyosin machinery contribute to the cellular mechanical properties, and they are believed to play pivotal roles in regulating various cellular mechanosensing processes, such as cell differentiation, migration and proliferation.

Several approaches attempted to characterize the cellular traction forces. One pronounced methodology is micropillar array substrates. Through selective coating of the tips of the pillars with ECM proteins, cells are allowed to adhere and exert forces on them, which results in pillar deflections that correspond to intracellular traction forces. Here, we build upon our recent work and developed an in vitro assay to quantitatively compare the mechanical properties of two cell types, endothelial cells and fibroblasts at the single cell scale. We characterized two commonly used cell models, the human umbilical vein endothelial cells (HUVECs) and 3T3 fibroblast cells. Both are established models for studying fibroblast and vascular biology in health and disease (10). Our results showcase discrepancies in the distribution of traction forces among the two cell types. Endothelial cells appeared to exert lower traction forces on the ECM substrate when compared to fibroblast cells. Additionally, differences in cellular morphology were observed, where a lower cell-eccentricity was detected in endothelial cells in comparison to fibroblast cells. Both cell types exert dipolar forces, however, an additional three-fold symmetry was identified for fibroblast cells

in certain cell-eccentricity ranges.

### 2.2 Results

# 2.2.1 Endothelial cells apply less traction forces compared to fibroblast cells

Previously, we have shown that the total traction force of single 3T3 fibroblast cells exerted on fibronectin-coated micropillars is proportional to the number of deflected pillars (11). To validate this behavior for endothelial cells, we measured the traction force of 133 HUVEC cells (Fig.2.1A). The force correlated highly to the number of deflected pillars per cell with a correlation coefficient of r=0.9 (Fig.2.1B). The linear dependence between the number of deflected pillars and the total traction force results in a single parameter for cellular traction force characterizations, the mean traction force per deflected pillar.

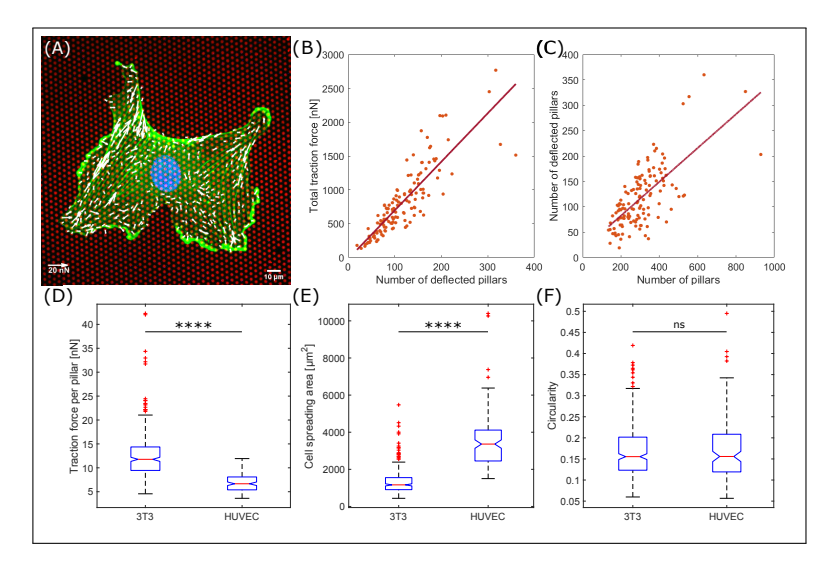


Figure 2.1: Traction forces are significantly higher for fibroblasts compared to endothelial cells. (A), A single endothelial cell on fibronectin-coated micropillars (red) showing F-actin (green), the nucleus (blue) and traction forces (white). (B), Total traction force per endothelial cell as a function of the number of deflected pillars. (C), Number of deflected pillars per endothelial cell correlated with the number of pillars per cell. (D), Mean traction force per deflected pillar per cell for fibroblasts and endothelial cells. (E), Cell spreading area. (F), Circularity. ns = not significant; \*\*\*\*\* p < 0.0001 using the two-sided Wilcoxon rank sum test.

For HUVEC cells, we measured a mean traction force per pillar of 6.9  $\pm$  1.9 nN (mean  $\pm$  s.d.) (Fig.2.1D). This value is significantly smaller than

2.2 Results 37

the averaged force per pillar of 12.6  $\pm$  5.2 nN (mean  $\pm$  s.d.) applied by 3T3 fibroblasts (p < 0.0001). We should note, that the number of deflected pillars for the HUVEC cells correlated with the total number of pillars per cell (r = 0.7), i.e., the cell spreading area (Fig.2.1C), a result that we reported also for fibroblasts earlier (11). The averaged cell spreading area was significantly higher for HUVEC cells with 3542  $\pm$  1486  $\mu$ m<sup>2</sup> (mean  $\pm$  s.d.) compared to 3T3 fibroblasts with 1328  $\pm$  673  $\mu$ m<sup>2</sup> (mean  $\pm$  s.d.) (Fig.2.1E).

# 2.2.2 Averaged force dipole distribution is independent of cell type

It is known that non-rounded cells generate force dipoles due to the contractility of their actomyosin machinery (12, 13). In round-shaped cells, forces are uniformly applied on substrates and mainly distributed at the cell-periphery (14). We measured the positions of deflected pillars according to the cell morphology. The cell spreading morphology was characterized by the moments-of-inertia of the cell shape approximated by an ellipse (Fig.2.2A endothelial cells, Fig.2.2D fibroblasts). With respect to the minor axis of the ellipse, we measured the angular position of the deflected pillars around the nucleus (Fig.2.2B endothelial cells, 15,682 deflections, Fig.2.2E fibroblasts, 8824 deflections). Both distribution of the angular positions for 133 analyzed endothelial cells and 323 fibroblasts show two peaks at an angular distance of 180°, hence located at the ends of the major axes. Together with the high eccentricities of both cell lines (Fig.2.2C endothelial cells; Fig.2.2F fibroblasts), the data show that both, endothelial cells and fibroblast cells, generally form force-dipoles.

It should be noted that the distributions around the main peaks in endothelial cells are broader compared to those of fibroblasts, indicating a difference in the cell spreading morphology. Endothelial cells are less elongated and tend to be rounder (Fig.2.2C). In contrast, fibroblast cells are more elongated (Fig.2.2F) and form narrow force dipoles (Fig.2.2E), which can be seen from the high probability distribution for larger eccentricities. Furthermore, we did not observe significant difference in circularity between 3T3 fibroblasts with 0.17  $\pm$  0.06 (mean  $\pm$  s.d.) and HUVEC cells with 0.17  $\pm$  0.08 (mean  $\pm$  s.d.) (Fig.2.1F).

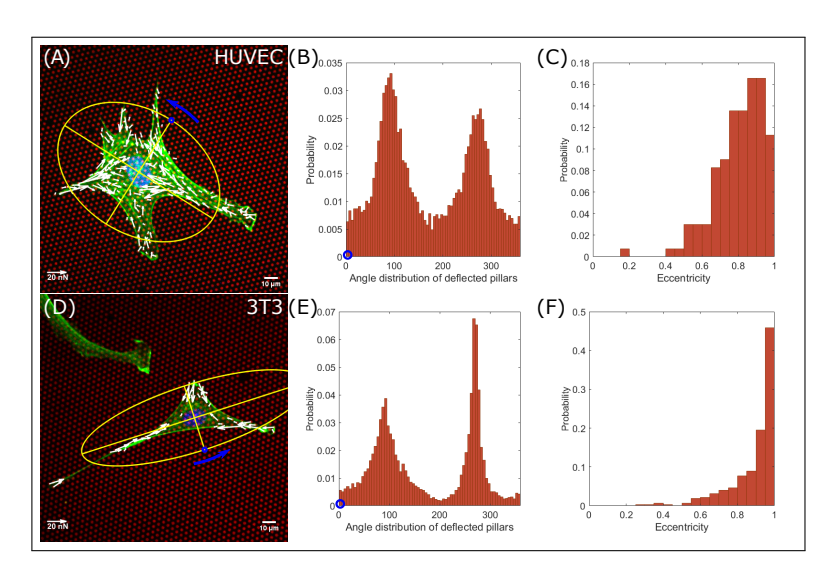


Figure 2.2: Endothelial cells and fibroblasts have dipolar force distributions. Angular distribution of deflected pillars and morphology analysis of endothelial cells (A-C) and fibroblast cells (D-F). (A,D), Single cells on fibronectin-coated micropillars (red) showing F-actin (green), the nucleus (blue) and traction forces (white). The cell spreading morphology was characterized by the moment of inertia of an ellipse (yellow). (B,E), Distributions of deflected pillars were assigned by counterclockwise rotation around the nucleus, starting at the short axis (blue circle). (C,F), Probability distributions of eccentricities.

# 2.2.3 Force pole is cell morphology and cell type dependent

As a next step, we investigated the dependence of the force distribution on the cell morphology in more detail. We compared the polarity of endothelial cells and fibroblast cells with their eccentricity for similarities and differences (Fig.2.3A–C endothelial; Fig.2.3D–F fibroblast). First, we investigated whether we could subtract the triangular shape of fibroblast cells from our data (15). We plotted the angular distribution for different eccentricities,  $\epsilon$ , and identified three peaks at an eccentricity range between 0.8 and 0.9 (Fig.2.3E, orange arrows, 54 cells, 1650 deflections), indicating a three-pole force distribution.

In comparison, highly elongated cells,  $0.9 < \epsilon \le 1$ , exerted mainly traction forces on their major axes, forming sharp force dipoles (Fig.2.3F, 211 cells, 5691 deflections). Endothelial cells, in contrast, retained their dipole distribution in all eccentricity-ranges, even when the distribution became more uniform for rounder cells ( $0.8 < \epsilon \le 0.9$ : 40 cells, 5436 deflections;  $0.9 < \epsilon \le 1$ : 37 cells, 3888 deflections).

2.3 Discussion 39

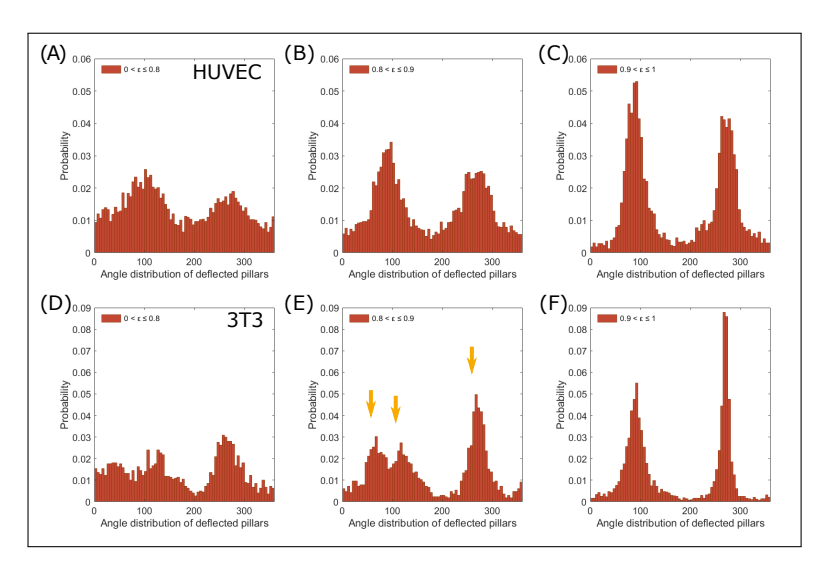


Figure 2.3: The force distribution pattern depends on the eccentricity of cells. Angular distribution of deflected pillars according to different eccentricities,  $\epsilon$ , of endothelial cells (A-C) and fibroblast cells (D-F). Endothelial cells retain two distribution peaks for all shown eccentricity ranges. Fibroblast cells show three deflection peaks (yellow arrows) at  $0.8 < \epsilon \le 0.9$  (E) and two peaks at  $0.9 \epsilon \le 1$  (F).

# 2.3 Discussion

Cellular mechanics is far from being homogenous across different cells. Mechanical heterogeneities of cells have been reported to largely influence several cellular processes, including response and resistance to treatment, mechanotransduction and tumor metastasis (16). As such, studying the mechanical properties of individual cells is a prerequisite to provide relevant insights into the prevention and treatment of disease. Here, using a micropillar-based assay, we quantitively describe the traction forces exerted by single endothelial cells and compared those to fibroblast cells. We identified particular differences between both cell types according to their traction force distribution and morphology. Endothelial cells were found to exert overall lower traction forces on the ECM substrate (mean traction force of  $6.9 \pm 1.9$  nN) when compared to fibroblasts ( $12.6 \pm 5.2$  nN). This may result from endothelial cells seeking cell-cell connections necessary for network formation, and hence resulting in stronger cell-cell adhesion forces, rather than cell-substrate adhesion. In addition, it was reported earlier that traction forces scale with focal adhesion areas (17-21). Therefore, compared to fibroblasts, endothelial cells might create less focal adhesions, which means that less traction forces are applied on substrates. Despite this, endothelial network formation relies on a balance between cell-cell and cell-substrate force interactions (22). While, in the case of fibroblast cells, stronger cell-substrate interactions are expected, given that fibroblasts are known to be largely responsible for ECM synthesis and remodeling (23). We further identified a significant heterogeneity in the mean force per pillar in both endothelial and fibroblast cells. The heterogeneity in cell binding to the ECM as dictated by specific cell-ECM interactions will contribute to specific ECM remodeling, that is subsequently resulting in the structural heterogeneity of the ECM (24).

Regarding to the cellular morphology, individual endothelial cells appeared to be more circular in their morphology when compared to fibroblasts. These morphological differences, quantified here as the cells' eccentricity, were found to be reflected in the angular force distribution as well. A broader force distribution pattern was detected in case of endothelial cells when compared to fibroblasts, indicating a difference in cell spreading morphology. Both cells exhibited a dipolar force distribution, which corroborates previous studies, that migrating cells (e.g., endothelial cells and fibroblasts) demonstrate a dipolar behavior (25). In addition, we observed a tri-polar force distribution specific to fibroblasts at a narrow eccentricity range (0.8 to 0.9). We speculate that the correlation of the force distribution-pattern with cellular morphology could lead to guide the directionality of cell movements, an insight that may be important for the mechanism of cell migration.

In conclusion, the micropillar-based assay reported here provides a reference for single-cell mechanical data for two commonly used cell types, HUVEC cells and 3T3 fibroblasts. We believe that our results will be of interest for future studies on the mechanics of complex tissues and organs involving these cell models. Recent studies showed a possible link between endothelial cells and fibroblasts functions in events like, inflammation and wound healing (26, 27). Thus, this assay and our data can be extended further to include cell-cell interactions to help understand how endothelial cells and fibroblasts interact and coordinate their dynamics during said events.

# 2.4 Materials and methods

#### Cell culture

3T3 fibroblast cells were cultured in high-glucose Dulbecco Modified Eagle's Medium (D6546; Sigma-Aldrich, St. Louis, MO, USA) supplemented with 10% fetal calf serum (Thermo Fisher Scientific, Waltham, MA, USA),  $2\,\mathrm{mM}$ 

glutamine, and 100 mg/mL penicillin/streptomycin, 37 °C, 5% CO<sub>2</sub>. For HUVECs, cells were cultured in Endothelial Cell Basal Medium 2 (Promo-Cell, C-22211) and supplemented with Growth Medium 2 SupplementMix (PromoCell, C-39216) and 100 mg/mL penicillin/streptomycin.

#### **Immunostaining**

After 22.5 h of spreading, 3T3 fibroblast and HUVEC cells were fixed for 15 min in 4% paraformaldehyde (43368; Alfa Aesar, Haverhill, MA, USA) in phosphate-buffered saline (PBS). Furthermore, cells were permeabilized for 10 min with 0.1% Triton-X 100 in 1% bovine serum albumin (BSA) and blocked for 60 min with 1% BSA in PBS. F-actin was stained with Alexa Fluor 532-labeled phalloidin (A22282; Invitrogen, Carlsbad, CA, USA) and the DNA with DAPI (Sigma-Aldrich).

#### Elastic micropillar arrays

Polydimethylsiloxane (PDMS, Sylgard 184) micropillar arrays of 2 µm diameter, 6.9 µm length, and 4 µm spacing in a hexagonal geometry were used for cell traction force experiments. The pillar arrays were flanked by 50 µm spacers on two sides of the array. Details of this arrangement and the experimental procedures were described earlier in detail (28). In brief, pillar arrays were produced on a negative silicon-wafer master made by a two-step deep reactive-ion etching process. Wafers were passivated in trichloro-silane (448931; Sigma-Aldrich). A mixture of 1:10 PDMS (cross-linker/base ratio) was poured onto the Si-master and cured for 20 h at 110 °C. After peeling off, the tops of the pillars were coated by micro-contact printing. For that, flat 1:30 PDMS stamps were incubated for 1 h with 40 mL of 50 mg/mL Alexa Fluor 647-labeled and 50 mg/mL unlabeled fibronectin (F1141; Sigma-Aldrich), then washed and dried. Subsequently, the stamps were gently loaded onto the ultraviolet-ozone-activated micropillar arrays for 10 min. After stamping, the arrays were passivated with 0.2% Pluronic (F-127, P2443; Sigma-Aldrich) for 1 h, and washed in PBS.

## Microscopy

Samples were imaged at high resolution on a home-build optical microscope setup based on an inverted Axiovert200 microscope body (Carl Zeiss, Oberkochen, Germany), a spinning disk unit (CSU-X1; Yokogawa Electric, Musashino, Tokyo, Japan), and an emCCD camera (iXon 897; Andor Labs, Morrisville, NC, USA). IQ-software (Andor Labs) was used for setup-control and data acquisition. Illumination was performed using fibercoupling of different lasers (405 nm (CrystaLaser, Reno, NV, USA), 514

nm (Cobolt AB, Solna, Sweden), and 642 nm (Spectra-Physics Excelsior; Spectra-Physics, Stahnsdorf, Germany)). Pillar arrays were placed upside down onto 25 mm cover glasses and inspected with an EC Plan-NEOFLUAR  $40 \times 1.3$  Oil Immersion Objective (Carl Zeiss).

#### Image analysis

Images of single, nonoverlapping and randomly selected cells within the field of view of  $176 \times 176~\mu m$  were analyzed using MATLAB scripts (MATLAB R2018a; MathWorks, Natick, MA, USA). Pillar deflections were quantified as previously described in detail (28). Deflected pillars caused by cell traction forces were distinguished from the background. The background was determined from an undeflected area of the pillar array by selecting a pillar region outside the cell area. Pillar deflections underneath the cell within the background range were excluded.

The cell spreading morphology was characterized by the moment of inertia of an ellipse using the Regionprops function in MATLAB. In respect to the minor axis of the ellipse, we measured the angular position  $(0^{\circ}$  to  $360^{\circ})$  of the deflected pillars around the nucleus. The angular position  $0^{\circ}$  was chosen in such a way that most deflected pillars were close to the major axis at  $270^{\circ}$  and less at  $90^{\circ}$  (Fig.2.2D).

#### Statistics

In total, we analyzed 133 HUVEC cells from eight samples of four independent performed experiments and 323 3T3 fibroblasts from six independent samples.

All data sets are of non-normal distribution. The p-values were calculated using the two-sided Wilcoxon rank sum test in MATLAB. Data sets were significantly different with probabilities of p < 0.0001 (\*\*\*\*); p > 0.05 (ns).

#### Author contributions

Cell culture and sample preparation of 3T3 cells, J.E.; microfabrication of micropillar arrays, data analysis, J.E.; cell culture and sample preparation of HUVECs, Y.A.; manuscript writing, J.E., Y.A. and A.M.; supervising the project, T.S. and A.M. All authors have read and agreed to the published version of the manuscript.

### **Funding**

This research was funded by Leiden University Fund grant number W19340-5-EML and the Netherlands Organisation for Scientific Research grant numbers NWA.1228.191.329 and OCENW.XS4.180.

#### Institutional review board statement

The study was conducted according to the guidelines of the Declaration of Helsinki.

#### Informed consent statement

Not applicable.

### Data availability statement

The original data are available on reasonable request to the corresponding author.

#### Conflicts of interest

The authors declare no conflict of interest. The funders had no role in the design of the study; in the collection, analyses, or interpretation of data; in the writing of the manuscript, or in the decision to publish the results.

- Evers, T. M. J., Holt, L. J., Alberti, S., and Mashaghi, A. (2021). Reciprocal regulation of cellular mechanics and metabolism. *Nature Metabolism 3*, 456–468.
- (2) Leslie, M. N., Chou, J., Young, P. M., Traini, D., Bradbury, P., and Ong, H. X. (2021). How Do Mechanics Guide Fibroblast Activity? Complex Disruptions during Emphysema Shape Cellular Responses and Limit Research. *Bioengineering* 8.
- (3) Li, B., and Wang, J. H.-C. (2011). Fibroblasts and myofibroblasts in wound healing: force generation and measurement. *Journal of tissue viability* 20, 108– 120.
- (4) Sorrell, J. M., Baber, M. A., and Caplan, A. I. (2007). A Self-Assembled Fibroblast-Endothelial Cell Co-Culture System That Supports in vitro Vasculogenesis by both Human Umbilical Vein Endothelial Cells and Human Dermal Microvascular Endothelial Cells. Cells Tissues Organs 186, 157–168.
- (5) Chaudhuri, O., Cooper-White, J., Janmey, P. A., Mooney, D. J., and Shenoy, V. B. (2020). Effects of extracellular matrix viscoelasticity on cellular behaviour. *Nature* 584, 535–546.
- (6) Henderson, N. C., Rieder, F., and Wynn, T. A. (2020). Fibrosis: from mechanisms to medicines. *Nature* 587, 555–566.
- (7) Kuehlmann, B., Bonham, C. A., Zucal, I., Prantl, L., and Gurtner, G. C. (2020). Mechanotransduction in Wound Healing and Fibrosis. *Journal of clinical medicine* 9, 1423.
- (8) Arslan, F. N., Eckert, J., Schmidt, T., and Heisenberg, C.-P. (2021). Holding it together: when cadherin meets cadherin. *Biophysical Journal* 120, 4182–4192.
- (9) Lemmon, C. A., Sniadecki, N. J., Ruiz, S. A., Tan, J. L., Romer, L. H., and Chen, C. S. (2005). Shear force at the cell-matrix interface: enhanced analysis for microfabricated post array detectors. *Mechanics & chemistry of biosystems :* MCB 2, 1–16.
- (10) Medina-Leyte, D. J., Domínguez-Pérez, M., Mercado, I., Villarreal-Molina, M. T., and Jacobo-Albavera, L. (2020). Use of Human Umbilical Vein Endothelial Cells (HUVEC) as a Model to Study Cardiovascular Disease: A Review. Applied Sciences 10.
- (11) Eckert, J., van Loon, J. J. A., Eng, L. M., and Schmidt, T. (2021). Hypergravity affects cell traction forces of fibroblasts. *Biophysical Journal* 120, 773–780.
- (12) Dembo, M., and Wang, Y.-L. (1999). Stresses at the Cell-to-Substrate Interface during Locomotion of Fibroblasts. *Biophysical Journal* 76, 2307–2316.

(13) Schwarz, U. S., and Safran, S. A. (2002). Elastic Interactions of Cells. Phys. Rev. Lett. 88, 048102.

- (14) Abuhattum, S., Gefen, A., and Weihs, D. (2015). Ratio of total traction force to projected cell area is preserved in differentiating adipocytes. *Integrative biology* : quantitative biosciences from nano to macro 7 10, 1212–7.
- (15) Abercrombie, M. (1978). Fibroblasts. Journal of clinical pathology. Supplement (Royal College of Pathologists) 12, 1–6.
- (16) Li, X., Das, A., and Bi, D. (2019). Mechanical Heterogeneity in Tissues Promotes Rigidity and Controls Cellular Invasion. Phys. Rev. Lett. 123, 058101.
- (17) Balaban, N. Q., Schwarz, U. S., Riveline, D., Goichberg, P., Tzur, G., Sabanay, I., Mahalu, D., Safran, S., Bershadsky, A., Addadi, L., and Geiger, B. (2001). Force and focal adhesion assembly: a close relationship studied using elastic micropatterned substrates. *Nature Cell Biology* 3, 466–472.
- (18) Tan, J. L., Tien, J., Pirone, D. M., Gray, D. S., Bhadriraju, K., and Chen, C. S. (2003). Cells lying on a bed of microneedles: An approach to isolate mechanical force. Proceedings of the National Academy of Sciences 100, 1484–1489.
- (19) Shemesh, T., Geiger, B., Bershadsky, A. D., and Kozlov, M. M. (2005). Focal adhesions as mechanosensors: A physical mechanism. *Proceedings of the National* Academy of Sciences 102, 12383–12388.
- (20) Trichet, L., Le Digabel, J., Hawkins, R. J., Vedula, S. R. K., Gupta, M., Ribrault, C., Hersen, P., Voituriez, R., and Ladoux, B. (2012). Evidence of a large-scale mechanosensing mechanism for cellular adaptation to substrate stiffness. Proceedings of the National Academy of Sciences 109, 6933–6938.
- (21) Balcioglu, H. E., van Hoorn, H., Donato, D. M., Schmidt, T., and Danen, E. H. J. (2015). The integrin expression profile modulates orientation and dynamics of force transmission at cell–matrix adhesions. *Journal of Cell Science* 128, 1316– 1326.
- (22) Califano, J. P., and Reinhart-King, C. A. (2010). Exogenous and endogenous force regulation of endothelial cell behavior. *Journal of biomechanics* 43 1, 79–86.
- (23) Rhee, S., and Grinnell, F. (2007). Fibroblast mechanics in 3D collagen matrices. Advanced drug delivery reviews 59, 1299–1305.
- (24) Malandrino, A., Mak, M., Kamm, R. D., and Moeendarbary, E. (2018). Complex mechanics of the heterogeneous extracellular matrix in cancer. Extreme Mechanics Letters 21, 25–34.
- (25) Mandal, K., Wang, I., Vitiello, E., Orellana, L. A. C., and Balland, M. (2014). Cell dipole behaviour revealed by ECM sub-cellular geometry. *Nature Communications* 5, 5749.
- (26) Slany, A., Bileck, A., Kreutz, D., Mayer, R. L., Muqaku, B., and Gerner, C. (2016). Contribution of Human Fibroblasts and Endothelial Cells to the Hallmarks of Inflammation as Determined by Proteome Profiling. *Molecular & Cellular Proteomics* 15, 1982–1997.
- (27) Tefft, J. B., Chen, C. S., and Eyckmans, J. (2021). Reconstituting the dynamics of endothelial cells and fibroblasts in wound closure. APL Bioengineering 5, 016102.

(28) van Hoorn, H., Harkes, R., Spiesz, E. M., Storm, C., van Noort, D., Ladoux, B., and Schmidt, T. (2014). The Nanoscale Architecture of Force-Bearing Focal Adhesions. *Nano Letters* 14, 4257–4262.

# Cell-Cell Separation Device: measurement of intercellular detachment forces

Whether at the intermolecular or cellular level in organisms, cell-cell adhesion adapts to external mechanical cues arising from the static environment of cells and from dynamic interactions between neighboring cells. Cell-cell adhesions need to resist to detachment forces to secure the integrity and internal organization of organisms. In the past decades, various techniques have been developed to characterize adhesion properties of molecules and cells in vitro, and to understand how they sense and probe their environment. Atomic force microscopy and dual pipette aspiration, where cells are mainly present in suspension, are common applications for studying detachment forces of cell-cell adhesions. How cell-cell adhesion forces are developed for adherent and environment-adapted cells is unclear. Here, we designed the Cell-Cell Separation Device (CC-SD), a substrate that measures both intercellular forces and external stresses of cells towards the matrix. The design is based on micropillar arrays for cell traction force measurements. We produced PDMS micropillar-blocks, on which cells adhered to and connected over the spacing. Controlled stretching changed the distance between the blocks and the applied strain at the cell-cell contact, resulting in cell-cell adhesion detachment, which was measured by pillar deflections. Our first experiments gave an insight into technical challenges to measure dynamic changes of cell-cell adhesions under stress. The CC-SD provided an increase of the gap between the blocks of up to 140%, which was sufficient to separate substrate-attached cells with fully developed F-actin network. Simultaneously measured pillar deflections resulted in cellular responds to the intercellular strain. Our novel CC-SD opens up possibilities for the analysis of intercellular force detachments and sheds light on the robustness of cell-cell adhesions in dynamic processes in tissue development.

This chapter is based on: **Eckert, J.**, Partel, S., Matylitskaya, V. , Kasemann, S., and Schmidt, T. Cell-Cell Separation Device – measurement of intercellular detachment forces. *In preparation*.

3.1 Introduction 51

#### 3.1 Introduction

Cells are dynamically in contact with each other and with the extracellular matrix (ECM). They experience external mechanical forces applied by neighboring cells and sense, individually or together, changes of the cellular environment, e.g. topography (1) and stiffness (2). The physical and passive interactions are converted into biochemical signals, which cause an active response followed by an alteration of cell-cell adhesion (3, These complex cell-cell adhesions have to resist detachment forces (5). Various techniques have been developed to characterize the properties of cells in vitro and to understand how they sense and probe their environment. These techniques and their further development for studying cell-cell adhesions have been described in detail in recent reviews (6-13). In most methodical approaches, like atomic force microscopy (14, 15) and dual pipette aspiration (16, 17), the detachment forces of cells were studied in a suspended form to avoid cell-ECM interactions. In the experiments, cells were brought into contact for a short period of time without developing an actin stress fiber network. Using other techniques such as Förster resonance energy transfer (FRET)-based tension sensors, traction force microscopy (TFM), and the micropillar array technology deal with spread cells on substrates and give an insight into the force and tension interactions of cells (18-23). The intercellular forces are predicted to be dependent on the ECM-property-dependent traction forces, cell spreading area and shape, cell-cell contact size, and on the cell type with its different cell-cell adhesion machinery. All these measurements were carried out in dynamical equilibrium and did not give information about detachment forces.

Here, we combined the ideas of measuring intercellular detachment forces of cells in the spread state with developed actin stress fibers by our novel device. Our Cell-Cell Separation Device (CC-SD) was able to obtain intercellular forces through traction force measurements of deflected micropillars. For this, the pillars were connected to PDMS-blocks on which cells adhered to and were allowed to connect across the gap. An applied stretch on a thin substrate underneath the blocks increased the distance between the cells until the cell-cell contact broke. Our first experiments gave an insight into technical challenges to measure dynamic changes of cell-cell adhesions under external stress. We demonstrated that our CC-SD provided a nominal strain at the cell-cell contact by an increase of the gap width between the blocks by up to 140%, i.e. 2.4-fold, which was sufficient to separate substrate-attached cells with fully developed actin stress fiber network. Simultaneously, pillar deflections caused by cell traction forces

gave information about the cellular responses to the intercellular strain. Our novel designed CC-SD opens up possibilities for the analysis of intercellular force detachments and sheds light on the robustness of cell-cell adhesions in dynamic processes in tissue development.

### 3.2 Results

# 3.2.1 The intercellular adhesion strength increases with an increase of the total traction force

Cells form doublets (Fig.3.1A) or larger clusters up to confluent monolayers, ultimately forming tissues that define the organism. The stability of such assembly is secured by the interplay of cell-matrix to cell-cell adhesions (4). At the single-cell level, where solely cell-matrix adhesion is important, it has been shown that the summed absolute traction force that individual 3T3 fibroblast cells exert on the extracellular matrix scales with the cell spreading area. Likewise, for cells on fibronectin-coated micropillars the total absolute traction force was found to increase proportional to the number of deflected pillars below the cell (24, 25). The question we asked here was, whether this linear scaling between interaction area and total absolute force prevails for cell assemblies, i.e. here for cell-doublets. In order to test the hypothesis, we cultured cells on flexible micropillars and analyzed the traction forces developed by the cell. Experiments were performed on 46 cell-doublets (Fig.3.1B-C). The total absolute traction force linearly increased with the number of deflected pillars for both the cell doublets and the 92 individual cells after forces were split and assigned to each cell. This relationship was identical for the doublet configuration as well as for individual cells (Fig.3.1D). The resulting mean absolute force per deflected pillar was calculated to be  $11.0 \pm 2.7$  nN for doublets, and  $10.9 \pm$ 3.4 nN (mean  $\pm \text{ s.d.}$ ) for individual cells of 3T3 fibroblasts on fibronectincoated pillars. Similar results have previously been obtained for single 3T3 fibroblasts ((25); Chapter 2).

The above measurements further allowed us to measure the forces that developed at cell-cell contacts (19). After partitioning the cell doublet into the two individual cells, we calculated the resultant force,  $F_c$ , for each cell, c1 and c2, summing up the individual traction forces,  $F_t$  (Fig.3.1E; Eqs.(3.7)). The resulting forces  $F_{c1}$  and  $F_{c2}$  were opposing, as required from Newton's law. Our results showed that the intercellular force (Eq.(3.8)) increased with the magnitude of the total traction force exerted by the doublet (Fig.3.1F). About 25% of the total traction force was accounted by the force between the cells. Therefore, we speculate that 25% of the active

3.2 Results 53

adhesion molecules are located at the cell-cell interface.

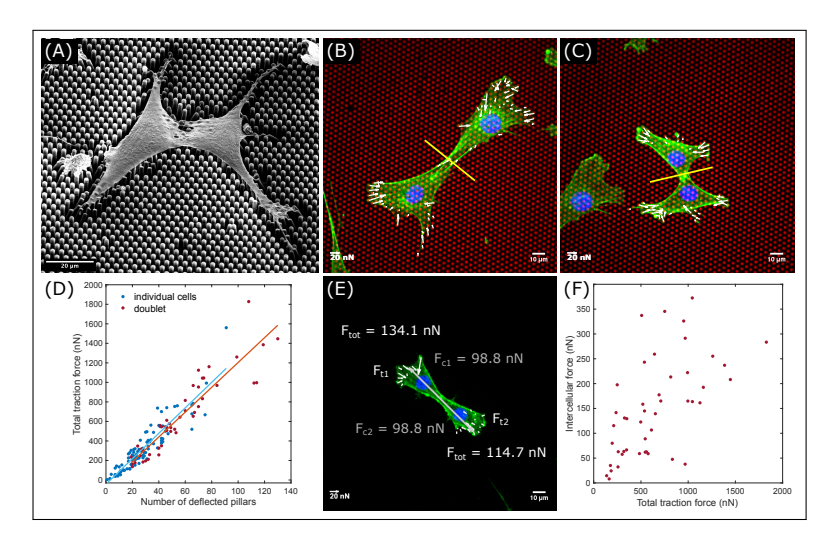


Figure 3.1: The intercellular force increases with the total traction force. (A), Scanning electron microscopy image of a 3T3 fibroblast cell doublet. (B,C), Two 3T3 cells connected to a cell-doublet exert traction forces (white arrows) on elastic micropillars. For the traction force analysis of each individual cell, the doublet was separated at the cell-cell contact (yellow line). Red: fibronectin-coated micropillars, green: F-actin, blue: nuclei. (D), Total traction force,  $F_{tot}$ , per doublet and each individual cell versus the number of deflected pillars. (E), Traction forces,  $F_t$  of each individual cell add up and result in the intercellular force contribution,  $F_c$ . (F), The intercellular force,  $F_{cc} = |F_{c1}| + |F_{c2}|$ , versus the total traction force per doublet. Correlation coefficient: r = 0.6.

# 3.2.2 Stretching a homogeneous elastic micropillar field causes deformations

In an organism, the static picture we analyzed in the previous subsection is invalid. The forces between cells and the extracellular matrix constantly change due to their activity, hence cell-cell adhesion needs to adapt in a dynamic way to keep tissue integrity. To test how cell-doublets and their individual cells adapt to dynamic mechanical challenges, we designed an experiment that included a dynamical stretch of the elastic micropillar array. Earlier it has been shown that the cell's cytoskeleton largely rearranged on a continued uniaxial stretch (26). Here, we used a similar approach to assess whether a uniaxial stretch would lead to a change in cell-cell adhesion forces, and whether we would be able to determine the forces that are sufficient to break a cell-cell contact. We cultured human melanoma MV3 cells on micropillar arrays and mounted arrays of thickness of  $\sim 100 \ \mu m$  with

two clamps in a linear stretcher on our microscope. The clamp-positions were electronically controlled (Fig.3.2A). We first characterize the resulting strain-fields for such homogeneous pillar arrays by analyzing the pillar positions with respect to the external strain applied. At 0% strain, i.e. in an unstretched position, the mean pillar-to-pillar distances was 3.87  $\pm$  0.18  $\mu m$  (mean  $\pm$  s.d.) (Fig.3.2B,D). When we applied the stretch in x-direction on the micropillar array, we identified a displacement of the pillars in both the x- and y-directions (Fig.3.2B-C). At 20% nominal strain, the pillar-to-pillar distance increased to 4.05  $\pm$  0.15  $\mu m$ , i.e. 4.6% in the stretch direction, and decreased to 3.79  $\pm$  0.09  $\mu m$  (mean  $\pm$  s.d.), i.e. -2.3% perpendicular to it (Fig.3.2D). The difference is predicted for an incompressible material like PDMS, for which the Poisson ratio  $\nu=0.5$ , and hence the strain relation (Eq.(3.6)) holds.

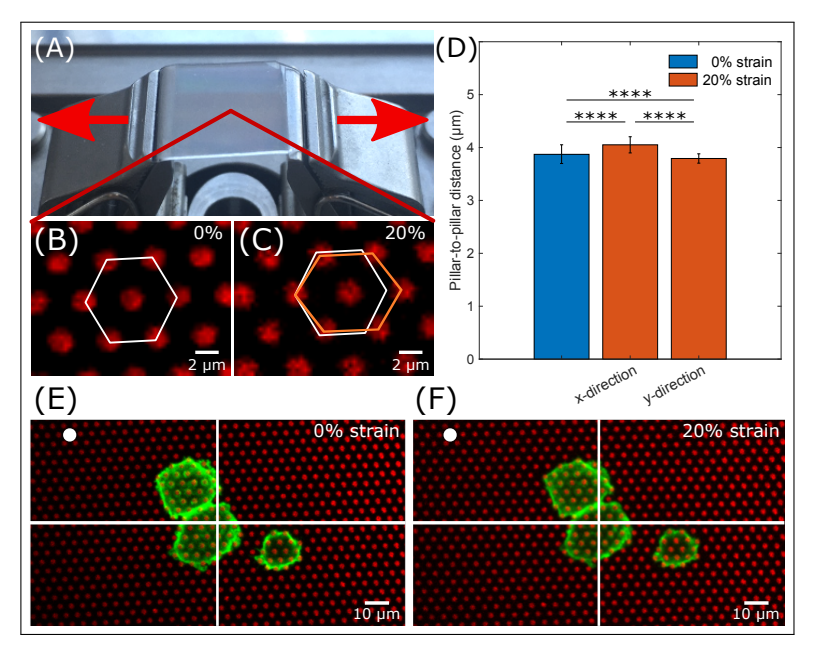


Figure 3.2: x-y displacement changes by less than 5%. (A), A 1x1 cm micropillar array mounted with two clamps. The horizontal stretch direction of the array is indicated by red arrows. (B), Top view of micropillars with hexagonal geometry in the unstretched position. (C), A strain of 20% on the pillar array caused a deformation of the substrate and thus an increase and decrease of the center-to-center distance in the x- and y-position, respectively, which is indicated by the orange hexagon. Scale bar: 2  $\mu$ m. (D), Pillar-to-pillar distances at 0% and 20% substrate strain in x-direction (n=40). (E,F), MV3 cells adhered to micropillars undergo substrate stretching and maintain stable cell-cell adhesions. The white dot represents the reference point of both images. Red: fibronectin-coated micropillars, green: F-actin. Two-sided Wilcoxon rank sum test: \*\*\*\* p < 0.0001.

3.2 Results 55

It is essential for the methodology of force measurements in micropillar assays that the positions of the undeflected pillars are known to high accuracy (27). When stretching the substrate, this accuracy might be deteriorated by, for example, pillar deformations and imperfections in the homogeneity of the PDMS polymer. Thus, we further characterized the background deflection field, i.e. excluding pillars covered by cells, of the micropillars on uniaxial stretch. For an unstretched array, the mean deflection was  $0.038 \pm 0.021~\mu m$  (mean  $\pm$  s.d.) (Fig.S3.7A). This accuracy was predicted from the total signal detected for each pillar on the CCD-detector of the microscope (27). At 20 % nominal substrate strain, the mean background deflection increased by 38% to  $0.061 \pm 0.033~\mu m$  (mean  $\pm$  s.d.) (Fig.S3.7B-C).

To check whether the applied substrate strain affected the traction force of cells, we focused on the pillar deflection analysis of single MV3 cell. These results need to be known in order to rule out the mechanical influence of substrate deformation on the intercellular force calculation. At 0% nominal strain, the mean deflection of the pillars was  $0.32\pm0.17~\mu m$  (mean  $\pm$  s.d.) and thus an order of magnitude higher than the background deflections (Fig.S3.7D). When the 20% nominal strain was applied, the mean deflection of  $0.34\pm0.26~\mu m$  (mean  $\pm$  s.d.) did not change compared to the unstretched position (Fig.S3.7E-F). The stretch of the micropillar and thus the deformation of the pillar field underneath the cell did not affect the mean traction forces of the MV3 cell.

These experiments demonstrated that the micropillar technology can be used to apply a defined stress/strain on both cells and cell assemblies, with the ability to simultaneously monitor the cellular force-response as monitored by the micropillar deflections. Yet, likewise, the results showed a severe limitation of this initial approach: the local strain field, reflected by the pillar-to-pillar displacement, that could be achieved was less than 5% on a nominal substrate stretch of 20%. Probably most of the strain was localized to areas of the substrate weakened by the clamps of the stretcher. The amount of strain that was realized on cells was not sufficient to challenge a cellular response, or even break the cell-cell contacts as shown for the MV3 cells in Fig.3.2E-F.

# 3.2.3 CC-SD: the Cell-Cell Separation Device

In order to break the cell-cell contact and simultaneously measure the maximum intercellular adhesion force between two cells adhered to substrates in a doublet configuration, we designed a substrate, the Cell-Cell Separation Device (CC-SD) (Fig.3.3A). The substrate is composed of PDMS blocks of

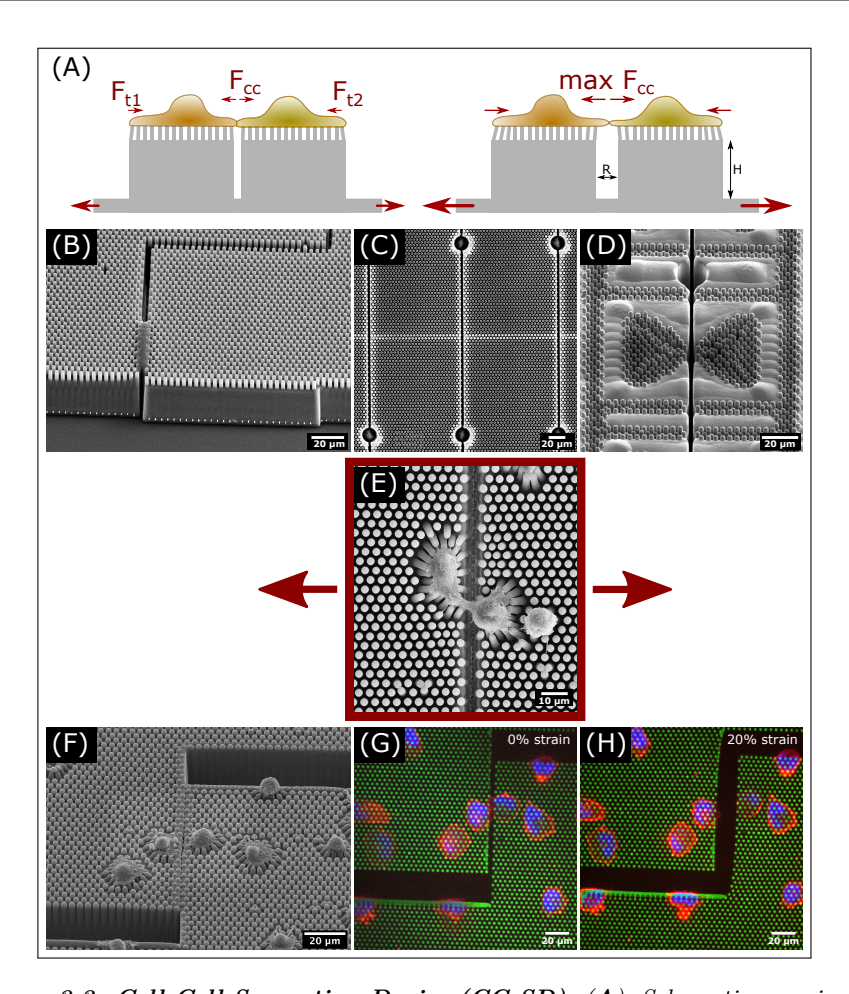


Figure 3.3: Cell-Cell Separation Device (CC-SD). (A), Schematic overview of the CC-SD. Two cells adhered on blocks of height, H, composed of micropillars and connect across a gap of width, R. Obtained traction forces,  $F_t$ , (Eqs.(3.7)) result in the intercellular forces,  $F_{cc}$  (Eq.(3.8)). By applying a stretch on the connected substrate, the gap width increases, resulting in an increase in pillar deflections, i.e. increase in pseudo-traction forces. At a certain strain, the cell-cell adhesions break and the maximum intercellular force can be obtained. (B), CC-SD in a zig-zag configuration for tensile and shear force measurements at the cell-cell contact. (C), Parallel gaps perpendicular to the stretch direction. (D), CC-SD with pillar fields in a butterfly configuration. The geometry of the wings controls the cell spreading area and contact length between the cells. (E), Two MV3 cells adhere across the gap. (F-H), CC-SD in a zig-zag configuration. An application of 20% strain is sufficient enough to break the cell-cell contact of MV3 cells. Green: fibronectin-coated micropillars, red: F-actin, blue: nuclei.

height, H, connected by a thin layer of PDMS at the bottom. On top of each block, a field of micropillars is located to which cells can adhere. The

3.2 Results 57

blocks are spaced in such a way that cells are allowed to connect across the gap of width, R (Fig.3.3E). An externally applied stretch on the thin layer localizes the strain to the gap and increases significantly the block distance, R. This eventually breaks the cell-cell contact.

Our novel design, although adding substantial challenges in the microfabrication process by deep reactive-ion etching (see materials and methods), allowed us to develop additional application modes, which make the CC-SD a versatile instrument. We developed and characterized four CC-SDs in different configurations (Fig.3.3B-D,F) whose specifications are summarized in Tab.S3.1. In one design, the gap was arranged perpendicular to the direction of stretching. That design allowed to apply tensile stress at the cell-cell contact during uniaxial stretching (Fig.3.3C). In a second and third design, the gap was arranged in a zig-zag pattern, allowing additional measurements of shear forces where the blocks separated parallel to the cell-cell contact length (Fig.3.3B). The pillars in the fourth design, inspired by (19), were arranged in a butterfly shape to adjust the cell spreading area and allowed the cell-cell contact length to be fixed (Fig.3.3D).

All CC-SDs were designed to be optimized for the cell lines we use in ongoing studies: the 3T3 fibroblast cell line and the MV3 melanoma cell line. As in the design of the homogeneous arrays we used earlier, the micropillar fields on top of the blocks consisted of pillars of  $\sim 2 \mu m$  diameter arranged in regular hexagonal patterns of  $\sim 4 \mu m$  center-to-center distance. The pillar height was adjusted to the range of suitable effective Young's moduli relevant to the two cell types. For a pillar height of 6.1 µm of the previously used micropillar array (effective Young's modulus: 29.5 kPa), 3T3 fibroblasts and MV3 cells were reported to apply a mean force per pillar of  $12.6 \pm 5.2$  nN ((25); Chapter 2) and  $19 \pm 6$  nN (mean  $\pm$  s.d.) (Fig.S3.6A), respectively. The initial gap width of all CC-SD substrates was set to 4 μm perpendicular to the direction of stretching, a length scale across which 3T3 and MV3 cells were able to span and adhere to each other (Fig. 3.3E; Fig. 3.4A). The area of the butterfly pattern was chosen to match the mean spreading area of the two cell lines, which was between 117  $\pm$  61 pillars and 122  $\pm$  85 pillars (mean  $\pm$  s.d.), respectively (Fig.S3.6B). Accordingly, we chose an area of each butterfly wing of 119 pillars.

We set the block height between 30  $\mu$ m to 40  $\mu$ m (Fig.3.3B). This height was sufficient to avoid pre-stretching our substrate while mounting. The strain on the CC-SD was mainly localized and applied in the region between the blocks. When we stretched the tensile CC-SD with the perpendicular gap, we identified a linear increase of the gap width of 0.43  $\pm$  0.06  $\mu$ m per nominal strain, i.e. from  $\sim$ 6  $\mu$ m at 0% stretch to  $\sim$ 16  $\mu$ m at 20% nominal

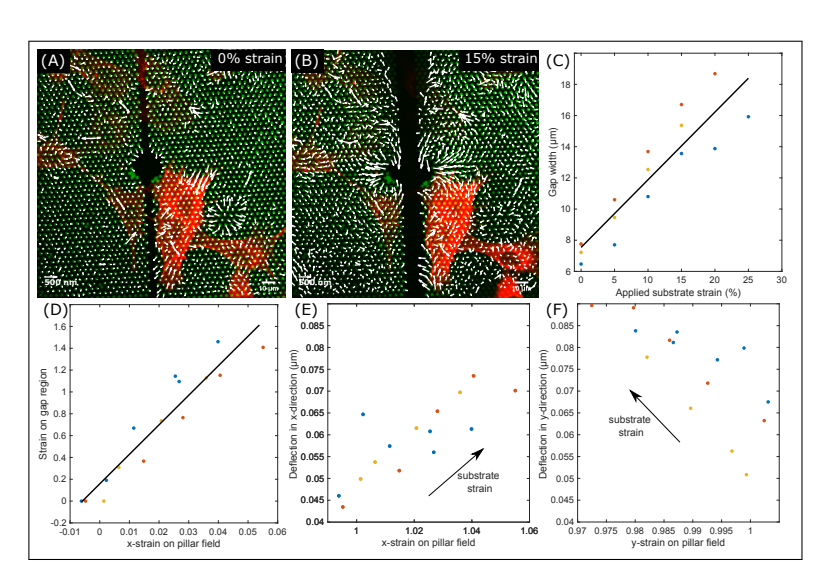


Figure 3.4: Tensile CC-SD. (A,B), CC-SD with the gap perpendicular to the stretch direction, showing 3T3 fibroblasts and the pillar deflection field (white arrows) at 0% and 15% substrate strain. Green: fibronectin-coated micropillars, red: F-actin. (C), By applying a strain on the substrate, the width of the gap increases (n=3). (D), The strain on the gap region is  $27.04 \pm 2.54$  bigger than the deformation on the pillar field. (E,F), The magnitude of the computed pillar deflections in x- and y-directions increase with increasing substrate strain. The stain on the substrate causes an elongation (increased strain) of the pillar field in x-direction (E) and a compression (decreased strain) in y-direction (F).

stretch (Fig.3.4C). Furthermore, we compared the strain in x-direction of the pillar field with the strain on the gap region (Fig.3.4D). The gap width increased by  $27.04 \pm 2.54$  times the pillar-to-pillar distance. In comparison to the tensile stretch of 4.6% of the pillar array (Fig.3.2D-F), the gap width increased by 140.2%, i.e. 2.4-fold.

As shown for the micropillar array above, the substrate deformation caused by the nominal substrate strain affected the accuracy of pillar detections. We showed that the magnitude of the pillar deflections in x- and y-direction increased with increasing substrate strain (Fig.S3.7C). We now wanted to confirm whether the earlier result likewise holds for the CC-SD substrate. For that, we computed the pillar deflections for each nominal substrate strain applied (Fig.3.4E-F). Again, we found an increase of the pillar deflections in x- and y-direction with increasing nominal stretch, which further correlated with the elongation and compression of the substrate, respectively. One example of 3T3 fibroblasts cultured on the tensile CC-SD is shown in Fig.3.5A-B. Two cells adhered to each other across the gap and were stretched by increasing gap width. The mean deflections of

3.2 Results 59

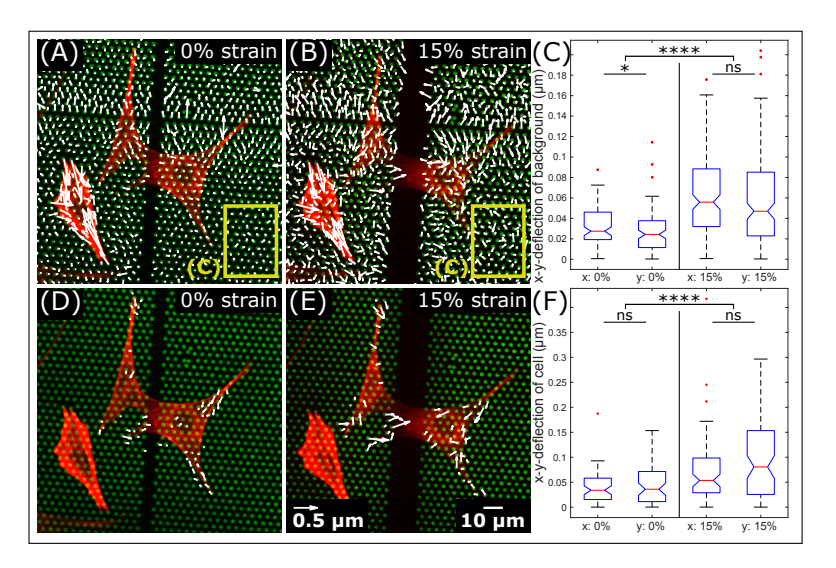


Figure 3.5: Traction forces of cell doublet increases with increasing gap width. 3T3 fibroblast cells cultured on the CC-SD with the gap perpendicular to the direction of stretching.  $(\mathbf{A},\mathbf{B})$ , The deflection field of all pillars at 0% and 15% nominal substrate strain. The yellow frame represents the pillars considered for background analysis in  $(\mathbf{C})$ .  $(\mathbf{C})$ , Absolute deflections in x-and y-direction of pillars in a manual selected background region, i.e. excluding pillars covered by cells. In total, 98 and 154 pillars at 0% and 15% nominal strain, respectively, were considered.  $(\mathbf{D},\mathbf{E})$ , Deflection of pillars caused by cell traction forces at 0% and 15% nominal substrate strain. All deflections pointing towards the center of the cell are shown and were used for the analysis.  $(\mathbf{F})$ , Absolute deflections in x-and y-direction of pillars deflected by the cell. In total, 58 and 77 pillars at 0% and 15% nominal strain, respectively, were considered. Green: fibronectin-coated pillars, red: F-actin. Two-sided Wilcoxon rank sum test: \*  $p \leq 0.05$ , \*\*\*\* p < 0.0001, \*\* p > 0.05.

the background were  $0.0481 \pm 0.0022~\mu m$  and  $0.0965 \pm 0.0039~\mu m$  (mean  $\pm$  s.e.m.) at 0% and 15% nominal strain, respectively (Fig.3.5C). When the stress at the cell-cell contact increased, we expected a cellular response by increasing pillar deflections towards the gap to obey Newton's third law in terms of total force conservation. In order to check whether the strain at the cell-cell contact affected the overall applied traction forces, we analysed the pillar deflections below the cells (Fig.3.5D-E). At 0% strain, the mean deflection caused by the cells was found to be  $0.070 \pm 0.006~\mu m$  (mean  $\pm$  s.e.m.). When we applied the nominal substrate strain of 15%, the mean pillar deflections increased to  $0.137 \pm 0.009~\mu m$  (mean  $\pm$  s.e.m.) (Fig.3.5F). Since the mean pillar deflections,  $\langle \delta_{\rm all} \rangle$ , below the cells were close to the mean background deflections,  $\langle \delta_{\rm bkg} \rangle$ , we needed to correct for the background. Assuming that the real cellular deflections,  $\langle \delta_{\rm cell} \rangle$ , are uncorrelated to the background as given by the positional accuracy, the real

mean deflection is given by  $\langle \delta_{\rm cell} \rangle = \sqrt{\langle \delta_{\rm all} \rangle^2 - \langle \delta_{\rm bkg} \rangle^2}$  (Eq.(3.4), Eq.(3.5)). This value changed from  $\langle \delta_{\rm cell} \rangle = 0.050 \pm 0.008$  µm at 0% to  $\langle \delta_{\rm cell} \rangle = 0.098 \pm 0.013$  µm at 15% substrate strain. Unfortunately, the pillar height decreased towards the gap due to technical limitations in the manufacturing of the Si-wafer for the PDMS substrate. This challenge needs to be tackled to allow us to translate deflections into forces.

## 3.3 Discussion and conclusion

Our goal was to provide a design for intercellular force measurements of cells in substrate-attached and spread positions with fully developed actin stress fiber network. The novel design of structured force-sensor fields does allow us now to measure, in real-time, the cellular force response on controlled linear stress at the cell-cell contact of up to 140%, i.e. 2.4-fold. This large increase in gap width was sufficient to successfully break the cell-cell adhesions of MV3 cells (Fig.3.3G-H) and 3T3 fibroblasts (Fig.3.4A-B). Using homogeneous pillar arrays, we saw a deformation of the pillar array when the substrate strain was applied without affecting the mean traction forces of the cells (Fig.S3.7F). For each single cell and cell doublet, the law of conservation of forces must hold. All applied traction forces must sum to zero in mechanical equilibrium. Using the CC-SD by pulling the cells apart from each other and generating a stress at the cell-cell contact, thus we expected a change in the deflection field below the cells as long as they were still in contact (Fig.3.5F). The increased tension at the cell-cell contact would cause an increase in the magnitude of the total pillar deflections per doublet cell, assuming a constant number of deflected pillars for all applied substrate strains. Traction force exertion has been reported to be at least three minutes behind the intercellular signalling process (28). Our experiment was performed in a shorter duration of about two minutes. The pillar deflections caused by the cells on our CC-SD substrate were close to the background deflections and were affected by reduced accuracy in pillar detection when a strain was applied. Nevertheless, we recorded a tendency for an increase in the y-direction compared to the x-direction (Fig. 3.5F). This led us to speculate whether the cell responded to the increased strain. It has been reported that the applied traction forces of cells act parallel to the cell's elongation ((25); Chapter 2). In our presented example, the elongation of both 3T3 fibroblasts is indeed parallel to the gap, i.e. perpendicular to the direction of substrate stretching, and can therefore explain our result. Our novel design will open up possibilities for the analysis of intercellular force detachments in the future and sheds light on the robustness

of cell-cell adhesions in dynamic processes in the development of tissues.

### 3.4 Materials and methods

#### Cell culture

3T3 fibroblast and MV3 cells were cultured in high-glucose Dulbecco Modified Eagle's Medium (D6546; Sigma-Aldrich, St. Louis, MO, USA) supplemented with 10% fetal calf serum (Thermo Fisher Scientific, Waltham, MA, USA), 2 mM glutamine, and 100 mg/mL penicillin/streptomycin, 37 °C, 5%  $\rm CO_2$ .

#### **Immunostaining**

After 22.5 h of spreading, 3T3 fibroblast cells were fixed for 15 min in 4% paraformaldehyde (43368; Alfa Aesar, Haverhill, MA, USA) in phosphate-buffered saline (PBS). Furthermore, cells were permeabilized for 10 min with 0.1% Triton-X 100 in 1% bovine serum albumin (BSA) and blocked for 60 min with 1% BSA in PBS. F-actin was stained with Alexa Fluor 532-labeled phalloidin (A22282; Invitrogen, Carlsbad, CA, USA) and the DNA with DAPI (Sigma-Aldrich).

## Life-cell staining

2 h before imaging, F-actin of MV3 cells was stained with CellMask dye (A57245; Invitrogen, DeepRed Actin) and DNA with Hoechst 34580 (63493; Sigma-Aldrich).

#### Wafer manufacture of CC-SD substrate

The CC-SD substrate was manufactured in several dry etching steps (Fig. S3.8). In a first step, a silicon-wafer of 100 mm in diameter was oxidized by thermal oxidation (SiO<sub>2</sub> thickness: 430 nm). Afterwards, the first photolithography step took place, in which a thin layer of photoresist (PR; MEGAPOSIT SPR 955CM 0.7) was utilized to transfer the desire pattern and open the SiO<sub>2</sub> mask. In this step, the holes that will be the PDMS pillars later were defined. After opening the SiO<sub>2</sub> hard mask, the holes were transferred into the Si-substrate using the Bosch Process or gas chopping process to etch deep into the substrate. The remaining photoresist was removed and another SiO<sub>2</sub> hard mask created by thermal oxidation. Next, the second photoresist layer was applied by spraying. This layer was used to separate the hole arrays (block height, H) followed by opening the oxide mask by deep etching using the Bosch Process. Precise coordination of the etching depth of the two dry etching steps was essential, since this defines

the height of the pillars. This depth is strongly related to the diameter of the holes. In the final step, the remaining silicon oxide was removed by wet chemical etching (BOE).

#### Elastic micropillar arrays and CC-SD

Polydimethylsiloxane (PDMS, Sylgard 184) micropillar arrays of 2 μm diameter, 6.1  $\mu$ m ( $E_{\text{eff}} = 29.5 \text{ kPa}$ ) and 4.1  $\mu$ m length ( $E_{\text{eff}} = 47.2 \text{ kPa}$ ), and 4 µm spacing in a hexagonal geometry were used for cell traction force experiments. The pillar arrays were flanked by 50  $\mu$ m spacers on two sides of the array. Details of this arrangement and the experimental procedures were described earlier in detail (27). In brief, pillar arrays were produced on a negative silicon-wafer master made by a two-step deep reactive-ion etching process. Wafers were passivated in trichloro-silane (448931; Sigma-Aldrich). A mixture of 1:10 PDMS (cross-linker/base ratio) was poured onto the Si-master and cured for 20 h at 110 °C. CC-CD substrates were critical point dried. After peeling off, the tops of the pillars were coated by micro-contact printing. For that, flat 1:30 PDMS stamps were incubated for 1 h with 40 mL of 50 mg/mL Alexa Fluor 647-labeled or Alexa Fluor 532-labeled, and 50 mg/mL unlabeled fibronectin (F1141; Sigma-Aldrich), then washed and dried. Subsequently, the stamps were gently loaded onto the ultraviolet-ozone-activated micropillar arrays for 10 min. After stamping, the arrays were passivated with 0.2% Pluronic (F-127, P2443; Sigma-Aldrich) for 1 h, and washed in PBS.

#### Stretcher

We used an in-house made, piezo-driven stretcher (26). PDMS samples of 100  $\mu$ m thickness were mounted with two clamps (Fig.3.2A). A uniaxial stretch to the PDMS layer was applied by two independent piezo motors (SLC2430s, SmarAct) and a controller unit (MCS-3D, SmarAct, Oldenburg, Germany). An in-house written LabVIEW program was used to control the strain and strain rate. For our experiments, we took images ever 5% strain and increased the strain by a rate of 0.5 %/s.

#### Microscopy

Samples were imaged at high resolution on a home-build optical microscope setup based on an inverted Axiovert200 microscope body (Carl Zeiss, Oberkochen, Germany), a spinning disk unit (CSU-X1; Yokogawa Electric, Musashino, Tokyo, Japan), and an emCCD camera (iXon 897; Andor Labs, Morrisville, NC, USA). IQ-software (Andor Labs) was used for setup-control and data acquisition. Illumination was performed using fiber-

coupling of different lasers (405 nm (CrystaLaser, Reno, NV, USA), 514 nm (Cobolt AB, Solna, Sweden), and 642 nm (Spectra-Physics Excelsior; Spectra-Physics, Stahnsdorf, Germany)). 3T3 cells on pillar arrays for doublet analysis were placed upside down onto 25 mm cover glasses and inspected with an EC Plan-NEOFLUAR  $40\times1.3$  Oil Immersion Objective (Carl Zeiss). The stretcher unit for cell-cell separations was mounted on the microscope for inspections.

#### Scanning electron microscope

After cell fixation and washing steps with PBS buffer, the medium was gradually replaced by a mixture of ethanol and milliQ water: 50%, 70%, 80%, 90%, and 100%. Each incubation step was 10 min. Next, the sample was transferred in 100% ethanol into the chamber of the critical point dryer (CPD 020, Balzers). After the replacement of ethanol with liquid  $CO_2$ , the samples were dried. Before the investigation with the scanning electron microscope, samples were coated with lead/platinum.

#### Pillar stiffness characterization

The traction force to pillar deflection relation was calculated from Euler's theory for flexible beams, supplemented by correction terms (29). The total pillar deflection was described by bending, shear, and tilting deflection as

$$\delta = \delta_{\text{bend}} + \delta_{\text{shear}} + \delta_{\text{tilt}}, \tag{3.1a}$$

$$= \left(\frac{16}{3} \left(\frac{h}{d}\right)^3 + \frac{7 + 6\nu}{3} \frac{h}{d} + 8T_{\text{tilt}} \left(\frac{h}{d}\right)^2\right) \frac{4}{\pi E d} F_{\text{t}}, \tag{3.1b}$$

where  $F_{\rm t}$  is the traction force, E is the Young's modulus, d is the pillar diameter, h is the pillar length,  $\nu$  is the Poisson ratio, and

$$T_{\text{tilt}} = 1.3 \frac{1+\nu}{2\pi} \left( 2(1-\nu) + \left(1 - \frac{1}{4(1-\nu)}\right) \right).$$
 (3.2)

is the tilting coefficient (29). For our experiment,  $\nu=0.5$  and  $E=2{,}500$  kPa for PDMS. Accordingly, the traction force applied on the pillar was  $F_{\rm t}=k\delta$ .

The effective Young's modulus of the pillar field was calculated with (30)

$$E_{\text{eff}} = \frac{9k}{2\pi d}.\tag{3.3}$$

#### Image analysis

Images of MV3 and 3T3 cells within the field of view of  $176 \times 176~\mu m$  were analyzed using MATLAB scripts (MATLAB R2018a; MathWorks, Natick, MA, USA). Pillar deflections were quantified as previously described in detail (27). Deflected pillars caused by cell traction forces were distinguished from the background. The background was determined from an undeflected area of the pillar array by selecting a pillar region outside the cell area. Pillar deflections underneath the cell within the background range were excluded.

For cells in the CC-SD images, the mean of cellular deflections was calculated with

$$\langle \delta_{\text{cell}} \rangle = \sqrt{\langle \delta_{\text{all}} \rangle^2 - \langle \delta_{\text{bkg}} \rangle^2}.$$
 (3.4)

Here,  $\langle \delta_{\rm all} \rangle$  is the mean of all deflections below the cell and  $\langle \delta_{\rm bkg} \rangle$  is the mean deflection of the background. The error of  $\langle \delta_{\rm cell} \rangle$  was derived from the propagation of uncertainty

$$\sigma_{\langle \delta_{\text{cell}} \rangle} = \sqrt{\left(\frac{\partial \langle \delta_{\text{cell}} \rangle}{\partial \langle \delta_{\text{all}} \rangle} s_{\langle \delta_{\text{all}} \rangle}\right)^2 + \left(\frac{\partial \langle \delta_{\text{cell}} \rangle}{\partial \langle \delta_{\text{bkg}} \rangle} s_{\langle \delta_{\text{bkg}} \rangle}\right)^2},\tag{3.5}$$

with  $s_{\langle \delta_{\rm all} \rangle}$  and  $s_{\langle \delta_{\rm bkg} \rangle}$  the standard error of means.

#### Poisson correction

To determine the pillar deflections, we considered the x- and y- deformation of the substrate caused by the uniaxial stretch by using the Poisson ratio:

$$\frac{y - y_0}{y_0} = -\nu \frac{x - x_0}{x_0},\tag{3.6}$$

with  $x_0$ ,  $y_0$  the unstretched and x, y the stretched positions.

#### Intercellular force analysis

The intercellular force contribution of each cell in a doublet configuration was calculated with

$$F_{\text{cell},1} = \sum_{i=1}^{N} F_{t1,i}, \tag{3.7a}$$

$$F_{\text{cell},2} = \sum_{i=1}^{M} F_{t2,i}, \tag{3.7b}$$

where  $F_t$  is the traction force applied on one of N or M pillars. Considering Eqs.(3.7), the intercellular force results in

$$F_{\rm cc} = |F_{\rm cell,1}| + |F_{\rm cell,2}|.$$
 (3.8)

#### **Statistics**

P-values between two groups were calculated using the two-sided Wilcoxon rank sum test in MATLAB. Data sets were significantly different with probabilities of  $p \le 0.05$  (\*); p < 0.0001 (\*\*\*\*); p > 0.05 (ns).

#### Acknowledgements

J.E. acknowledges Erik Danen (Leiden University) for providing the MV3 cell line.

#### Author contributions

J.E. conducted and coordinated the research, performed analytic work, experiments, and data analysis. S.K., V.M. and S.P. manufactured the wafer for the CC-SD, J.E. and T.S. wrote the manuscript. T.S. supervised the project.

#### 3.5 Supplementary

#### **Table**

				<b>₽</b>	l l	_ thu		_ X _ I		
$\operatorname{Butterfly}$	1.4  to > 10	2.5	1235.7  to > 11.8	708.0  to  6.8	3.9	I	3.9	40	128	infinite
Tensile	2.5  to  5.4	2.7	504.1  to  82.5	267.4 to 43.8	3.7	55.6	4.1	35	108	infinite
Zig- $Zag$ 2	1.7  to  2.8	2.5	866.1 to 308.7	496.3 to 176.9	3.8	76.1	x: 4.8, y: 23.1	35	108	108
${ m Zig\text{-}Zag}$ 1	6.6  to  8.5	2.3	27.2  to  13.6	16.9 to 8.5	3.9	108.5	4.3	30	110	110
	height, $h$ ( $\mu$ m)	diameter, $d$ ( $\mu$ m)	stiffness, $k  (\text{nN/\mu m})$	$E_{ m eff}~({ m kPa})$	p-p distance, $r  (\mu m)$	deflection, $\delta$ (nm)	gap width, $R$ ( $\mu$ m)	height, $H$ ( $\mu$ m)	width, $W$ ( $\mu$ m)	length, $(\mu m)$
	ıslliq				рјоск					

Table S3.1: Cell-Cell Separation Device (CC-SD) specifications. This table summarizes all characteristics of the four different CC-SDs. The bending stiffness, k, was calculated with (3.1b) and the effective Young's modulus,  $E_{eff}$  with (3.3). All other values were obtained by analyzing SEM images using ImageJ and Matlab software. The substrates are made of PDMS with a Young's modulus of E = 2500 kPa.

# CHAPTER 3

#### Figures

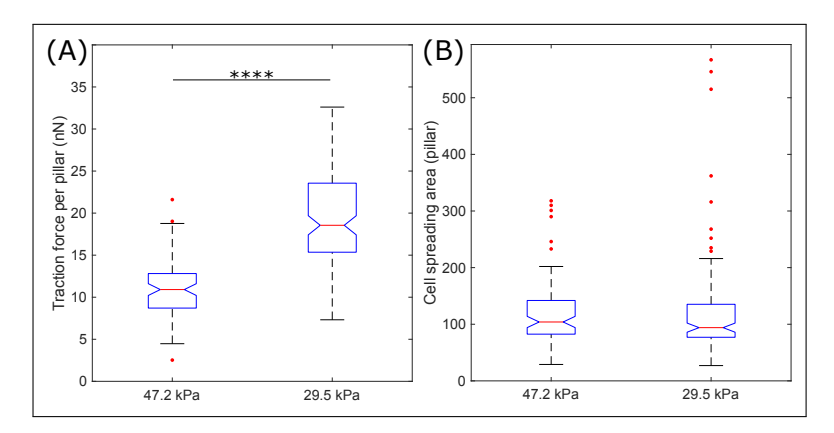


Figure S3.6: Single MV3 cells cultured on elastic micropillar arrays with Young's modulus of 47.2 kPa and 29.5 kPa ( $n_{stiff}$ =85,  $n_{soft}$ =128). (A), Cells apply larger traction forces on soft pillars compared to stiff. (B), The cell spreading areas are equal. Two-sided Wilcoxon rank sum test: \*\*\*\* p < 0.0001.

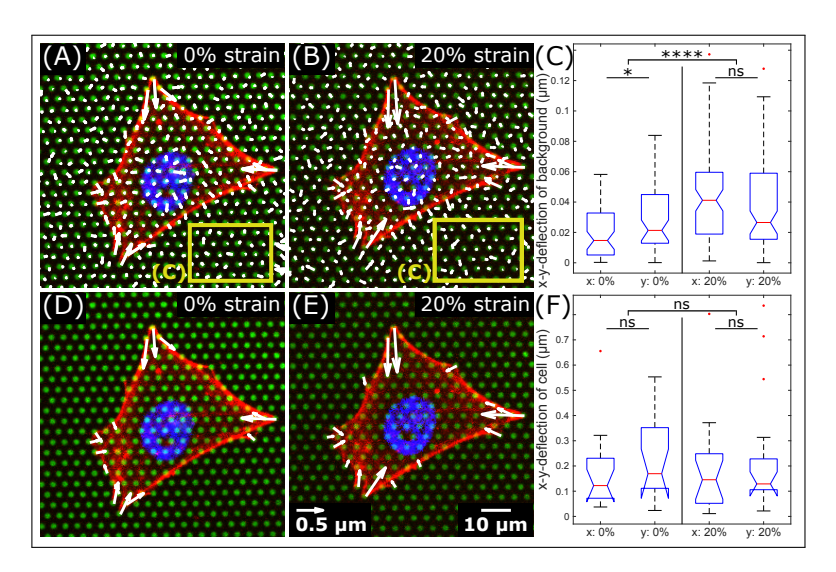


Figure S3.7: A single MV3 cell cultured on an elastic micropillar array with Young's modulus of 47.2 kPa. ( $\mathbf{A}$ , $\mathbf{B}$ ), The deflection field of all pillars at 0% and 20% nominal substrate strain. The yellow frame represents the pillars considered for background analysis in ( $\mathbf{C}$ ). ( $\mathbf{C}$ ), Absolute deflections in x-and y-direction of pillars in a manual selected background region, i.e. excluding pillars covered by cells. In total, 54 and 82 pillars at 0% and 20% nominal strain, respectively, were considered. ( $\mathbf{D}$ , $\mathbf{E}$ ), Deflection of pillars caused by cell traction forces at 0% and 20% nominal substrate strain. Only deflections towards the center of mass of the cell are shown. Background forces were excluded. ( $\mathbf{F}$ ), Absolute deflections in x-and y-direction of pillars deflected by the cell. In total, 15 and 16 pillars at 0% and 20% nominal strain, respectively, were considered. Green: fibronectin-coated micropillars, red:  $\mathbf{F}$ -actin, blue: nuclei. Two-sided Wilcoxon rank sum test: \*  $\mathbf{p} \leq 0.05$ , \*\*\*\*  $\mathbf{p} < 0.0001$ , \*\*  $\mathbf{p} > 0.05$ .

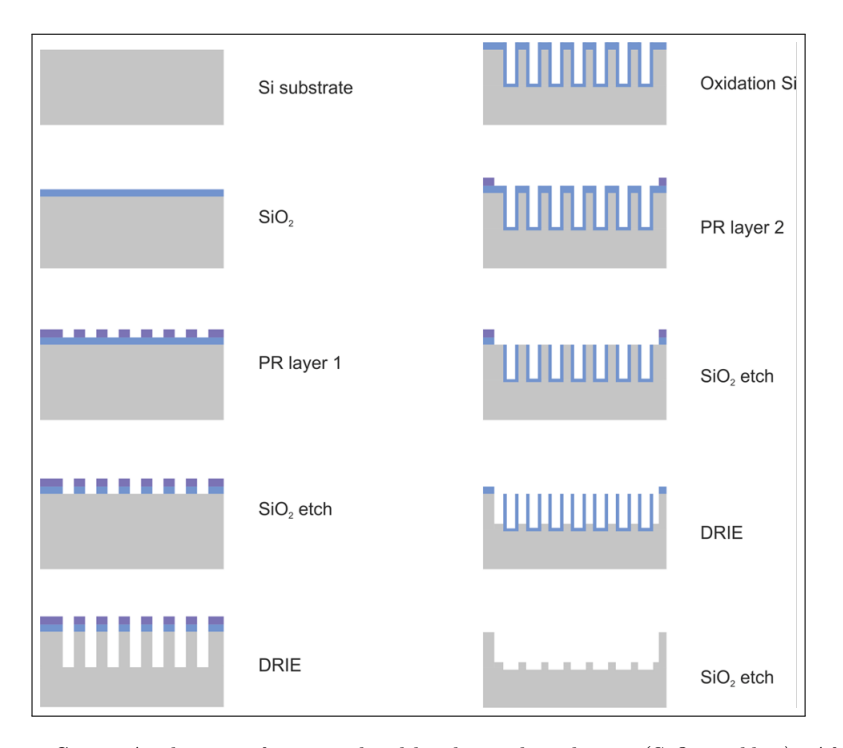


Figure S3.8: A silicon-wafer is oxidized by thermal oxidation (SiO<sub>2</sub> in blue). Afterwards, the first photolithography step takes place, in which a thin layer of photoresist (PR in purple) is utilized to transfer the desire pattern and open the SiO<sub>2</sub> mask. In this step, the holes that will be the PDMS pillars later are defined. After opening the SiO<sub>2</sub> hard mask, the holes are transferred into the Si-substrate using the Bosch Process or gas chopping process to etch deep into the substrate (DRIE). The remaining photoresist is removed and another SiO<sub>2</sub> hard mask (blue) created by thermal oxidation. Next, the second photoresist layer (purple) is applied by spraying. This layer is used to separate the hole arrays (block height H) followed by opening the oxide mask by deep etching using the Bosch Process. In the final step, the remaining silicon oxide is removed by wet chemical etching (BOE).

### References

- (1) Lehnert, D., Wehrle-Haller, B., David, C., Weiland, U., Ballestrem, C., Imhof, B. A., and Bastmeyer, M. (2004). Cell behaviour on micropatterned substrata: limits of extracellular matrix geometry for spreading and adhesion. *Journal of Cell Science* 117, 41–52.
- (2) Reinhart-King, C. A., Dembo, M., and Hammer, D. A. (2008). Cell-cell mechanical communication through compliant substrates. *Biophysical journal 95*, 6044–6051.
- (3) Yap, A. S., Duszyc, K., and Viasnoff, V. (2018). Mechanosensing and Mechanotransduction at Cell-Cell Junctions. Cold Spring Harbor Laboratory Press 10, a028761.
- (4) Arslan, F. N., Eckert, J., Schmidt, T., and Heisenberg, C.-P. (2021). Holding it together: when cadherin meets cadherin. *Biophysical Journal* 120, 4182–4192.
- (5) Charras, G., and Yap, A. S. (2018). Tensile Forces and Mechanotransduction at Cell–Cell Junctions. *Current Biology* 28, R445–R457.
- (6) Kashef, J., and Franz, C. M. (2015). Quantitative methods for analyzing cell–cell adhesion in development. *Developmental Biology* 401, 165–174.
- (7) Polacheck, W. J., and Chen, C. S. (2016). Measuring cell-generated forces: a guide to the available tools. *Nature Methods* 13, 415–423.
- (8) Campàs, O. (2016). A toolbox to explore the mechanics of living embryonic tissues. Seminars in cell & developmental biology 55, 119–130.
- (9) Sugimura, K., Lenne, P.-F., and Graner, F. (2016). Measuring forces and stresses in situ in living tissues. Development 143, 186–196.
- (10) Rehfeldt, F., and Schmidt, C. F. (2017). Physical probing of cells. *Journal of Physics D: Applied Physics* 50, 463001.
- (11) Roca-Cusachs, P., Conte, V., and Trepat, X. (2017). Quantifying forces in cell biology. Nature Cell Biology 19, 742–751.
- (12) Basoli, F., Giannitelli, S. M., Gori, M., Mozetic, P., Bonfanti, A., Trombetta, M., and Rainer, A. (2018). Biomechanical Characterization at the Cell Scale: Present and Prospects. Frontiers in Physiology 9, 1449.
- (13) Gómez-González, M., Latorre, E., Arroyo, M., and Trepat, X. (2020). Measuring mechanical stress in living tissues. *Nature Reviews Physics* 2, 300–317.
- (14) Benoit, M., Gabriel, D., Gerisch, G., and Gaub, H. E. (2000). Discrete interactions in cell adhesion measured by single-molecule force spectroscopy. *Nature Cell Biology* 2, 313–317.

72 References

(15) Puech, P.-H., Taubenberger, A., Ulrich, F., Krieg, M., Muller, D. J., and Heisenberg, C.-P. (2005). Measuring cell adhesion forces of primary gastrulating cells from zebrafish using atomic force microscopy. *Journal of Cell Science* 118, 4199–4206.

- (16) Sung, K., Sung, L., Crimmins, M., Burakoff, S., and Chien, S. (1986). Determination of junction avidity of cytolytic T cell and target cell. Science 234, 1405–1408.
- (17) González-Bermúdez, B., Guinea, G. V., and Plaza, G. R. (2019). Advances in Micropipette Aspiration: Applications in Cell Biomechanics, Models, and Extended Studies. *Biophysical Journal* 116, 587–594.
- (18) Zhao, B., Li, N., Xie, T., Bagheri, Y., Liang, C., Keshri, P., Sun, Y., and You, M. (2020). Quantifying tensile forces at cell-cell junctions with a DNA-based fluorescent probe. Chemical Science 11, 8558–8566.
- (19) Liu, Z., Tan, J. L., Cohen, D. M., Yang, M. T., Sniadecki, N. J., Ruiz, S. A., Nelson, C. M., and Chen, C. S. (2010). Mechanical tugging force regulates the size of cell-cell junctions. Proceedings of the National Academy of Sciences of the United States of America 107, 9944–9949.
- (20) Maruthamuthu, V., Sabass, B., Schwarz, U. S., and Gardel, M. L. (2011). Cell-ECM traction force modulates endogenous tension at cell-cell contacts. Proceedings of the National Academy of Sciences 108, 4708–4713.
- (21) McCain, M. L., Lee, H., Aratyn-Schaus, Y., Kléber, A. G., and Parker, K. K. (2012). Cooperative coupling of cell-matrix and cell-cell adhesions in cardiac muscle. Proceedings of the National Academy of Sciences 109, 9881–9886.
- (22) Mertz, A. F., Che, Y., Banerjee, S., Goldstein, J. M., Rosowski, K. A., Revilla, S. F., Niessen, C. M., Marchetti, M. C., Dufresne, E. R., and Horsley, V. (2013). Cadherin-based intercellular adhesions organize epithelial cell-matrix traction forces. Proceedings of the National Academy of Sciences 110, 842–847.
- (23) Ng, M. R., Besser, A., Brugge, J. S., and Danuser, G. (2014). Mapping the dynamics of force transduction at cell–cell junctions of epithelial clusters. *eLife* 3, e03282.
- (24) Eckert, J., van Loon, J. J. A., Eng, L. M., and Schmidt, T. (2021). Hypergravity affects cell traction forces of fibroblasts. *Biophysical Journal* 120, 773–780.
- (25) Eckert, J., Abouleila, Y., Schmidt, T., and Mashaghi, A. (2021). Single Cell Micro-Pillar-Based Characterization of Endothelial and Fibroblast Cell Mechanics. *Micro* 1, 242–249.
- (26) Balcioglu, H. E., van Hoorn, H., Donato, D. M., Schmidt, T., and Danen, E. H. J. (2015). The integrin expression profile modulates orientation and dynamics of force transmission at cell–matrix adhesions. *Journal of Cell Science* 128, 1316– 1326.
- (27) van Hoorn, H., Harkes, R., Spiesz, E. M., Storm, C., van Noort, D., Ladoux, B., and Schmidt, T. (2014). The Nanoscale Architecture of Force-Bearing Focal Adhesions. Nano Letters 14, 4257–4262.
- (28) van Hoorn, H., Donato, D. M., Balcioglu, H. E., Danen, E. H., and Schmidt, T. (2018). p130Cas contributes to cellular mechanosensing and force exertion. bioRxiv.

References 73

(29) Schoen, I., Hu, W., Klotzsch, E., and Vogel, V. (2010). Probing Cellular Traction Forces by Micropillar Arrays: Contribution of Substrate Warping to Pillar Deflection. *Nano Letters* 10, 1823–1830.

(30) Ghibaudo, M., Saez, A., Trichet, L., Xayaphoummine, A., Browaeys, J., Silberzan, P., Buguin, A., and Ladoux, B. (2008). Traction forces and rigidity sensing regulate cell functions. *Soft Matter 4*, 1836–1843.

### Epithelia are multiscale active liquid crystals

Biological processes, such as embryogenesis, wound healing and cancer progression, crucially rely on the ability of epithelial cells to coordinate their mechanical activity over length scales larger than the typical cellular size. While regulated by various signaling pathways, it has recently become evident that this behavior can additionally hinge on a minimal toolkit of physical mechanisms, of which liquid crystal order is the most prominent example. Yet, experimental and theoretical studies have given so far inconsistent results in this respect: whereas nematic order is often invoked in the interpretation of experimental data, computational models have instead suggested that hexatic order could in fact serve as a linchpin for collective migration in confluent cell layers. In this article, we resolve this dilemma. Using a combination of *in vitro* experiments on Madin-Darby canine kidney cells (MDCK), numerical simulations and analytical work, we demonstrate that both nematic and hexatic order are in fact present in epithelial layers, with the former being dominant at large length scales and the latter at small length scales. In MDCK GII cells on uncoated glass, these different types of liquid crystal order crossover at 34 µm, corresponding approximately to clusters of 21 cells. Our work sheds light on the emergent organization of living matter, provides a new framework for deciphering the emergent organization of epithelia and paves the way toward a comprehensive and predictive mesoscopic theory of tissues.

This chapter is based on: Armengol-Collado, J.-M., Carenza, L. N., **Eckert, J.**, Krommydas, D., and Giomi, L. (2022). Epithelia are multiscale active liquid crystals. arXiv:2202.00668, under revision.

## CHAPTER 4

#### 4.1 Introduction and results

An increasingly large body of evidence suggests that liquid crystal order could lie at the heart of a myriad of cellular processes that are instrumental for life (1-7). These include the extrusion of apoptotic cells (2), the development of sharp morphological features in developing embryos (8, 9) or the onset of organism-wide cellular flows during morphogenesis (10). In confluent epithelial layers, detecting liquid crystal order is commonly achieved by tracking the longitudinal direction of individual cells by diagonalizing a rank-2 tensor – i.e. the so-called structure tensor (11) or equivalently the shape tensor (12, 13) in case of segmented images – that embodies the geometry of the polygonal cells (Fig.4.1A). The resulting two-dimensional orientation field is then used to identify topological defects (1-4), which in turn provide a fingerprint of the underlying orientational order. Liquid crystal defects (also known as disclinations) are isolated singularities in the orientational field and can be classified according to their winding number or 'strength', s, defined as the number of revolutions of the orientation field along an arbitrary contour encircling the defect core (14). Because in a two-dimensional liquid crystal with p-fold rotational symmetry (i.e. symmetry under rotations by  $2\pi/p$ ) this number must be an integer multiple of 1/p, defects such as vortices, asters and spirals, for which s=1, are a signature of a polar phase (i.e. p=1); comet- and star-shaped disclinations, whose winding numbers are s = 1/2 and s = -1/2 respectively, are representative of a nematic phase (i.e. p=2); whereas 5-fold and 7-fold disclinations, with s = 1/6 and s = -1/6, are the elementary topological defects in hexatics (i.e. p = 6).

Although inferring order from defects represents a consolidated strategy in liquid crystals science since the times of Georges Friedel (15) — who used it to decipher and classify phases such as nematic, cholesteric, and smectic — this specific protocol, based on tracking the cells' longitudinal direction, becomes progressively less reliable as p increases. To illustrate this issue, we show in Fig.4.1B how applying the same protocol to a perfect honeycomb lattice can lead to the misdetection of a pair of  $\pm 1/2$  nematic disclinations. This originates from the fact that, while regular hexagons are invariant under rotations by 60°, the orientation field constructed from the longitudinal direction of hexagonal cells cannot discriminate between the three equivalent directions defined by pairs of opposite vertices. Similarly, in Fig.4.1C and Fig.4.1D we show how detecting an elementary hexatic disclination correctly yields a topological defect, but with incorrect winding number s=1.

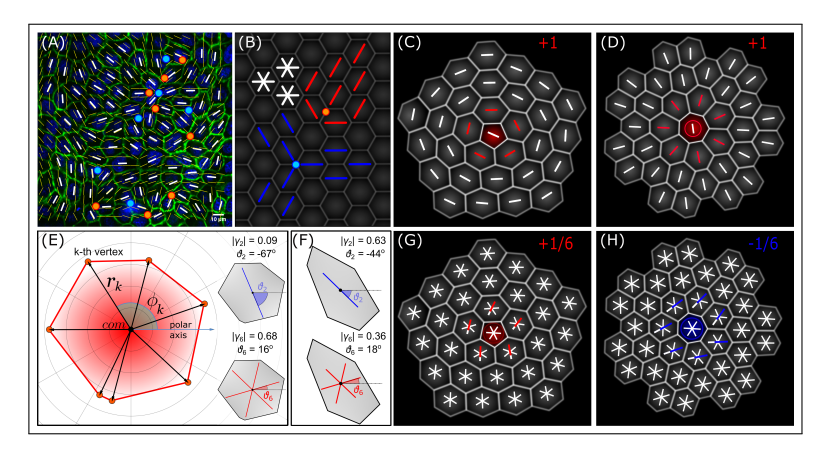


Figure 4.1: Topological defects and p-fold rotational symmetry. (A), A typical configuration of the nematic orientation field (white rods), obtained from a sample of MDCK GII cells upon diagonalizing the shape tensor (12, 13). Yellow rods represent the interpolated nematic field. Here and in the following, positive and negative defects are marked in red and blue, respectively, regardless of the magnitude of their winding number. (B), Because of the 6-fold symmetry of regular hexagons, there is no well-defined longitudinal direction, thus it is possible to construct a defective configuration, featuring a pair of  $\pm 1/2$  disclinations, even though the lattice is defect free. (C,D), Disclinations in hexatics consist of pentagonal (i.e. s=1/6) and heptagonal (i.e. s = -1/6) sites embedded in an otherwise 6-fold background. Attempting to detect these elementary defects by tracking the longitudinal direction of the cells (with rods), correctly yields a defect at the center of the clusters, however, because of the mismatch between the 6-fold symmetry of the configuration and the 2-fold symmetry of the order parameter both defects are detected with the incorrect winding number s=1. (E), Graphical representation of the p-fold order parameter, Eq.(4.2), for a generic polygon (heptagon). The quantities  $\mathbf{r}_k = \{x_k, y_k\}$  and  $\phi_k = \arctan(y_k/x_k)$ represent, respectively, the position of the vertices of the polygon with respect to its center of mass (i.e. com) and their orientation with respect to the horizontal direction (i.e. polar axis). The inset shows the nematic (top) and hexatic (bottom) order parameter,  $\gamma_p$ , superimposed on the polygonal shape of the main panel. (F), Example of the  $\gamma_p$  order parameter, Eq.(4.2), for an elongated hexagon. The irregular heptagon in panel (E) is closer in shape to a regular hexagon, thus the order parameter  $\gamma_6$  is an order of magnitude larger than  $\gamma_2$ . The outcome is reversed in the irregular hexagon in panel (F), which, as a consequence of its elongation and despite being 6-sided, yields  $\gamma_2 > \gamma_6$ . In both panels, the blue rods and the 6-legged stars correspond respectively to the 2-fold and 6-fold orientations of the polygons and are oriented in such a way that maximizes the overall probability of finding a vertex in the direction of the legs. (H,I), The correct recognition of the hexatic disclinations are shown in panels (C) and (D) using  $\gamma_6$ . In both panels, one of the legs of the order parameter has been colored as a guide to the eye. By following the order parameter along a positive oriented (anticlockwise) close loop encircling the defect core, the red leg rotates anticlockwise for the positive defect in panel (E). After a full rotation, the colored leg rotates of an angle  $2\pi/6$  corresponding to a winding number s=1/6. Conversely, in panel (I) the blue leg rotates clockwise and covers an angular displacement of  $-\pi/3$ corresponding to a winding number s = -1/6.

To overcome this difficulty, here we introduce a generalized rank-p shape tensor, able to capture arbitrary p-fold rotational symmetries, with p any natural number. Given the polygonal contour of a cell, whose V vertices have coordinates  $\mathbf{r}_k = \{x_k, y_k\}$  with respect to the cell's center of mass (Fig.4.1E), our generalized shape tensor can be defined as

$$G_p = \frac{1}{\Delta_p} \left[ \sum_{k=1}^{V} \underbrace{\mathbf{r}_k \otimes \mathbf{r}_k \otimes \cdots \otimes \mathbf{r}_k}_{p \text{ times}} \right], \tag{4.1}$$

where  $\Delta_p = \sum_{k=1}^V |r_k|^p$ , and the operator  $[\![\cdot\cdot\cdot]\!]$  has the effect of rendering its argument symmetric and traceless. For tensors whose rank is higher than two, the property of being traceless implies that contracting any two indices of the tensor yields zero. For p=2, Eq.(4.1) gives, up to a normalization constant, the traceless part of the standard rank-2 shape tensor (12, 13). Regardless of its rank, the tensor  $G_p$  has only two linearly independent components in two dimensions (16, 17), from which one can extract information about the cells' orientation and anisotropy. In particular, using a generalization of the spectral theorem to tensors with arbitrary rank (18), one can show that all elements of  $G_p$  are proportional to either the real or the imaginary part of the complex order parameter

$$\gamma_p = \frac{1}{\Delta_p} \sum_{k=1}^{V} |\mathbf{r}_k|^p e^{ip\phi_k} = |\gamma_p| e^{ip\vartheta_p}, \tag{4.2}$$

where  $\phi_k = \arctan(y_k/x_k)$  the angular coordinate of the k-th vertex of a given cell (Fig.4.1E). The angle  $\vartheta_p$ , on the other hand, corresponds to the p-fold orientation of the whole cell with respect to the horizontal direction. In practice, this is equivalent to the inclination of a p-legged star centered at the cell's center of mass and oriented in such a way to maximize the probability of finding a vertex in the direction of either one of the legs. Some examples of this construction are shown in Fig.4.1E and Fig.4.1F, where  $\gamma_p$  is computed for more or less elongated irregular polygons. When applied to defective configurations, our method yields the correct winding numbers  $s = \pm 1/6$  (Fig.4.1G and Fig.4.1H).

With the tensor  $G_p$  in hand, we next investigate the emergent orientational order in confluent monolayers of MDCK GII cells (Fig.4.2A and Fig.4.2B). After segmenting the images by taking advantage of the previous labeling of E-cadherin, we track the cells' contour and from the coordinates of the vertices we compute the order parameter  $\gamma_p$ , Eq.(4.2). We analyze a total of 68 images of confluent monolayers (see the Methods for details) with each one of them comprising  $140 \pm 31$  cells (mean  $\pm$  s.d.). Fig.4.2C

shows the probability distribution of  $\gamma_p$  for p=2 and p=6. Interestingly, the distribution of  $\gamma_6$  is symmetric and spreads over a broad range of values; conversely, the distribution of  $\gamma_2$  features a peak at approximately 0.35, with a decreasing tail at larger values. The MDCK GII cells analyzed in this study are, therefore, more prone to arrange in isotropic rather than elongated shapes.

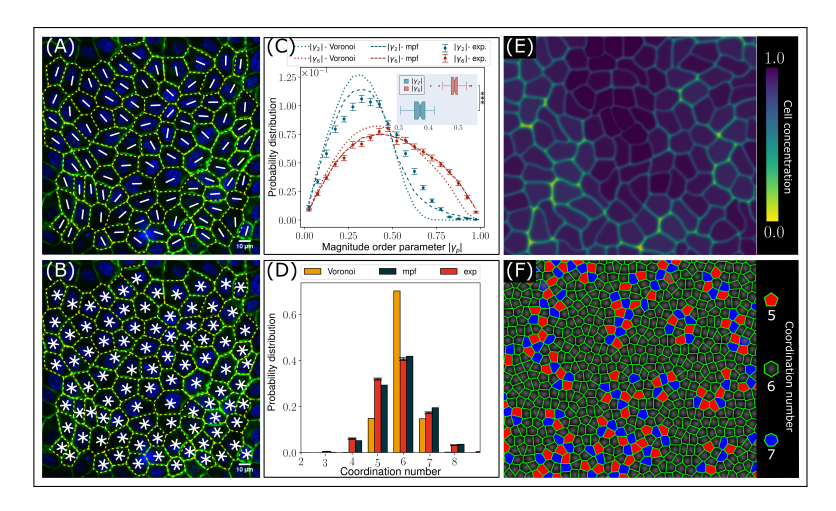


Figure 4.2: Symmetry of MDCK cells in confluent monolayers. (A.B). Confocal image of a confluent MDCK GII monolayer (green, E-cadherin and blue, nuclei). The dashed yellow lines trace the contour of the cells as identified after image segmentation. The white rods (A) and stars (B) respectively mark the 2-fold and 6-fold orientation of cells and have been obtained from the order parameter  $\gamma_p$ , Eq.(4.2). (C), Probability distribution of the magnitude of the order parameter  $|\gamma_p|$  for p=2(blue) and p = 6 (red). Experimental data points are obtained by averaging over 68 different images, with each containing  $140 \pm 31$  (mean  $\pm$  s.d.) cells. The mean value of the distributions are  $\langle |\gamma_2| \rangle = 0.370 \pm 0.030$  (mean  $\pm$  s.d.) and  $\langle |\gamma_6| \rangle = 0.49 \pm$  $0.05~(mean~\pm~s.d.)$ . The boxplot in the inset shows the average magnitudes of the order parameters of 68 imaged monolayers.  $\langle |\gamma_2| \rangle$  and  $\langle |\gamma_6| \rangle$  are significantly different with a p-value < 0.0001, calculated by using the two-sided Wilcoxon rank sum test. Dashed and dotted lines are obtained from numerical simulations of the multiphasefield (mpf) and Voronoi models. (D), Probability distribution of cell coordination number for experiments and simulations. The height of the bar represents the mean of 68 analyzed images. The mean values of the coordination number distributions are  $5.8 \pm 0.9 \; (mean \pm s.d.) \; for \; experiments, \; 5.9 \pm 0.9 \; (mean \pm s.d.) \; for \; multiphase$ field simulations, and  $6.0 \pm 0.6$  (mean  $\pm$  s.d.) for Voronoi simulations. In (C) and (D), error bars are computed from the standard error of mean. (E), Contour plot of the local cell concentration of a multiphase-field simulation with 360 cells in a magnified region of the simulation box, showing approximately one third of the system. Darker regions correspond to areas dense with cells and lighter regions to areas where cells are sparser (see legend box). (F), Configuration of a numerical simulation of the Voronoi model. The cells in red (blue) have 5 (7) neighbors, while others have 6.

This results in a disordered and yet orientationally coherent tiling of the plane, where a majority of hexagons coexists with large minorities of pentagons and heptagons, as indicated by the distribution of the number of neighbors in Fig.4.2D. We compare these observations with numerical simulations of two different theoretical models of epithelia: i.e. a continuous multiphase field model (mpf) (Fig.4.2E; (19-21)) and the discrete Voronoi model (Fig.4.2F; (22)), both in qualitative agreement with experimental data.

In order to quantify the amount of orientational order in the system, we next compare the orientation of each cell with that of its neighbors, by means of the following coarse-graining procedure. Given a disk  $\Omega_R = \Omega_R(\mathbf{r})$ , with radius R and centered at  $\mathbf{r}$ , and letting  $\mathbf{r}_c$  be the position of the center of mass of the c-th cell, we define the coarse-grained order field  $\Gamma_p = \Gamma_p(\mathbf{r})$  as

$$\Gamma_p = \frac{1}{N} \sum_{c=1}^{N} \gamma_p(\mathbf{r}_c) = |\Gamma_p| e^{ip\theta_p}, \tag{4.3}$$

where N is the number of cells whose center of mass lies within  $\Omega_R$ , while  $|\Gamma_p| = |\Gamma_p(\mathbf{r})|$  and  $\theta_p = \theta_p(\mathbf{r})$  are respectively the magnitude and phase of the complex order parameter  $\Gamma_p$ , conveying information about the amount and direction of p-fold orientational order at the length scale R (Fig.4.3A).

The outcome of this analysis is shown in Fig.4.3B and Fig.4.3C. At length scales comparable with the average cell size - i.e.  $R \lesssim R_{\text{cell}}$ , with  $R_{\text{cell}} = 7.4 \pm 1.9 \,\mu\text{m}$  the average cell radius computed as half of the distance between the cells' centers of mass - both the nematic (Fig.4.3B) and the hexatic (Fig.4.3C) coarse-grained fields are populated by topological defects. For p = 6, in particular, the monolayer appears organized into regions characterized by spatially uniform hexatic order, separated by arrays of  $\pm 1/6$  disclinations, similarly to grains and grain boundaries in polycrystals (23). Increasing R has the effect of smoothing the  $\Gamma_6$  field, thereby absorbing neutral pairs of disclinations into a gently varying 6-fold orientation field, resulting in a power law decreasing defect density (Fig.4.3D).

The scenario differs dramatically for p=2 (Fig.4.3B). In this case, many of the defective structures identified in the configuration of the hexatic field at the small length scales are replaced by very sharp and yet defect-free textures. This peculiarity originates precisely from the mismatch between the actual 6-fold symmetry of the configuration at the cellular scale and the 2-fold symmetry of the order parameter used to describe it, in a similar fashion as using a (polar) vector field to describe a nematic disclination gives rise to singular lines where the polar field 'jumps' by an angle  $\pi$  (Fig.4.3E).

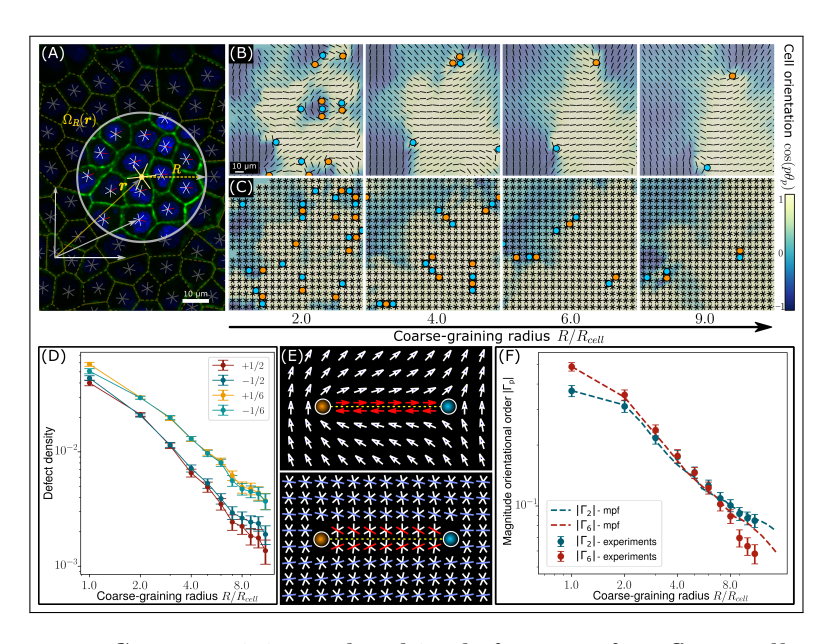


Figure 4.3: Coarse-graining and multiscale features of confluent cell monolayers. (A), Illustration of the coarse-graining procedure entailed in Eq. (4.3). A disk  $\Omega_R = \Omega_R(\mathbf{r})$  (encircled in gray), with radius R and centered at the point  $\mathbf{r}$  (in general not coincident with the center of mass of any specific cell) is superimposed to a segmented image of the cell monolayer and the cells in its interior are used to compute the coarse-grained filed  $\Gamma_p$ . The large yellow star at the center of the disk shows the orientation of the whole cluster. (B,C), Nematic (top row) and hexatic (bottom row) coarse-grained fields  $\Gamma_2$  and  $\Gamma_6$  versus the coarse-graining radius R, expressed in units of the average cell size  $R_{cell} = 7.4 \,\mu m$ . In both panels, positive and negative defects are marked in red and blue, respectively  $(\pm 1/2 \text{ for nematic and } \pm 1/6$ for hexatic). (D), Defect density at varying the coarse-graining radius R. (E), A mismatch between the defect charge and the symmetry of the p-atic liquid crystal gives rise to unphysical singular line (see Sec. S4.4.2). Top (bottom) panel shows a pair of nematic (hexatic) defects of winding number  $s = \pm 1/2$  ( $s = \pm 1/6$ ). (F), Magnitude of  $\Gamma_2$  and  $\Gamma_6$  versus the coarse-graining radius R measured from experimental and numerical mpf data. Both data sets fit the power law  $|\Gamma_p| = \langle \gamma_p \rangle (R/R_{cell})^{-\eta_p/2}$ , with  $\eta_p$  a non-universal exponent (16, 17), with the following fitting parameters: (experiments)  $\eta_2 = 0.41 \pm 0.01$ ,  $\eta_6 = 0.49 \pm 0.01$ ; (mpf)  $\eta_2 = 0.43 \pm 0.02$ ,  $\eta_6 = 0.48 \pm 0.01$ . In both experiments and multiphase field simulations, the  $|\Gamma_2|$  and  $|\Gamma_6|$  order parameters crossover at the length scale  $R_{\times}$ , with: (experiment)  $R_{\times}/R_{\rm cell} = 4.6 \pm 1.0$ ; (mpf)  $R_{\times}/R_{cell} = 5.0 \pm 1.2$ . In (D) and (F), the error bars correspond to the standard error of the mean.

Conversely, at larger length scales, the majority of nematic defects is replaced by regions where the nematic field  $\Gamma_2$  smoothly varies across the sample, with exception for a small number of isolated  $\pm 1/2$  disclinations (Fig.4.3B and Fig.4.3D). These observations are further supported by the scaling behavior of the magnitude of the fields  $\Gamma_2$  and  $\Gamma_6$  as the coarse-

graining radius R varies (Fig.4.3F). In particular, both  $|\Gamma_2|$  and  $|\Gamma_6|$  are finite at all length scales in the range  $1 \leq R/R_{\rm cell} < 10$ , but, while  $|\Gamma_6|$  is prominent at small length scales, this is overweighted by  $|\Gamma_2|$  at large length scales. For our MDCK GII cells on uncoated glass, the crossover occurs at  $R_{\times}/R_{\rm cell} = 4.6 \pm 1.0$ , corresponding to clusters of approximately 21 cells. The same crossover is also observed in our numerical simulations of the multiphase field model, with the crossover scale  $R_{\times}/R_{\rm cell} = 5.0 \pm 1.2$ , while it is not found in simulations of the Voronoi model, where hexatic order is dominant at all length scales.

Taken together, our experimental and numerical results demonstrate that epithelial monolayers behave as multiscale active liquid crystals, with 6—fold hexatic order characterizing the spatial organization of the cells at small length scales, while nematic order dictates the large-scale structure of the monolayer. The crossover length scale is, as intuitive, non-universal, but depends on the molecular repertoire and the material properties of the specific phenotype, as well as on the mechanical properties and the surface chemistry of the substrate.

#### 4.2 Discussion and conclusion

In conclusion, we have investigated the multiscale physics of epithelial layers, finding that multiple types of liquid crystal order can coexist at different length scales. In particular, hexatic order is prominent at the cellular scale (i.e. in clusters of up to 21 cells in our MDCK GII samples) while nematic order characterizes the structure of the monolayer at larger length scales. This hierarchical structure is expected to complement the complex network of regulatory pathways that tissues have at their disposal (24) to coordinate the activity of individual cells to achieve multicellular organization (25). The novel approach introduced here creates the basis for a correct identification of topological defects – whose biophysical role in epithelia has recently focused great attention (1-3), especially in the context of morphogenesis (8, 10, 26, 27) – and further provides the necessary knowledge for the foundation of a comprehensive and predictive mesoscopic theory of collective cell migration (28). In addition, our findings highlight a number of potentially crucial properties of epithelial tissues. First, collective cell migration in epithelia relies on both remodeling events at the small scale – such as cell intercalation and the rearrangement of multicellular rosettes (29, 30) – as well as large scale flows (10). Therefore, the underlying hexanematic multiscale organization and the specific magnitude of the crossover scale  $R_{\times}$  are expected to have a profound impact on how

the geometry of the environment affects the specific migration strategy. E.g. metastatic cells traveling through micron-sized channels in the extracellular matrix during cancer invasion (31) will more likely rely on local hexatic-controlled remodeling events, whereas unconfined wound healing processes (32) are more likely to leverage on system-wide nematic-driven collective flows. Second, as both hexatic and nematic liquid crystals can feature topological defects, these are expected to interact, thereby affecting processes such as the extrusion of apoptotic cells (2), the development of sharp features during morphogenesis (8, 9) and, in general, any remodeling or morphogenetic event that can take advantage of the persistent pressure variations introduced by active defects (3). Finally, in the light of what said above, it is evident that understanding how the crossover scale  $R_{\times}$  can be controlled, either chemically or mechanically, may ultimately represent the key toward deciphering tissues' collective dynamics.

#### 4.3 Materials and methods

#### Cell culture

Parental Madin-Darby Canine Kidney (MDCK) GII cells stably expressing E-cadherin-GFP (33) (kindly provided by M. Gloerich, UMC Utrecht) were cultured in a 1:1 ratio of low glucose DMEM (D6046; Sigma-Aldrich, St. Louis, MO) and Nutrient Mixture F-12 Ham (N4888; Sigma-Aldrich, St. Louis, MO) supplemented with 10% fetal calf serum (Thermo Fisher Scientific, Waltham, MA), and 100 mg/mL penicillin/streptomycin, 37 °C, 5% CO<sub>2</sub>. For experiments, cells were seeded on uncoated cover glasses, grew to confluence, and nuclei were live-stained with 2 μg/mL Hoechst 34580 (Thermo Fisher, H21486) before imaging.

#### Microscopy

Samples were imaged at high resolution on a home-build optical microscope setup based on an inverted Axiovert200 microscope body (Zeiss), a spinning disk unit (CSU-X1, Yokogawa), and an emCCD camera (iXon 897, Andor). IQ-software (Andor) was used for setup-control and data acquisition. Illumination was performed using fiber-coupling of different lasers (405 nm (CrystalLaser) and 488 nm (Coherent)). Cells on over glasses were inspected with an EC Plan-NEOFLUAR  $40\times1.3$  Oil immersion objective (Zeiss). Images were taken in three focal-planes within a distance of 352 nm for a maximal intensity projection.

#### **Analysis**

Shape order parameter. Cell boundaries of confluent monolayers were analyzed using a maximum intensity projection of z-stack images. Cell segmentation and vertex analysis were performed using home-build Matlab scripts (Mathworks, Matlab R2018a). The number of nearest neighbors corresponds to the number of vertices surrounding a cell. The centroid of the polygon was calculated by  $\mathbf{r}_c = \sum_{i=1}^V \mathbf{r}_i/V$ , where V is the number of vertices and  $\mathbf{r}_i$  their positions. For each cell, the shape order was derived by using Eq.(4.2). On average, we analyzed 140  $\pm$  31 cells per image. For the probability distribution of the shape order for each analyzed image, we choose a binning of 20 ranging from 0 to 1.

Coarse-graining. The radius used to construct the coarse-grained field, given by Eq.(4.3), was chosen according to the typical cell radius  $R_{\rm cell} = 7.4 \pm 1.9 \, \mu \rm m$ , calculated as half of the average cell-cell nearest neighbor distance. For calculating the crossover point, we set the center point of the disk equal to the center point of the image. The radius of the disk in which the complex order parameters were averaged ranged from  $R_{\rm cell}$  to half of the image size (176  $\times$  176  $\mu \rm m$ ). For computing the nematic and hexatic coarse-grained director field, we set the grid-distance to  $R_{\rm cell}$ .

Topological defects. Topological defects were identified by first interpolating the p-fold orientation field on a square  $22 \times 22$  grid by means of the coarse-graining procedure in Eq.(4.3) and then computing the winding number along each unit cell. That is:

$$s = \frac{1}{2\pi} \oint_{\square} d\theta_p = \frac{1}{2\pi} \sum_{n=1}^{4} \left[ \theta_p(\mathbf{r}_{n+1}) - \theta_p(\mathbf{r}_n) \right] \mod \frac{2\pi}{p}, \tag{4.4}$$

where the symbol  $\square$  denotes a square unit cell in the interpolation grid and the mod operator constraints the difference  $\theta_p(\mathbf{r}_{n+1}) - \theta_p(\mathbf{r}_n)$  in the interval  $[-\pi/p, \pi/p]$ .

#### Statistics

In total, 68 images of confluent monolayers (nine coverslips, three independent experiments) were taken and analyzed. In total, 9496 cells were considered for the analysis.

#### Numerical simulations

We make use of two different numerical models for ET previously introduced in literature: (i) the multiphase field model and (ii) the Voronoi

model.

Multiphase field model. This model has been used to study the dynamics of confluent cell monolayers (19) and the mechanics of cell extrusion (20). It is a continuous model where each cell is described by a concentration field  $\varphi_c = \varphi_c(\mathbf{r})$ , with  $c = 1, 2 \dots N_{\text{cell}}$  and  $N_{\text{cell}}$  the total number of cells. The equilibrium state is defined by the free energy  $\mathcal{F} = \int dA f$  where the free energy density f is given by

$$f = \frac{\alpha}{4} \sum_{c} \varphi_c^2 (\varphi_c - \varphi_0)^2 + \frac{k_{\varphi}}{2} \sum_{c} (\nabla \varphi_c)^2 + \epsilon \sum_{c < c'} \varphi_c^2 \varphi_{c'}^2 + \sum_{c} \lambda \left( 1 - \frac{1}{\pi \varphi_0^2 R_{\varphi}^2} \int dA \varphi_c^2 \right)^2.$$
(4.5)

Here,  $\alpha$  and  $k_{\varphi}$  are material parameters which can be used to tune the surface tension  $\gamma = \sqrt{8\kappa_{\varphi}\alpha}$  and the interfacial thickness  $\xi = \sqrt{2\kappa_{\varphi}/\alpha}$  of isolated cells and thermodynamically favor spherical cell shapes. The constant  $\epsilon$  captures the repulsion between cells. The concentration field is large (i.e.  $\varphi_i \simeq \varphi_0$ ) inside the cells and zero outside. The contribution proportional to  $\lambda$  in the free energy enforces cell incompressibility whose nominal radius is given by  $R_{\varphi}$ . The phase field  $\varphi_i$  evolves according to the Allen-Cahn equation

$$\partial_t \varphi_c + \boldsymbol{v}_c \cdot \nabla \varphi_c = -M \frac{\delta \mathcal{F}}{\delta \phi_c},\tag{4.6}$$

where  $v_i = v_0(\cos\theta_c e_x + \sin\theta_c e_y)$  is the velocity at which the c-th cell self-propels, with  $v_0$  a constant speed and  $\theta_c$  an angle. The latter evolves according to the stochastic equation

$$\frac{\mathrm{d}\theta_c}{\mathrm{d}t} = \sqrt{2D} \, W_c,\tag{4.7}$$

where D is a constant controlling noise diffusivity and  $W_c = W_c(t)$  is a Wiener process. The constant M in Eq.(4.6) is the mobility, measuring the relevance of thermodynamic relaxation with respect to non-equilibrium cell migration. Eq.(4.6) is solved with a finite-difference approach through a predictor-corrector finite difference Euler scheme implementing second order stencil for space derivatives (21). Simulation details and scaling to physical units are given in Tab.4.1.

Voronoi model. This model portrays a confluent tissue as a Voronoi tessellation of the plane (22). Each cell is characterized by two dynamical

variables: the position  $r_c$  and the velocity  $v_c = v_0(\cos\theta_c e_x + \sin\theta_c e_y)$  with  $v_0$  a constant speed and  $\theta_c$  an angle, with  $c = 1, 2 \dots N_{\text{cell}}$  and  $N_{\text{cell}}$  the total number of cells. The dynamics of these variables is governed by the following set of ordinary differential equations

$$\frac{\mathrm{d}\boldsymbol{r}_c}{\mathrm{d}t} = \boldsymbol{v}_c - \mu \nabla_{\boldsymbol{r}_c} E,\tag{4.8a}$$

$$\frac{\mathrm{d}\theta_c}{\mathrm{d}t} = \eta_c,\tag{4.8b}$$

where  $\mu$  is a mobility coefficient and  $E = E(\mathbf{r}_1, \mathbf{r}_2 \dots \mathbf{r}_{N_{\text{cell}}})$  is an energy function defined as

$$E = \sum_{c} \left[ K_A (A_c - A_0)^2 + K_P (P_c - P_0)^2 \right].$$
 (4.9)

Here,  $A_c$  and  $P_c$  are respectively the area and perimeter of each cell and  $A_0$  and  $P_0$  their preferred values. The variable  $\eta_c$  in Eq.(4.8b) is white noise, having zero mean and correlation function

$$\langle \eta_c(t)\eta_{c'}(t')\rangle = 2D_{\rm r}\delta_{cc'}\delta(t-t') , \qquad (4.10)$$

with  $D_{\rm r}$  a rotational diffusion coefficient. Simulation details and scaling to physical units are given in Tab.4.1.

Numerical model							
	Multiphase field n	nodel					
Model p	arameter	Dimension	$Simulation\ value(s)$	Physical scaling			
	$N_{\text{cell}}$	_	361	_			
Lattice parameters	$\Delta x$	L	1	$0.685~\mu\mathrm{m}$			
Lattice parameters	$\Delta t$	T	1	1.414  s			
	$L_x, L_y$	L	380	246.6 μm			
	$M\alpha$	1/T	0.006	$0.0042 \text{ s}^{-1}$			
	$Mk_{\varphi}$	$L^2/T$	0.012	$0.0040 \ \mu m^2 \ s^{-1}$			
	$M\epsilon$	1/T	0.01	$0.0071 \text{ s}^{-1}$			
Free energy parameters	$M\lambda$	1/T	600	$424, 4 \text{ s}^{-1}$			
Tree energy parameters	$\varphi_0$	_	2.0	_			
	R	L	10.86	$7.4~\mu\mathrm{m}$			
	$\xi = \sqrt{2k_{\varphi}/\alpha}$	L	2	$1.37~\mu\mathrm{m}$			
	$\begin{cases} \xi = \sqrt{2k_{\varphi}/\alpha} \\ M\gamma = M\sqrt{8/9k_{\varphi}\alpha} \end{cases}$	L/T	0.008	$0.0039~\mu m~s^{-1}$			
D . 1	$D_r^{pf}$	1/T	0.0001	$0.00007 \text{ s}^{-1}$			
Dynamical equation parameter	$v_0$	L/T	0.0035	$0.00169~\mu m~s^{-1}$			
D:	Peclét number $Pe = v_0/(D_r R)$	_	3.22	_			
Dimensionless numbers	Cell deformability $d = \epsilon/\alpha$	_	1.66	_			
	Voronoi mode	l					
	$N_{\text{cell}}$	_	22500	_			
Lattice parameters	$\Delta t$	T	0.01	$0.53 \ s$			
	$L_x, L_y$	L	150	$2220~\mu m$			
	$\mu K_A$	$1/(L^2T)$	1	$0.0086~\mu s^{-1}$			
Energy parameters	$\mu K_P$	1/T	1	$0.98 \text{ s}^{-1}$			
пистуу разатыныны	$A_0$	$L^2$	1	$219.04~\mu m^{-2}$			
	$P_0$	L	3.9	57.72 μm			
Demanded equation representation	$v_0$	L/T	0.1	$27.8~\mu {\rm m~s}^{-1}$			
Dynamical equation parameter	$D_r'$	1/T	1	$0.019 \text{ s}^{-1}$			
Dimensionless numbers	Peclét $Pe = v_0/(D_r^V \sqrt{A_0})$	_	0.1	_			
Dimensioniess numbers	Shape index $p_0 = P_0/\sqrt{A_0}$	_	3.9	_			

Table 4.1: Physical scaling of simulation parameters. The table provides the parameters used to perform simulations for both the multiphase field and the Voronoi model, together with their dimensions and scaling to physical units. For the multiphase field model, scaling is performed by equating the mean cell radius  $R_{\rm cell}$  ( $\simeq 7.4~\mu m$ ) measured in experiments with the nominal cell radius R and a typical migration speed of cells in MDCK monolayers (4) ( $\simeq 2~\mu m~h^{-1}$ ) with that measured in our simulations ( $\simeq 0.0011~\Delta x/\Delta t$ ). This allows us to find the physical scaling of the lattice grid unit  $\Delta x$  and the iteration unit  $\Delta t$ . For the Voronoi model, we equated the mean cell radius  $R_{\rm cell}$  in experiments with that measured in simulations ( $\simeq 1$ ). The time-step was derived with the same procedure as described for the multiphase field model. In the table, simulation values are given in both lattice and physical units, in columns four and five, respectively. Notice that we did not introduce an energy scale as this cancels out with the mobility parameter M in Eq.(4.6) and  $\mu$  in Eq.(4.8), respectively.

#### Acknowledgements

This work is supported by the European Union via the ERC-CoGgrant HexaTissue (L.N.C., D.K. and L.G.) and by Netherlands Organization for Scientific Research (NWO/OCW) as part of the research program 'The active matter physics of collective metastasis' with project number Science-

XL 2019.022 (J.-M.A.-C. and L.G.). Part of this work was carried out on the Dutch national e-infrastructure with the support of SURF through the Grant 2021.028 for computational time. J.E. and L.G. acknowledge M. Gloerich, UMC Utrecht, for providing us the MDCK cells. All authors acknowledge Ludwig Hoffmann for fruitful discussions.

#### Author contributions

J.-M.A.-C. performed analytic work, Voronoi model simulations and analyzed data. L.N.C. coordinated the research, performed the multiphase field simulations and analyzed data. J.E. performed analytic work, experiments and analyzed data. D.K. performed analytic work and analyzed data. L.G. devised and coordinated the research. All authors wrote the paper. J.-M.A.-C., L.N.C., J.E. and D.K. contributed equally to this work.

#### Author information

The authors declare no competing financial interests.

#### 4.4 Supplementary

#### S4.4.1 The p-fold shape tensor

#### Definition and basic properties

In this supplementary Section, we explain the relation between the p-fold shape tensor  $G_p$ , Eq.(4.1), and the complex order parameter  $\gamma_p$ , Eq.(4.2). To build up intuition, we start from observing that the standard rank-2 shape tensor for a V-sided polygon, is given by (9, 34)

$$S = \frac{1}{V} \sum_{k=1}^{V} r_k \otimes r_k , \qquad (S4.11)$$

where, as in the main text,  $r_k$  represents the coordinate of the k-th vertex with respect to the center of mass of the cell. The spectral theorem allows one to represent S, as well as any other symmetric tensor, in terms of two irreducible components, one diagonal and the other traceless:

$$S = \bar{\lambda} \mathbb{1} + \Delta \lambda \left( e_1 \otimes e_1 - \frac{1}{2} \mathbb{1} \right) , \qquad (S4.12)$$

where we have set

$$\bar{\lambda} = \frac{\lambda_1 + \lambda_2}{2} , \qquad \Delta \lambda = \lambda_1 - \lambda_2 ,$$

with  $\lambda_1 > \lambda_2$  the two eigenvalues of S,  $e_1 = \cos \vartheta e_x + \sin \vartheta e_y$  the unit eigenvector associated with the largest eigenvalue  $\lambda_1$  and 1 the rank-2 identity tensor. The two terms in Eq.(S4.12) entail information about the polygon's size and anisotropy. The latter property can be further highlighted by introducing the tensor

$$G_2 = \frac{\llbracket \mathbf{S} \rrbracket}{\Delta_2} = \frac{\Delta \lambda}{\Delta_2} \llbracket \mathbf{e}_1^{\otimes 2} \rrbracket , \qquad (S4.13)$$

where  $\Delta_2 = \sum_{k=1}^{V} |\mathbf{r}_k|^2$ , the operator  $[\![\cdot\cdot\cdot]\!]$  has the effect of rendering its argument traceless and symmetric (13, 14) and the  $(\cdot\cdot\cdot)^{\otimes p}$  implies a p-fold tensorial product of the argument with itself: i.e.

$$e_1^{\otimes p} = \underbrace{e_1 \otimes e_1 \otimes \cdots \otimes e_1}_{p \text{ times}}$$
 (S4.14)

In two dimensions, the tensor  $G_2$  has only two linearly independent components and expressing it in the basis  $\{e_x, e_y\}$  readily gives

$$G_2 = \frac{\Delta \lambda}{2\Delta_2} \begin{bmatrix} \cos 2\vartheta & \sin 2\vartheta \\ \sin 2\vartheta & -\cos 2\vartheta \end{bmatrix} . \tag{S4.15}$$

Furthermore, explicitly diagonalizing Eq.(S4.11) gives

$$\vartheta = \frac{1}{2} \arctan \left( \frac{\sum_{k=1}^{V} |\mathbf{r}_{k}|^{2} \sin 2\phi_{k}}{\sum_{k=1}^{V} |\mathbf{r}_{k}|^{2} \cos 2\phi_{k}} \right) , \tag{S4.16a}$$

$$\Delta \lambda = \sqrt{\left(\sum_{k=1}^{V} |\boldsymbol{r}_k|^2 \sin 2\phi_k\right)^2 + \left(\sum_{k=1}^{V} |\boldsymbol{r}_k|^2 \cos 2\phi_k\right)^2},$$
 (S4.16b)

where  $\phi_k = \arctan(y_k/x_k)$  denotes the angular position of the k-th vertex with respect to the center of mass (Fig.4.1E). This construction implies that all components of the tensor  $G_2$  are proportional to either the real or imaginary part of the complex order parameter

$$\gamma_2 = \frac{1}{\Delta_2} \sum_{k=1}^{V} |\mathbf{r}_k|^2 e^{2i\phi_k} = \frac{\Delta \lambda}{\Delta_2} e^{2i\vartheta} , \qquad (S4.17)$$

so that

$$|\gamma_2| = \frac{\Delta \lambda}{\Delta_2} , \qquad \vartheta = \frac{\operatorname{Arg} \gamma_2}{2} .$$

Now, the same construction can be carried out for a generic rank-p shape tensor, by defining

$$G_p = \frac{1}{\Delta_p} \left[ \sum_{k=1}^{V} r_k^{\otimes p} \right], \tag{S4.18}$$

where  $\Delta_p = \sum_{k=1}^{V} |\mathbf{r}_k|^p$ . As for the rank-2 tensor defined in Eq.(S4.13), this tensor has only two linearly independent components, that are

$$g_1 = G_{p,xx\cdots x} = \frac{1}{2^{p-1}\Delta_p} \sum_{k=1}^{V} |\mathbf{r}_k|^p \cos(p\phi_k),$$
 (S4.19a)

$$g_2 = G_{p,xx\cdots y} = \frac{1}{2^{p-1}\Delta_p} \sum_{k=1}^{V} |\mathbf{r}_k|^p \sin(p\phi_k),$$
 (S4.19b)

and can be cast as in Eq.(S4.13), that is

$$G_p = \frac{\Delta \lambda_p}{\Delta_p} \left[ e^{\otimes p} \right] , \qquad (S4.20)$$

where the positive scalar  $\Delta \lambda_p$  and the unit vector  $\mathbf{e} = \cos \vartheta_p \, \mathbf{e}_x + \sin \vartheta_p \, \mathbf{e}_y$  are analogous to the difference  $\lambda_1 - \lambda_2$ , quantifying the anisotropy of the polygon, and the eigenvector  $\mathbf{e}_1$  associated with the largest eigenvalue. This problem ultimately relies on a generalization of the spectral theorem for tensors whose rank is larger than two. A possible strategy to achieve such as generalization was proposed by Virga in the context of rank-3 tensors (15) and consists of defining  $\vartheta_p$  as the inclination of a p-legged star oriented in such a way to maximize the probability of finding a vertex of the polygon in the direction of either one of the legs. The latter task is equivalent to solving the system of equations

$$G_p \odot e^{\otimes p-1} = \frac{\Delta \lambda_p}{\Delta_p} e ,$$
 (S4.21)

where  $\odot$  denotes a contraction of all matching indices of the two tensors on the left-hand side. After some lengthy calculations, partially summarized

in Sec. S4.4.1, one finds

$$\vartheta_p = \frac{1}{p} \arctan \left( \frac{\sum_{k=1}^{V} |\boldsymbol{r}_k|^p \sin(p\phi_k)}{\sum_{k=1}^{V} |\boldsymbol{r}_k|^p \cos(p\phi_k)} \right) , \tag{S4.22a}$$

$$\Delta \lambda_p = \sqrt{\left(\sum_{k=1}^{V} |\boldsymbol{r}_k|^p \cos\left(p\phi_k\right)\right)^2 + \left(\sum_{k=1}^{V} |\boldsymbol{r}_k|^p \sin\left(p\phi_k\right)\right)^2}.$$
 (S4.22b)

As in the case of the rank-2 shape tensor, one can then express all components of  $G_p$  in terms of the real and imaginary parts of the p-fold complex order parameter

$$\gamma_p = \frac{1}{\Delta_p} \sum_{k=1}^{V} |\mathbf{r}_k|^p e^{ip\phi_k} = \frac{\Delta \lambda_p}{\Delta_p} e^{ip\theta_p} , \qquad (S4.23)$$

so that

$$|\gamma_p| = \frac{\Delta \lambda_p}{\Delta_p} , \qquad \vartheta = \frac{\operatorname{Arg} \gamma_p}{p} .$$

#### Derivation of Eqs. (S4.22)

For sake of completeness, here we elaborate on the solution of Eq.(S4.21), leading to Eqs.(S4.22). The strategy, pioneered in Ref. (15), consists of mapping the diagonalization of a rank-p tensor to an optimization problem where  $\Delta \lambda_p \in \mathbb{R}$  is the Lagrange multiplier subjected to the constraint  $|e|^2 = e_x^2 + e_y^2 = 1$ . This task requires computing the tensorial power  $e^{\otimes p-1}$ , which, in turn, amounts to constructing all possible order-(p-1) products of  $e_x$  and  $e_y$ . The latter is facilitated by the fact that, as previously stated, the two-dimensional tensor  $G_p$  has only two linearly independent components, proportional to the functions  $g_1$  and  $g_2$  introduced in Eqs.(S4.19). In particular, depending on whether the number of y-indices of the generic element  $G_{i_1i_2\cdots i_p}$ , with  $i_p = \{x,y\}$ , is even or odd, the element is proportional to  $g_1$  and  $g_2$  respectively. Taken together, the aforementioned considerations result into the following expressions for the components of

the e vector:

$$\frac{\Delta \lambda_{p}}{\Delta_{p}} e_{x} = g_{1} \left[ \sum_{k \in \text{even}} (-1)^{\frac{k}{2}} {p-1 \choose k} e_{x}^{p-1-k} e_{y}^{k} \right] 
+ g_{2} \left[ \sum_{k \in \text{odd}} (-1)^{\frac{k-1}{2}} {p-1 \choose k} e_{x}^{p-1-k} e_{y}^{k} \right], \qquad (S4.24a)$$

$$\frac{\Delta \lambda_{p}}{\Delta_{p}} e_{y} = g_{2} \left[ \sum_{k \in \text{even}} (-1)^{\frac{k}{2}} {p-1 \choose k} e_{x}^{p-1-k} e_{y}^{k} \right] 
- g_{1} \left[ \sum_{k \in \text{odd}} (-1)^{\frac{k-1}{2}} {p-1 \choose k} e_{x}^{p-1-k} e_{y}^{k} \right]. \qquad (S4.24b)$$

Despite their apparently complexity, these equations can be considerably simplified leading to

$$\frac{\Delta \lambda_p}{\Delta_p} \cos \theta_p = g_1 \cos \left[ (p-1) \,\theta_p \right] + g_2 \sin \left[ (p-1) \,\theta_p \right], \qquad (S4.25a)$$

$$\frac{\Delta \lambda_p}{\Delta_p} \sin \vartheta_p = g_2 \cos \left[ (p-1) \vartheta_p \right] - g_1 \sin \left[ (p-1) \vartheta_p \right]. \tag{S4.25b}$$

If  $g_1 = 0$ , Eqs.(S4.25) reduces to

$$\cot \vartheta_p = \tan \left[ (p-1) \vartheta_p \right] , \qquad (S4.26)$$

which has  $2\,p$  solutions in the range  $0 \leq \vartheta_p < 2\pi$  given by

$$\vartheta_p^{(k)} = \frac{2k+1}{p} \pi , \qquad k = 0, 1 \dots 2p-1 .$$
 (S4.27)

Conversely, when  $g_1 \neq 0$ , setting  $\varrho = g_2/g_1$  and solving Eqs.(S4.25) with respect to  $\vartheta_p$  gives

$$\cot \vartheta_p = \frac{\cos \left[ (p-1) \vartheta_p \right] + \varrho \sin \left[ (p-1) \vartheta_p \right]}{\varrho \cos \left[ (p-1) \vartheta_p \right] - \sin \left[ (p-1) \vartheta_p \right]}, \tag{S4.28}$$

from which one can readily find

$$\varrho = \tan p \vartheta_p \,, \tag{S4.29}$$

whose solution is given by

$$\vartheta_p^{(k)} = \frac{\arctan \varrho + k\pi}{p} , \qquad k = 0, 1...2p - 1 ,$$
 (S4.30)

thereby completing the derivation of Eq.(S4.22a). To compute  $\Delta \lambda_p$ , one can use again Eqs.(S4.25) and express  $g_1$  and  $g_2$  in terms of coordinates. This gives, after some direct calculations,

$$\left| \Delta \lambda_p^{(k)} \right| = |g_1| \sqrt{1 + \varrho^2}$$

$$= \frac{1}{2^{p-1}} \sqrt{\left( \sum_{i=1}^{V} |\mathbf{r}_i|^p \cos(p\phi_i) \right)^2 + \left( \sum_{i=1}^{V} |\mathbf{r}_i|^p \sin(p\phi_i) \right)^2} .$$
 (S4.31)

Note that, because of the periodicity of  $\vartheta_p^{(k)}$ , then  $\Delta \lambda_p^{(k)} = -\lambda_p^{(k+1)}$ , whereas the sign of  $\lambda_p^{(0)}$  depends on  $\varrho$  and  $g_1$ . Finally, to cast the tensor  $\mathbf{G}_p$  in the form given in Eq.(S4.20), one can write  $g_1 = \Delta \lambda_p \hat{g}_1$  and  $g_2 = \Delta \lambda_p \hat{g}_2$  where

$$\hat{g}_1 = \frac{1}{2^{p-1}\Delta_p}\,\cos p\vartheta_p\;, \qquad \hat{g}_2 = \frac{1}{2^{p-1}\Delta_p}\,\sin p\vartheta_p$$

are the two independent components of  $[e^{\otimes p}]/\Delta_p$ . Then, using the expression of  $\vartheta_p$  given in Eq.(S4.27) and Eq.(S4.30), one obtains

$$\Delta \lambda_p = 2^{p-1} \left| \Delta \lambda_p^{(k)} \right| , \qquad k = 0, 1 \dots 2p - 1 ,$$
 (S4.32)

which completes the derivation of Eq.(S4.22b).

#### S4.4.2 Defect representation in p-atic liquid crystals

In two-dimensional liquid crystals, topological defects consist of point-like singularities in the orientational field, that are points where the orientations of the director field are not univocally defined, and can be classified in terms of the winding number s defined in the main text. In liquid crystals with p-fold rotational symmetry, the latter is an integer multiple of the elementary winding number 1/p. By contrast, it is impossible to correctly describe a defect of winding number  $s = \pm 1/p$  in terms of an orientation field with rotational symmetry other than p-fold.

To substantiate this statement, we consider here the common case of a pair of  $\pm 1/2$  disclinations in a nematic liquid crystal (p = 2), respectively located at positions  $\mathbf{r}_+ = x_+ \mathbf{e}_x + y_+ \mathbf{e}_y$  and  $\mathbf{r}_- = x_- \mathbf{e}_x + y_- \mathbf{e}_y$ . The far-field configuration of the phase  $\vartheta_2 = \operatorname{Arg}(\Gamma_2)/2$  is given by

$$\vartheta_2 = \frac{1}{2} \left[ \arctan \left( \frac{y - y_+}{x - x_+} \right) - \arctan \left( \frac{y - y_-}{x - x_-} \right) \right] . \tag{S4.33}$$

In turn, the 2-fold orientation field can be visualized as the standard headless nematic director - i.e. a 2-legged star - as in Fig.4.1A of the main

text. Now, as illustrated in Fig.4.3E, attempting to describe the same 2—fold symmetric configuration with a, say, 1—fold symmetric orientation filed — i.e. a standard vector field — results in a discontinuity of magnitude  $\pi$  of the associated phase  $\vartheta_1$  across the x-axis.

The same issue occurs while attempting to describe a pair of  $s=\pm n/p$  defects (with n a real number) in by means of a q-fold orientation filed, with q < p. In this case, the far-field configuration of the phase  $\vartheta_p$  is given by

$$\vartheta_p = \frac{n}{p} \left[ \arctan \left( \frac{y - y_+}{x - x_+} \right) - \arctan \left( \frac{y - y_-}{x - x_-} \right) \right], \tag{S4.34}$$

and it can be graphically represented by a p-legged star oriented at angles  $\vartheta_p + 2\pi n/p$ , with  $n=1, 2 \dots p$ , so that the order parameter  $\Gamma_p = |\Gamma_p| \exp(ip\vartheta_p)$  is continuous everywhere, but at the defect position. We attempt to describe the same configuration in terms of the order parameter  $\Gamma_q = |\Gamma_q| \exp(iq\vartheta_q)$ , corresponding to q-legged stars oriented at an angle  $\vartheta_q + 2\pi n/q$ , with  $n=1, 2 \dots q < p$ . For the purpose of this discussion, and without loss of generality, we set  $y_+ = y_- = y_0$  and compute the variation of  $\Gamma_q$ . While crossing the line, the axis  $y=y_0$  in the region comprised between the two defects  $(x_- < x < x_+)$ . Since the q-legged star associated with the order parameter  $\Gamma_q$  is invariant under rotations by  $2\pi/q$ , the inclination of the leg closer to the x-axis undergoes a discontinuity of magnitude

$$|\Delta \vartheta_q| = 2\pi \min\left(\frac{n}{p}, \frac{|p - nq|}{pq}\right) . \tag{S4.35}$$

Thus, the field  $\vartheta_q$  is continuous everywhere, but at the defect position  $(|\Delta\vartheta_q|=2\pi m/p \text{ with } m \text{ any natural number})$  only when p=q or nq is an integer multiple of p. In particular, describing a defect of winding number s=1/6 (n=1 and p=6) by means of a nematic field with q=2 would result into a jump of magnitude  $|\Delta\vartheta_2|=\pi/3$  as shown in Fig.4.3E in the main text. The resulting configuration of the nematic director features a singular line connecting defects of opposite charge.

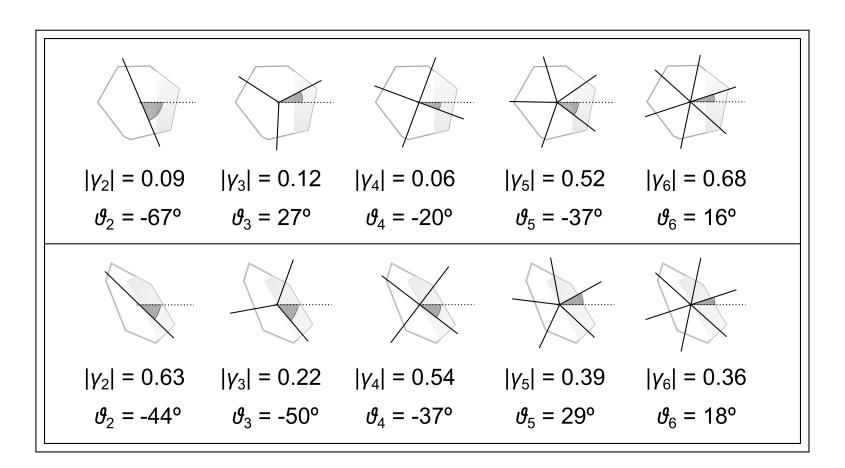


Figure S4.4: Order parameter  $\gamma_p$ . Top and bottom panels show the p-atic star for the polygonal shapes in Fig.4.1E and Fig.4.1F, respectively. The magnitude of the order parameter  $|\gamma_p|$  and its orientation  $\vartheta_p$  with respect to the polar axis (dashed horizontal line) are given for  $p=2,\ldots,6$ .

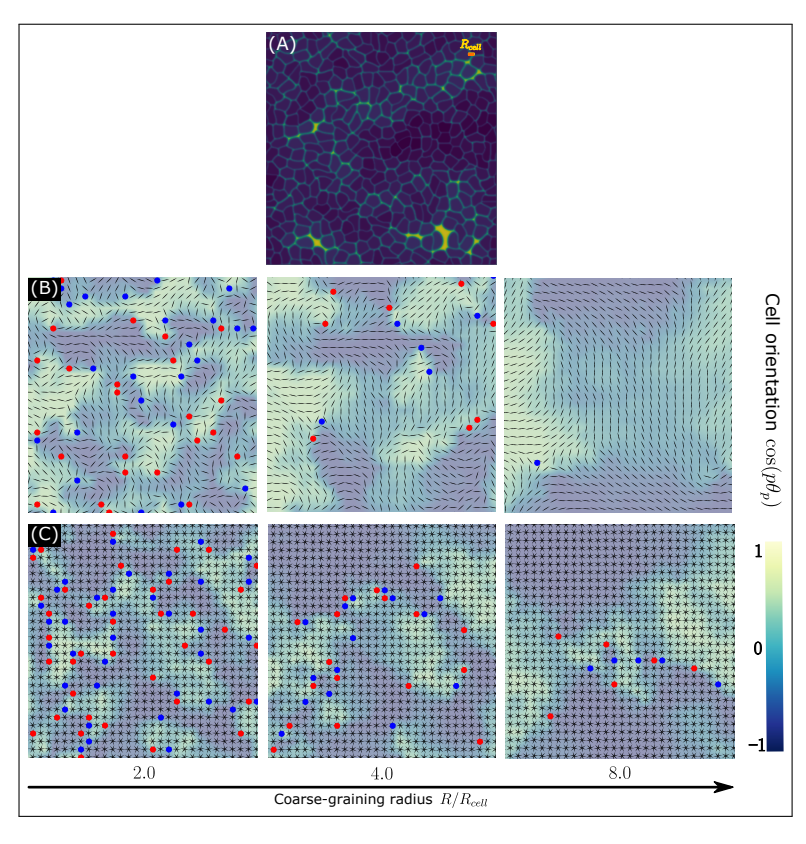


Figure S4.5: Coarse-graining the multiphase field model. (A), A typical configuration of the multiphase field simulations with 360 cells. Darker regions correspond to areas dense with cells and lighter regions to areas where cells are sparser. (B,C), Nematic (top row) and hexatic (bottom row) coarse-grained fields  $\Gamma_2$  and  $\Gamma_6$  versus the coarse-graining radius R, expressed in units of the nominal cell size  $R_{cell}$ . In both panels, positive and negative defects are marked in red and blue respectively ( $\pm 1/2$  for nematic and  $\pm 1/6$  for hexatic).

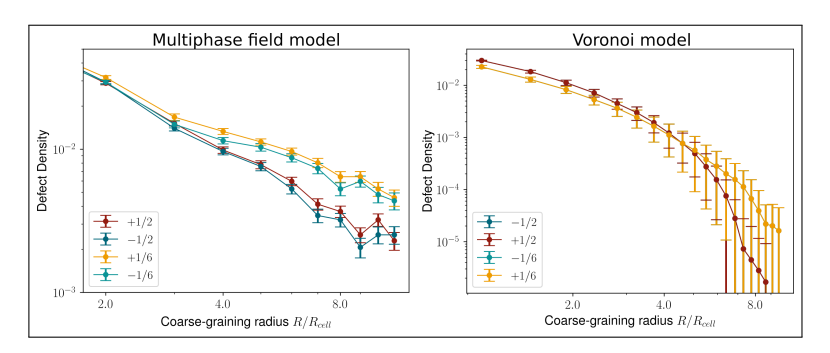


Figure S4.6: Decay of defect density in simulations. Left and right panels show the decay of the defect density at varying the coarse-graining radius in simulations of the multiphase field model (left) and Voronoi model (right). The scaling of multiphase field model data is compatible with that shown in Fig.4.3D in the main text for experimental data. In the right panel, curves of oppositely charged defects overlap exactly.

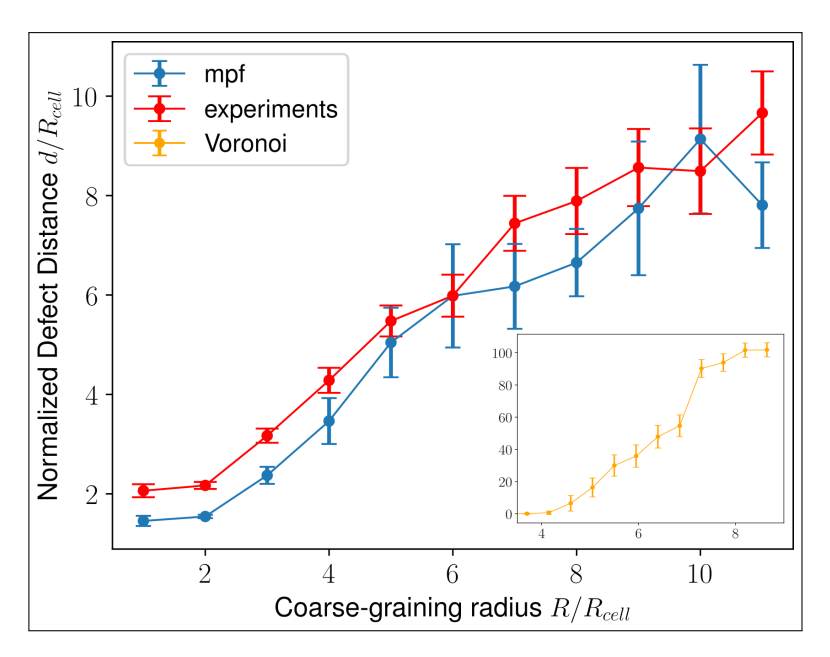


Figure S4.7: Separation of hexatic and nematic defects at varying the coarse-graining radius. The graph shows the mean distance between a hexatic defect and the closest nematic defect, regardless of their charge, computed for experimental data, multiphase field simulations and Voronoi simulations (inset). Experimental data (red curve) and multiphase field simulation (blue curve) are in qualitative agreement.

- Duclos, G., Erlenkämper, C., Joanny, J.-F., and Silberzan, P. (2016). Topological defects in confined populations of spindle-shaped cells. *Nat. Phys.* 13, 58–62.
- (2) Saw, T. B., Doostmohammadi, A., Nier, V., Kocgozlu, L., Thampi, S., Toyama, Y., Marcq, P., Lim, C. T., Yeomans, J. M., and Ladoux, B. (2017). Topological defects in epithelia govern cell death and extrusion. *Nature* 544, 212–216.
- (3) Kawaguchi, K., Kageyama, R., and Sano, M. (2017). Topological defects control collective dynamics in neural progenitor cell cultures. *Nature* 545, 327–331.
- (4) Balasubramaniam, L., Doostmohammadi, A., Saw, T. B., Narayana, G. H. N. S., Mueller, R., Dang, T., Thomas, M., Gupta, S., Sonam, S., Yap, A. S., Toyama, Y., Mège, R.-M., Yeomans, J. M., and Ladoux, B. (2021). Investigating the nature of active forces in tissues reveals how contractile cells can form extensile monolayers. *Nature Materials* 20, 1156–1166.
- (5) Li, Y.-W., and Ciamarra, M. P. (2018). Role of cell deformability in the twodimensional melting of biological tissues. *Phys. Rev. Materials* 2, 045602.
- (6) Durand, M., and Heu, J. (2019). Thermally driven order-disorder transition in two-dimensional soft cellular systems. Phys. Rev. Lett. 123, 188001.
- (7) Pasupalak, A., Yan-Wei, L., Ni, R., and Pica Ciamarra, M. (2020). Hexatic phase in a model of active biological tissues. Soft Matter 16, 3914–3920.
- (8) Maroudas-Sacks, Y., Garion, L., Shani-Zerbib, L., Livshits, A., Braun, E., and Keren, K. (2021). Topological defects in the nematic order of actin fibres as organization centres of Hydra morphogenesis. *Nature Physics* 17, 251–259.
- (9) Hoffmann, L. A., Carenza, L. N., Eckert, J., and Giomi, L. (2022). Theory of defect-mediated morphogenesis. Science Advances 8, eabk2712.
- (10) Streichan, S. J., Lefebvre, M. F., Noll, N., Wieschaus, E. F., and Shraiman, B. I. (2018). Global morphogenetic flow is accurately predicted by the spatial distribution of myosin motors. *Elife* 7, e27454.
- (11) Bigun, J., Optimal orientation detection of linear symmetry; Linköping University Electronic Press: 1987.
- (12) Aubouy, M., Jiang, Y., Glazier, J. A., and Graner, F. (2003). A texture tensor to quantify deformations. *Granul. Matter* 5, 67–70.
- (13) Asipauskas, M., Aubouy, M., Glazier, J. A., Graner, F., and Jiang, Y. (2003). A texture tensor to quantify deformations: the example of two-dimensional flowing foams. *Granul. Matter* 5, 71–74.
- (14) Chaikin, P. M., and Lubensky, T. C., *Principles of condensed matter physics*; Cambridge University Press: Cambridge, 1995.

- (15) Friedel, G. (1922). Les états mésomorphes de la matière. Ann. Phys. 9, 273–474.
- (16) Giomi, L., Toner, J., and Sarkar, N. (2022). Long-Ranged Order and Flow Alignment in Sheared p—atic Liquid Crystals. Phys. Rev. Lett. 129, 067801.
- (17) Giomi, L., Toner, J., and Sarkar, N. (2022). Hydrodynamic theory of p-atic liquid crystals. Phys. Rev. E 106, 024701.
- (18) Virga, E. G. (2015). Octupolar order in two dimensions. Eur. Phys. J. E 38, 63.
- (19) Loewe, B., Chiang, M., Marenduzzo, D., and Marchetti, M. C. (2020). Solid-liquid transition of deformable and overlapping active particles. *Phys. Rev. Lett.* 125, 038003.
- (20) Monfared, S., Ravichandran, G., Andrade, J. E., and Doostmohammadi, A. (2021). Mechanics of live cell elimination. arXiv:2108.07657.
- (21) Carenza, L. N., Gonnella, G., Lamura, A., Negro, G., and Tiribocchi, A. (2019). Lattice Boltzmann methods and active fluids. Eur. Phys. J. E 42, 81.
- (22) Bi, D., Yang, X., Marchetti, M. C., and Manning, M. L. (2016). Motility-driven glass and jamming transitions in biological tissues. *Physical review. X* 6, 021011.
- (23) Kittel, C., and McEuen, P., Introduction to solid state physics; Wiley New York: 1996; Vol. 8.
- (24) De Pascalis, C., and Etienne-Manneville, S. (2017). Single and collective cell migration: the mechanics of adhesions. *Mol. Biol. Cell* 28, 1833–1846.
- (25) Friedl, P., and Gilmour, D. (2009). Collective cell migration in morphogenesis, regeneration and cancer. *Nat. Rev. Mol. Cell Bio.* 10, 445–457.
- (26) Keber, F. C., Loiseau, E., Sanchez, T., DeCamp, S. J., Giomi, L., Bowick, M. J., Marchetti, M. C., Dogic, Z., and Bausch, A. R. (2014). Topology and dynamics of active nematic vesicles. *Science* 345, 1135–1139.
- (27) Guillamat, P., Blanch-Mercader, C., Pernollet, G., Kruse, K., and Roux, A. (2022). Integer topological defects organize stresses driving tissue morphogenesis. Nature Materials 21, 588–597.
- (28) Armengol-Collado, J.-M., Carenza, L. N., and Giomi, L. (2022). Hydrodynamics and multiscale order in confluent epithelia. arXiv:2202.00651.
- (29) Blankenship, J. T., Backovic, S. T., Sanny, J. S., Weitz, O., and Zallen, J. A. (2006). Multicellular Rosette Formation Links Planar Cell Polarity to Tissue Morphogenesis. Dev. Cell 11, 459–470.
- (30) Rauzi, M. (2020). Cell intercalation in a simple epithelium. Phil. Trans. R. Soc. B 375, 20190552.
- (31) Haeger, A., Alexander, S., Vullings, M., Kaiser, F. M., Veelken, C., Flucke, U., Koehl, G. E., Hirschberg, M., Flentje, M., Hoffman, R. M., et al. (2020). Collective cancer invasion forms an integrin-dependent radioresistant niche. J. Exp. Med> 217.
- (32) Serra-Picamal, X., Conte, V., Vincent, R., Anon, E., Tambe, D. T., Bazellieres, E., Butler, J. P., Fredberg, J. J., and Trepat, X. (2012). Mechanical waves during tissue expansion. Nat. Phys. 8, 628–634.
- (33) Yamada, S., Pokutta, S., Drees, F., Weis, W. I., and Nelson, W. J. (2005). Deconstructing the Cadherin-Catenin-Actin Complex. *Cell* 123, 889–901.

(34) Maroudas-Sacks, Y., Garion, L., Shani-Zerbib, L., Livshits, A., Braun, E., and Keren, K. (2021). Topological defects in the nematic order of actin fibres as organization centres of Hydra morphogenesis. *Nature Physics* 17, 251–259.

# Hexanematic crossover in epithelial monolayers depends on cell adhesion and cell density

During tissue folding in developmental processes and monolayer migration in wound healing, epithelial cells undergo shape changes and move collectively. Recent experimental and numerical results suggested that these processes could leverage on the existence of both nematic (2-fold) and hexatic (6-fold) orientational order coexisting at different length scales within the same epithelial layer. Yet, how this remarkable example of multiscale organization in living matter is affected by the material properties of the cells and their substrate is presently unknown. In the current article, we experimentally address these questions in monolayers of Madin-Darby canine kidney cells (MDCK-II) having various cell density and molecular repertoire. At small length scales, confluent monolayers are characterized by a prominent hexatic order and nearly vanishing nematic order, independently on the presence of E-cadherin, the monolayer density, and the underlying substrate stiffness. All three properties, however, dramatically affect the organization of MDCK-II monolayers at large length scales, where nematic order becomes dominant over hexatic order. In particular, we find that the length scale at which nematic order prevails over hexatic order – here referred to as hexanematic crossover scale – strongly depends on cell-cell adhesions and correlates with the monolayer density. Our analysis sheds light on how the organization of epithelial layers is affected by the material and mechanical properties, and provides a robust approach for analyzing the tissue composition towards understanding developmental processes.

Eckert, J., Ladoux, B., Giomi, L., Schmidt, T. (2022). Hexanematic crossover in epithelial monolayers depends on cell adhesion and cell density. bioRxiv 2022.10.07.511294.

5.1 Introduction 105

#### 5.1 Introduction

The collective behavior of cells drives tissue patterning and folding during gastrulation, and is involved in wound healing and metastasis (1-5). Such processes rely on the cross-talk between extracellular matrix adhesions and cell-cell connections through cell junction proteins. Any extracellular changes trigger, for example, the recruitment of focal adhesion molecules, the rearrangement of the actin network at the cell-substrate interface and cell cortex, and causes actomyosin contractions within the cell (6-10). These biochemical processes, in turn, affect the cell's shape and mechanical properties, thereby influencing the cellular organization at larger length scales (3, 11, 12).

Among the various aspect of multicellular organization, orientational order has recently been identified as an essential concept, because of its inherent propensity towards enhancing the coherence of microscopic forces that would be incoherent (randomly oriented) otherwise (13-19). Elongated cells, such as fibroblasts (13), neurons (14), and potentially any mesenchymal phenotypes, tend, for instance, to align with each other, thereby giving rise to polar (20, 21) or nematic (14, 15, 22-24) phases, whose spatial structure and dynamics facilitate a number of biomechanical processes. These include the onset of organism-wide cellular flows during gastrulation (25), the development of protrusion and tentacles-like features (18, 26), or the extrusion of apoptotic cells (15). By contrast, various epithelial phenotypes form honeycomb-like structures, held together by cadherin-mediated junctions, where cells are confluent, yet able to move by remodeling of the local honeycomb network. Previous numerical studies suggested that, as other two-dimensional assemblies of equally-sized isotropic building blocks, epithelial layers resemble hexatic liquid crystals: anisotropic fluids featuring quasi-long-ranged 6-fold orientational order (27-29). More recently, this picture has been further elaborated by experimental ((30); Chapter 4)) and theoretical (31) studies, which indicated that certain epithelial layers feature, in fact, a unique combination of nematic and hexatic order, with the former being dominant at large and the latter at small length scale. These two types of liquid crystal order crossover at intermediate length scales – corresponding roughly to clusters of a dozen cells for MDCK GII on non-coated glass ((30); Chapter 4) – where the local hexagonal structure inherited from the shape of individual cells is gradually replaced by the uniaxial arrangement caused by clustering of cells into chain-like assemblies.

It has been speculated that the specific magnitude of such a *hexanematic* crossover scale – hereafter referred to as  $R_{\times}$  – could affect the strategy of epithelial layers with respect to collective migration (31). Depending on

the length scale, L, at which it is confined, an epithelial layer could select among the different motility modes at its disposal. E.g. metastatic cells invading the extracellular matrix by collectively migrating through micronsized channels, for which  $L \ll R_{\times}$ , are more likely to adopt migration strategies based on intercalation and other remodeling events rooted into small scale hexatic order. Conversely, the organism-wide collective flow observed in morphogenetic process, for which  $L \gg R_{\times}$ , could in principle result from the large scale spontaneous flow that is routinely observed in active nematics. But what sets the magnitude of  $R_{\times}$ , and how it can be controlled by epithelia in order to accomplish their biological functions is presently unknown.

In this article, we address these questions by measuring the hexanematic crossover length scale,  $R_{\times}$ , in epithelial and mesenchymal-like MDCK-II layers, for various cell densities and stiffness of the underling substrate. Our analysis indicates that both properties influence the hexanematic crossover. We experimentally confirmed that a hexatic symmetry overweights any nematic symmetry at the level of individual cells in confluent monolayers, independent of the magnitude and ratio of cell-cell and cell-matrix interaction. Yet at the tissue level, order is dominated by a nematic phase. We demonstrated that the hexanematic crossover shifts towards shorter length scales for decreasing monolayer density and reduction of the cell-cell interaction. Furthermore, we observed that the approach towards the crossover length scale is crucially related with the specific cellular phenotype and its location along the epithelial-mesenchymal spectrum. Finally, we suggest that the hexanematic crossover length scale adds a phenotypic parameter that discerns whether cellular behavior is individual or collective.

#### 5.2 Results

# 5.2.1 Reduced cell-cell adhesion increases the shape index and decreases the monolayer density

The cell density in confluent epithelial monolayers affects the morphology and the motility of cells therein (32, 33). It has been proposed that changes in cell shape and motility crucially depend on the development of stable cell-cell adhesions, because of their interplay with the cellular contractility (34).

As a starting point, we investigated how the cell shape is affected by the interaction between cells. To this end, we compared the shape of epithelial MDCK type II wild-type (WT) cells with that of mesenchymal-like MDCK-II E-cadherin knock-out cells (E-cad KO) (19). A reduced level

5.2 Results 107

of cell-cell contacts was maintained in MDCK E-cad KO cells through cadherin-6 (19). Both cell lines, MDCK WT and E-cad KO, were cultured for three days, including two days at confluency, on non-coated glass. Subsequently, samples were fixed and immunostained for the tight junction protein ZO-1, which is localized near the apical surface of cells to determine cell boundaries. We thus used the ZO-1 signal to identify the cell vertex positions and reconstructed a polygon of each cell (Fig.5.1A-B). Using the polygon, we calculated the shape index,  $p_0$ , defined as the ratio between a cell's perimeter, P, and the square root of its area, A,  $p_0 = P/\sqrt{A(35-37)}$ , and conventionally used as an indicator of the cell's shape. By averaging over all mean cell shape indices of all monolayers imaged, we identified that MDCK WT cells had a smaller shape index of 4.06  $\pm$  0.07 (mean  $\pm$ s.d.) compared to MDCK E-cad KO cells with 4.20  $\pm$  0.21 (mean  $\pm$  s.d.), p-value < 0.0001 (Fig.5.1C). This observation is in line with the smaller cell aspect ratio for MDCK WT cells compared to MDCK E-cad KO cells that has been reported earlier (19).

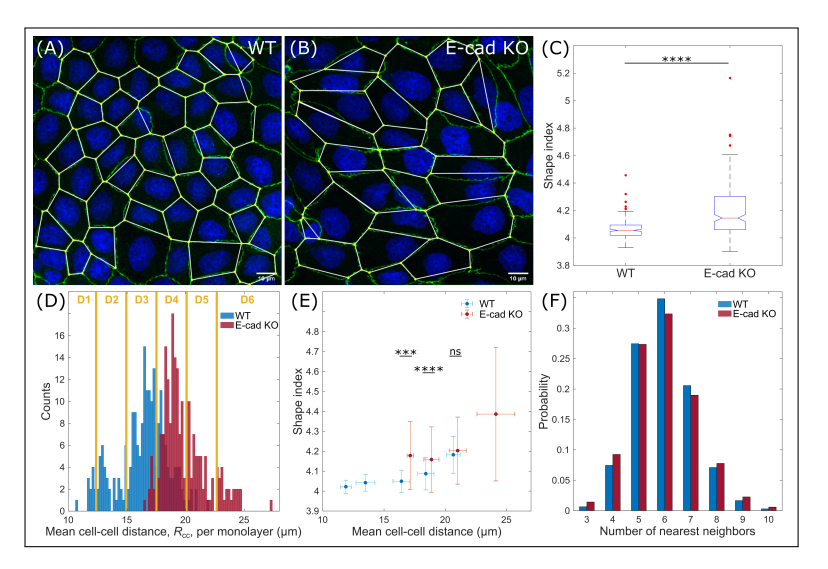


Figure 5.1: The cell shape index decreases with increasing monolayer density. (A,B), Confocal image of confluent MDCK-II WT and E-cad KO monolayers (green, ZO-1 and blue, nuclei), cultured on non-coated glass. Cells were segmented, and their shape reconstructed by connecting the vertices. (C) Cell shape index of both cell lines. (D), Distribution of the mean cell-cell distance,  $R_{cc}$ . The bin-width is 0.2  $\mu$ m. For further analysis, monolayers were grouped in six intervals, D1-D6, of 2.6  $\mu$ m-width each  $(N_{WT}=226$  and  $N_{KO}=216$  from three independent experiments). (E), Mean shape index increases with  $R_{cc}$ . (F), The probability distribution of the number of nearest neighbors per cell. Error bars represent the standard deviation. Two-sided Wilcoxon rank sum test: \*\*\* p < 0.001, \*\*\*\* p < 0.0001, \*\* p > 0.5.

When we compared the morphology of the MDCK WT and E-cad KO cell-monolayers, it appeared that MDCK WT cells were more densely packed and approximately round (Fig.5.1A), while MDCK E-cad KO cells were larger and elongated (Fig.5.1B). We then asked whether the density distributions between both cell lines were different, and whether that was reflected in the shape index. To address this questions, we calculated the mean cell-cell distance between neighboring cells as an indicator for the density. By comparing the distributions between both cell lines, we found that MDCK E-cad KO cells, on average, assumed a larger cell-cell distance of 19.9  $\pm$  1.0  $\mu$ m (mean  $\pm$  s.d.), i.e. one cell per 200  $\pm$  103  $\mu$ m², compared to MDCK WT cells of 16.4  $\pm$  2.1  $\mu$ m (mean  $\pm$  s.d.), i.e. one cell per 295  $\pm$  153  $\mu$ m², (Fig.5.1D). Therefore, it is conceivable that the larger shape index of MDCK E-cad KO cells was caused by the increased cell-cell distance, i.e. decreased monolayer density.

To assess the correlation between the shape index to the monolayer density, we grouped monolayers according to their mean cell-cell distance,  $R_{\rm cc}$ , in six intervals (D1-D6 in Fig.5.1D). Upon increasing the cell-cell distance – thus decreasing the monolayer density – we observed a monotonic increase in the shape index for both cell lines (Fig.5.1E), thus corroborating previous experimental observations (33). MDCK E-cad KO cells assumed a significant larger shape index compared to MDCK WT cells at smaller comparable density intervals ( $R_{\rm cc} \leq 20.1\,\mu{\rm m}$ ; D3-D4). For the largest cell-cell distance interval measured (20.1  $\mu{\rm m} \leq R_{\rm cc} < 22.7\,\mu{\rm m}$ ; D5), the mean shape indices for both cell lines were indistinguishable.

Taken together, the mesenchymal-like MDCK E-cad KO cells had an overall larger shape index and a smaller cell density compared to MDCK WT cells. In the same density interval, MDCK E-cad KO cells had either a larger or the same shape index compared to MDCK WT cells.

#### 5.2.2 Hexagonality in epithelia increases with density

As previously mentioned, epithelial layers exhibit hexatic order at the small scale, by virtue of the approximate 6-fold symmetry of individual cells. The latter, in turn, is a natural consequence of the fact that, in two dimensions, isotropic particles pack more densely when arranged in a honeycomb lattice. For rigid disks, this mechanism yields the packing fraction  $\phi_{\text{honeycomb}} = \pi \sqrt{3}/6 \approx 0.91$ , while the remaining fraction, i.e.  $1 - \phi_{\text{honeycomb}} \approx 0.09$ , is occupied by the gaps in between the disks. Evidently, the same limitation does not exist in the case of deformable particles, as these can fill the gaps by adapting to the hexagonal geometry of their neighborhood, eventually reaching confluency (i.e.  $\phi_{\text{confluent}} = 1$ ). These

5.2 Results 109

considerations suggest that the 'hexagonality' of individual epithelial cells would increase with the monolayer density.

To test this hypothesis, we measured the 6-fold shape parameter,  $\gamma_6$ , introduced in Ref. (30) and Chapter 4 in both, the MDCK WT and the E-cad KO cell line, and compared it with the 2-fold shape parameter,  $\gamma_2$ , for all individual cells (Fig.S5.5A-B). These two metrics consist of specific instances of a generic p-fold shape parameter, defined in Eq.(5.1), quantifying the resemblance of an arbitrary polygon to a p-sided regular polygon (or rod for p=2), having the same position and size. Further, we calculated the ensemble average of the shape parameters,  $\langle |\gamma_n| \rangle$ , (see Eq.(5.2) in Methods). Regardless of the monolayer density and cell line, the mean 6-fold shape parameter was found to be always larger than the 2-fold shape parameter at the scale of individual cells (Fig. 5.2A; Fig.S5.5A-B). Furthermore, upon increasing cell-cell distance, the difference  $\langle |\gamma_6| \rangle - \langle |\gamma_2| \rangle$  decreased (Fig.5.2B). At the largest cell-cell distance interval (D6) of  $24.1 \pm 1.5 \,\mu m$  (mean  $\pm s.d.$ ), both symmetries were equally prominent, while the difference between MDCK WT and E-cad KO cells disappeared (Fig.5.2A).

By comparing the individual shape parameters of both MDCK WT and E-cad KO cells in the same monolayer density interval, it appeared that the 6-fold shape parameter did not differ in all overlapping density intervals (Fig.5.2A; p-value > 0.05). On the other hand, the 2-fold shape parameter of MDCK E-cad KO cells were significantly larger for cell-cell distances in the interval  $R_{\rm cc} \leq 20.1\,\mu{\rm m}$  (D3-D4; p-value < 0.0001) and equal in the interval  $20.1\,\mu{\rm m} \leq R_{\rm cc} < 22.7\,\mu{\rm m}$  (D5; p-value > 0.05) compared to MDCK WT cells. This trend in the behavior of  $\langle |\gamma_2| \rangle$  in MDCK WT and E-cad KO cells at similar density intervals echos that observed in the behavior of the shape index (Fig.5.1E) as also demonstrated by the large correlation between these two parameter (correlation coefficient:  $0.93 \leq r \leq 0.97$ ; see Fig.5.2C).

From these observations, we concluded that decreasing monolayer density – increasing cell-cell distance – as well as reducing cell-cell adhesions led to an elongation of cells, which can be equivalently captured by either the cell shape index or the 2–fold shape parameter,  $\gamma_2$ . By contrast, 6–fold symmetry always overweights 2–fold symmetry at the single-cell level, independently on the monolayer density and the strength of cell-cell adhesion. Hence, individual cells in confluent monolayers were statistically more hexagonal rather than elongated.

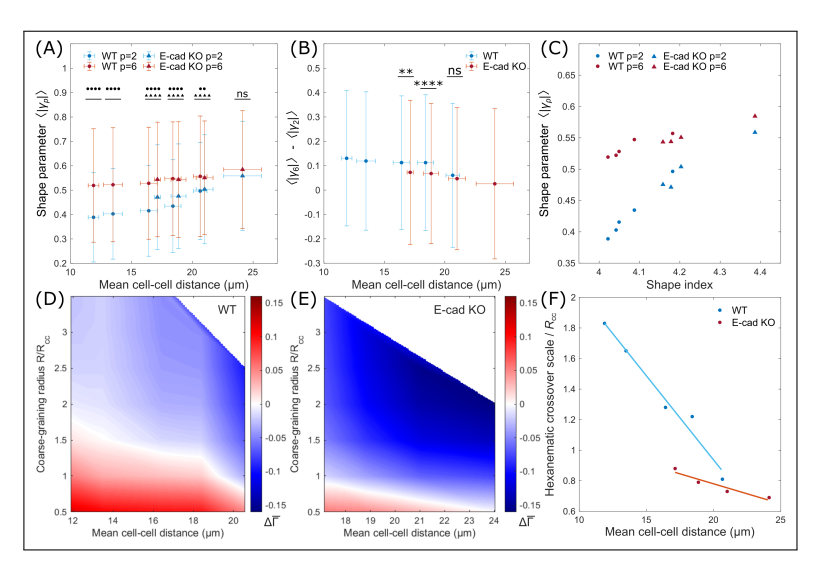


Figure 5.2: The dominance and length scale of the hexatic order depends on the monolayer density and cell line. (A), The magnitude of the shape parameter,  $\langle |\gamma_p| \rangle$ , for different mean cell-cell distances. Differences between the hexatic and nematic shape parameters,  $\langle |\gamma_6| \rangle - \langle |\gamma_2| \rangle$ , are shown in (B). (C), Correlation between the mean shape index and mean shape parameter. (D,E), The difference between the scale-dependent hexatic and nematic shape parameter,  $\Delta \overline{\Gamma} = \overline{\Gamma}_6 - \overline{\Gamma}_2$ , plotted as a function of the coarse-graining radius and the mean cell-cell distance for MDCK-II WT (D) and E-cad KO cells (E). Red and blue tones regions of the parameter space where hexatic order prevails over nematic order and vice versa. The white line marks the hexanematic crossover, which is the length scale  $R_{\times}$  where  $\overline{\Gamma}_6 = \overline{\Gamma}_2$ . Individual plots can be seen in Fig.S5.5C-D. (F), Hexanematic crossover scale versus the mean cell-cell distance. Error bars represent the standard deviation. Two-sided Wilcoxon rank sum test: \*\* p < 0.01, \*\*\*\* p < 0.0001, \*\*\* p > 0.5.

#### 5.2.3 The absence of E-cadherin shifts the hexanematic crossover towards small length scales

As we anticipated in the Introduction, the 6-fold symmetry characterizing the structure of the cellular network at the length scale of individual cells propagates towards larger length scales, giving rise to hexatic order. The latter decays with distance and is eventually replaced by a similarly decaying nematic order at length scales larger than a system-dependent hexanematic crossover scale,  $R_{\times}$ . To understand how this depends upon the monolayer mechanical and biochemical properties, we coarse-grained the shape parameters,  $\gamma_2$  and  $\gamma_6$ , over a disk of radius R, thereby obtaining the scale-dependent shape parameter  $\overline{\Gamma}_p = \overline{\Gamma}_p(R)$  (Fig.S5.5C-D; see Methods for details). In our analysis, R was normalized to the mean cell-cell distance,  $R_{\rm cc}$ . We then analyzed the behavior of the difference  $\overline{\Gamma}_6 - \overline{\Gamma}_2$ 

5.2 Results 111

as a function of the coarse-graining radius and the mean cell-cell distance (Fig.5.2D-E). In this plot, positive (in red) and negative (in blue)  $\overline{\Gamma}_6 - \overline{\Gamma}_2$  values correspond respectively to regimes where hexatic order overweights nematic order and vice versa, whereas the white dots mark the hexanematic crossover, where  $\overline{\Gamma}_6 = \overline{\Gamma}_2$ .

In both MDCK WT (Fig.5.2D) and E-cad KO cells (Fig.5.2E), the hexanematic crossover shifted toward smaller and smaller scales upon increasing the cell-cell distance, indicating an increase in the range of hexatic order with the monolayer density. To further highlight this trend, in Fig.5.2F we plotted the normalized crossover scale  $R_{\times}/R_{\rm cc}$  for each mean cell-cell distance interval. In both cell lines,  $R_{\times}/R_{\rm cc}$  decreases approximately linearly with the monolayer density, but with significantly different rate. Specifically, at any given monolayer density, the length scale at which the hexatic order prevailed was more significantly reduced for MDCK E-cad KO cells in comparison to MDCK WT cells. It is interesting to note that both cell lines could be distinguished more clearly by the relationship between the hexanematic crossover scale and the cell-cell distance (Fig.5.2F), rather than the cell shape index (Fig.5.1D).

Taken together, our results indicate that the range of hexatic order is larger in MDCK WT cells compared to MDCK E-cad KO cells and increases with the monolayer density. Interestingly, we found that the hexanematic crossover scale provides what appears to be a robust indicator to distinguish the two cell lines.

# 5.2.4 Multiscale hexanematic order strengthen with the monolayer density

As in molecular liquid crystals, orientational order can be locally disrupted by topological defects, point-like singularities where the cells' local orientation is undefined. In multicellular systems, topological defects are believed to serve various kind of biological functionalities, from driving collective motion at length scales significantly larger than that of individual cells (14, 24), to facilitate the extrusion of apoptotic cells (15), and the development of sharp features, such as tentacles and protrusions (26, 38).

To shed light on the occurrence of topological defects in our cell layers, we computed the nematic and hexatic orientation fields of MDCK WT and E-cad KO cells and determined the location of the corresponding elementary defects (see Methods for details about the defect tracking method). For each cell-cell distance interval and coarse-graining radius, we then computed the corresponding defect density, defined as the number of defects per 100 cells in a monolayer, independently of the cell size. This

analysis is shown in Figs.5.3A and 5.3B, where the density of nematic defects in MDCK WT and E-cad KO cells, respectively, is plotted against the coarse-graining radius and the mean cell-cell distance. Because the smoothing of the orientation field progressively neutralizes pairs of defects and anti-defects, the overall defect density naturally decreases upon coarse-graining (Fig.S5.6A-B). Surprisingly, however, the defect density appeared unaffected by the cell-cell distance (Fig.S5.6C-D for hexatic). In other words, the same number of cells features the same number of defects, independently of their density.

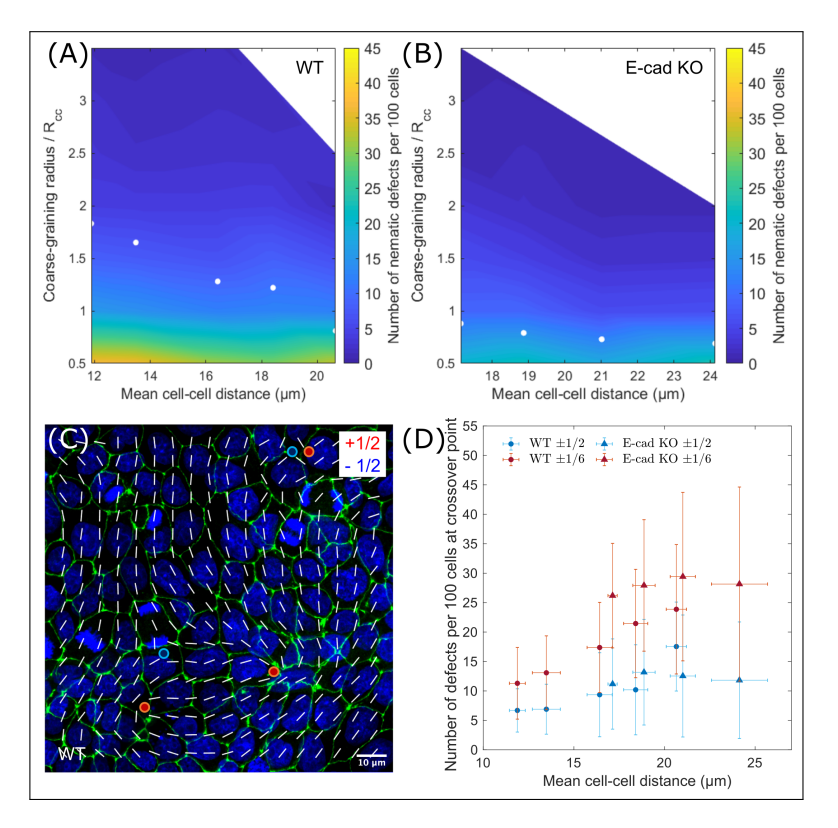


Figure 5.3: With equal hexatic and nematic order, the defect density per cell depends on the monolayer density. (A,B), The nematic defect density, defined by the number of defects per 100 cells, as a function of the coarse-graining radius and the mean cell-cell distance for MDCK-II WT and E-cad KO cells, respectively. The number of nematic defects was found to be independent of the cell density. At the hexanematic crossover, here marked by white dots, the number of defects increases with increasing mean cell-cell distance. (C), A smooth nematic director field at the hexanematic crossover with defects of charge  $\pm 1/2$  (green, ZO-1 and blue, nuclei). (D), The number of nematic and hexatic defects formed by MDCK-II WT and E-cad KO cells versus the mean cell-cell distance. Error bars represent the standard deviation.

5.2 Results 113

Since nematic and hexatic order occurs in epithelial layers at different length scales, we next investigated how the abundance of nematic and hexatic defects at the crossover scale, where both types of orientational order are simultaneously present. The abundance is shown in Fig.5.3A-B, where the white dots mark the location of the hexanematic crossover for increasing cell-cell distance. Upon computing the number of defects at the crossover scale (Fig.5.3D), we then found that for MDCK WT cells, the nematic and hexatic defects are more abundant in loosely packed monolayers (large cell-cell distance) (Tab.S5.2). Consistently with the results summarized in the previous sections, this trend was more significant in MDCK WT than in MDCK E-cad KO cells (Tab.S5.2), consistent with the observation that varying the density of MDCK E-cad KO cells has a limited effect on the hexanematic crossover (Fig.5.2F).

In conclusion, the defect density, when analyzed at the relevant crossover length scale, was lower for compact monolayers, increasing with decreasing cell density. Given this finding was observed for both shape parameter suggests that both the nematic and the hexatic order together control the collective organization of cells in generating topological defects.

# 5.2.5 Lower substrate stiffnesses reinforce the length scale of the hexatic order driven by cell-matrix and cell-cell adhesions

In the analysis reported so far, we investigated how the biomechanical properties of the cells – their density and mutual adhesion – affect the hexanematic crossover. Next, we focused on the biomechanical properties of the substrate, in particular its stiffness and adhesion with the cell monolayer. To this end, we cultured both cell lines for two days on fibronectin-coated polyacrylamide (PAA) gels of varying stiffness.

On stiff glass substrates, our measurements of the shape index,  $p_0$ , (Fig.5.1E) and the shape parameters,  $\langle |\gamma_2| \rangle$  and  $\langle |\gamma_6| \rangle$ , (Fig.5.2F), revealed a dependence of the cell shape on monolayer density. The same trend was found on compliant PAA substrates, whose stiffness ranged between 25 kPa and 49 kPa, but with no evidence of a direct cross-talk between the shape of cells and the stiffness of the substrate. While plated on compliant substrates, cells systematically formed denser monolayers, as demonstrated by the probability distribution of the cell-cell distance (Fig.S5.7). We then asked whether this change in the monolayer density affected the shape index of cells. For that, we grouped monolayers in the six cell-cell distance intervals (D1-D6; Fig.S5.7B-C), as above. The shape index of MDCK WT and E-cad KO cells increased with increasing cell-cell distance. How-

ever, most of the density intervals showed no significant indication for a stiffness-dependent shape index: by comparing cells on both PAA gels and glass (Fig.5.4A; Tab.S5.3), data from MDCK WT and E-cad KO cells overlapped. Consistently with previously reported measurements on epithelial monolayers at jamming (33), our results suggest that, when the cell-cell distance intervals between 9.7  $\mu$ m and 28.5  $\mu$ m and substrate stiffness between 25 kPa and 49 kPa, the influence of the monolayer density on the shape index overweights that caused by the substrate stiffness.

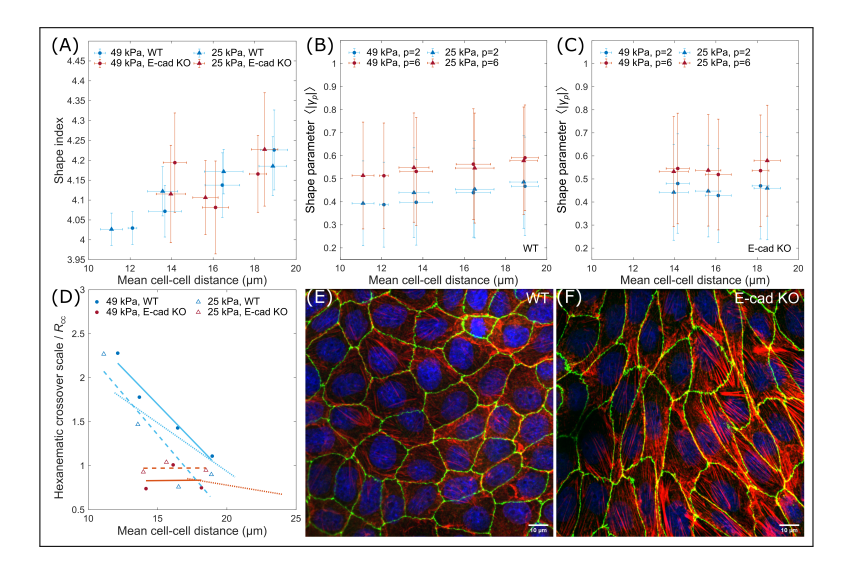


Figure 5.4: Substrate stiffness has a minor effect on the hexanematic organization. MDCK-II WT and E-cad KO cells were cultured on PAA gels with stiffness of 49 kPa and 25 kPa. (A), The mean shape index increases with the mean cell-cell distance,  $R_{cc}$ . (B,C), On single-cell scale, the mean hexatic shape parameter,  $\langle |\gamma_6| \rangle$ , is always larger compared to  $\langle |\gamma_2| \rangle$ . (D), The hexanematic crossover scale versus the mean cell-cell distance. Independent of PAA stiffness, MDCK-II WT cells exhibit a stronger dependence on monolayer density compared to E-cad KO cells, as demonstrated by the larger slope of the data. Dotted lines represent the fits of Fig.5.2F for cells on non-coated glass. (E), MDCK-II WT cells cultured on non-coated glass appear more isotropic and have a less prominent actin stress fiber network. (F), MDCK-II E-cad KO cells cultured on non-coated glass are stretched and show strong F-actin fibers (red, F-actin, green, ZO-1, and blue, nuclei). Error bars represent the standard deviation.

We next focused on the stiffness-dependence of hexanematic order across length scales. At the scale of individual cells, measurements of the 2-fold and 6-fold shape parameters,  $\langle |\gamma_2| \rangle$  and  $\langle |\gamma_6| \rangle$ , demonstrated a prevalence of 6-fold symmetry irrespective of the cell line, PAA gel stiffness, and monolayer density (Fig.5.4B-C). On the other hand, comparing the

magnitude of the coarse-grained shape parameters,  $\overline{\Gamma}_2$  and  $\overline{\Gamma}_6$ , revealed a density-dependence of the hexanematic crossover scale in MDCK WT cells, but not in MDCK E-cad KO cells (Fig.5.4D). Together with the fact that mesenchymal-like MDCK E-cad KO cells feature higher substrate adhesions and stronger actin stress fibers (Fig.5.4E-F), reduced intercellular tension, and a lower correlation length in their collective behavior (19), our results suggest that hexatic order could play a role in epithelial phenotypes regardless of the specific properties of the environment.

#### 5.3 Discussion and conclusion

In this article, we explored the multiscale structure of *in vitro* layers of MDCK-II cells, with the goal of unveiling how the mechanical and biochemical properties of the monolayers and the substrate affect the crossover between hexatic and nematic orientational order. Such a remarkable example of multiscale organization in living matter has been recently identified by means of numerical simulations and experiments (30, 31), and has been conjectured to contribute to the biophysical versatility of epithelial tissues, whose tasks range from organism-wide morphogenetic migration to collective metastatic invasion under strong confinement.

By comparing the behavior of two different cell lines – MDCK WT and the mesenchymal-like MDCK E-cad KO cells – we showed that the existence of hexatic order crucially relies on E-cadherin-mediated intercellular adhesion, whose lack on MDCK E-cad KO cells rendered the cellular shape significantly elongated, hence prone to form nematic phases. Furthermore, as the lower cell-cell adhesion increases the presence of focal adhesions and actin stress fibers (19) and these contribute to the elongation of the cell (39), we suggest that intercellular- and cell-substrate adhesions jointly control the order of cells in monolayers (see also Ref. (40)). Accordingly, cell-cell adhesion leads to a compact hexagonal shape, whereas actin stress fibers contribute to cell elongation and 2—fold symmetry.

Upon coarse-graining the 2-fold and 6-fold shape parameters, we then identified a significant dependence of the hexanematic crossover on the density of the cell monolayer as well as on the specific cell-line. In MDCK-WT cells, in particular, the hexanematic crossover occurs at larger length scales compared to MDCK E-cad KO cells and the 6-fold symmetry inherited by the shape of individual cells persists up to clusters consisting approximately 3 to 13 cells, depending on the monolayer density. Interestingly, increasing the cell density has been reported to strengthen intercellular adhesion (41, 42), while decreasing the alignment of stress fibers (41). Together with

our observations, this suggests that, in epithelial layers, multiple physical and biochemical mechanisms could conspire toward consolidating hexatic order at small length scales. On the other hand, our analysis shows that cell density is an efficient control parameter to manipulate the scale of hexanematic crossover, thus it could possibly be used by the system to switch from a hexatic- to a nematic-based migration mode.

Finally, our data provides a clear demonstration that the specific density-dependence of the hexanematic crossover is not universal, but strongly depends on the cells' molecular repertoire and could be used, in principle, to discern among phenotypes along the epithelial-mesenchymal spectrum.

#### 5.4 Materials and methods

#### Cell culture

MDCK-II WT (ATCC CCL-34) cells and MDCK-II E-cadherin KO cells were cultured in DMEM(1x)+DlutaMax-1 (2340251, Gibcon) supplemented with 10% foetal bovine serum (FBS; Life Technologies) and 1% penicillin/streptomycin (Life Technologies) at 37 °C with 5% CO<sub>2</sub>.

#### Preparation of polyacrylamide gel substrates

Polyacrylamide (PAA) gels were prepared from a stock solution of 40% acrylamide: A (1610140, Bio Rad) and 2% bis-acrylamide: B (1610142, Bio Rad) in PBS. The ratio of these components were mixed according to the PAA gel stiffness of  $25.0 \pm 2.4$  kPa (6/10 total stock volume A, 15/100 total stock volume B) and  $49 \pm 8$  kPa (6/10 total stock volume A, 28/100 total stock volume B), based on the protocol in Ref. (43). PAA gel stiffnesses were measured using indentation-type atomic force microscopy (Chiaro, Optics11 Life) and interpreted based on the Hertz model. The final PAA solution contained 50/100 total volume stock solution, 5/1000 total volume 10% ammonium persulfate (A3678-25G, Sigma Aldrich) and 15/10,000 total volume TEMED (17919, Thermo Scientific) in PBS. Glass coverslips were plasma activated and incubated with 20 µg ml<sup>-1</sup> fibronectin (FC010-10MG, Sigma-Aldrich) for 2 h. After incubation, coverslips were rinsed in water to remove excess protein. Simultaneously, a second set of glass coverslips was silanized. Glass coverslips were plasma activated and incubated with a solution of 2% (v/v) 3-(trimethoxysilyl) propyl methacrylate (440159-500ML, Sigma Aldrich) and 1% (v/v) acetic acid (20104.298, VWR Chemicals) in absolute ethanol for 10 min. After rinsing with 96% ethanol, silanized coverslips were heated at 120 °C for 1 h. PAA gels were sandwiched between the fibronectin-coated glass coverslip and silanized coverslip for 20 min. After polymerization, coverslips were separated and samples were kept in water until cell seeding.

#### **Immunostaining**

Cells on non-coated coverslips and PAA gels were cultured for three days and two days, respectively, reaching confluence after one to two days. After cell fixation with 4% paraformaldehyde (43368; Alfa Aesar) for 15 min, cells were permeabilized with 0.5% Triton-X 100 for 10 min, blocked with 1% BSA in PBS for 1 h. ZO-1 was visualized with anti-ZO-1 rat monoclonal antibody (1:200 ratio; clone R40.76, MilliporeSigma) followed by staining with Alexa Fluor 488 goat anti-rat (1:200 ratio; A11006, LifeTechnology), F-actin with Alexa Fluor 568 Phalloidin (1:200 ratio; A12380, Invitrogen), and DNA with Hoechst (1:10,000 ratio; 33342 Thermo Fischer).

#### **Imaging**

Before imaging, samples were mounted on ProLong (P36962, Invitrogen). Imaging was performed on a microscope setup based on an inverted Axio Observer.Z1 microscope (Zeiss), a Yokogawa CSU-X1 spinning disk, and a 2 ORCA Fusion camera (Hamamatsu). ZEN 2 acquisition software was used for setup-control and data acquisition. Illumination was performed using different lasers (405 nm, 488 nm, 561 nm). Cells were inspected with a  $63 \times 1.4$  oil immersion objective (Zeiss). Images were taken in z-stack focal-planes with distances of 500 nm for a maximal intensity projection.

#### Cell shape analysis

Segmentation. Cell boundaries of confluent monolayers were analyzed using a maximum intensity projection of z—stack images. Cell segmentation and vertex analysis were performed using custom MATLAB scripts (Mathworks, MATLAB R2018a). In short, the ZO-1 signal was thresholded and skeletonized. Branching points shared by at least three cells were identified as vertices. The number of vertices surrounding a cell corresponds to the number of nearest neighbors. To obtain the polygon structure of each cell, vertices were connected by straight lines.

Shape parameter. The shape parameter is defined as a the complex function (30):

$$\gamma_p = \frac{1}{\Delta_p} \sum_{k=1}^{V} |\boldsymbol{r}_c - \boldsymbol{r}_k|^p e^{ip\phi_k} , \qquad (5.1)$$

where  $r_k$  is the position of the k-th vertex of the polygon tracing the con-

tour of a cell positioned with it's center of mass at,  $\mathbf{r}_c = 1/V \sum_{k=1}^{N} \mathbf{r}_k$ . Further,  $\Delta_p = \sum_{k=1}^{V} |\mathbf{r}_c - \mathbf{r}_k|^p$  and  $\phi_k = \arctan(y_k/x_k)$  the angular coordinate of the k-th vertex. We here focused on the 2-fold parameter,  $\gamma_2$ , describing the nematic order, and on the 6-fold parameter,  $\gamma_6$ , describing the hexatic order.

Ensemble average. The ensemble average  $\langle |\gamma_p| \rangle$  was obtained by averaging the magnitude of the complex function  $\gamma_p$  over the entire ensemble of cells,  $N_{\text{cells}}$ , analyzed in a given dataset and density interval. That is

$$\langle |\gamma_p| \rangle = \frac{1}{N_{\text{cells}}} \sum_{c=1}^{N_{\text{cells}}} |\gamma_p|_c .$$
 (5.2)

Coarse-graining. Coarse-graining of the shape-parameter fields at any location, r, and length scale, R, was performed by averaging the complex values of  $\gamma_p$  of Eq.(5.1) over all  $N_R$  cells, for which the center-of-mass was located inside a disk of radius R:

$$\Gamma_p(R, \mathbf{r}) = \frac{1}{N_R} \sum_{k=1}^{N_R} \gamma_{p,k}.$$

$$(5.3)$$

Images were constructed on a regular cartesian grid,  $r_n$ , of lattice spacing of half the mean cell-cell distance,  $R_{\rm cc}/2$ , within a field of view of 124 × 124 µm. Coarse-graining was performed for coarse-graining radii of integer multiples of half the mean cell-cell distance,  $R = m \times R_{\rm cc}/2$ , and at all lattice positions,  $r_n$ . The average coarse-grained magnitude of the shape parameter,  $\overline{\Gamma}_p$  (see e.g. Fig.S5.5C-D), was subsequently determined by averaging over all  $r_n$  positions, N, of the constructed coarse-grained shape parameter images as a function of R:

$$\overline{\Gamma}_p(R) = \frac{1}{N} \sum_{n=1}^{N} |\Gamma(R, \boldsymbol{r}_n)|.$$
 (5.4)

#### Topological Defects

Topological defects were identified by computing the winding number (44) around a unit cell of a superimposed cartesian grid. The winding number, s, was calculated as

$$s = \frac{1}{2\pi} \sum_{k=1}^{V} (\theta_{k+1} - \theta_k) \bmod \left(\frac{2\pi}{p}\right) , \qquad (5.5)$$

where  $\theta$  is the p-fold orientation of the polygon defined from the phase of the shape parameter  $\Gamma_p$ : i.e.  $\theta_p = (1/p) \arctan[\operatorname{Im}(\Gamma_p)/\operatorname{Re}(\Gamma_p)]$ .

#### **Statistics**

The number of experiments performed and number of images taken are summarized in Tab.S5.1. All data sets are of non-normal distribution. P-values between two groups were calculated using the two-sided Wilcoxon rank sum test in MATLAB. Comparisons between more than two groups were performed using Dunn's test of multiple comparisons after Kruskal–Wallis significance test in R. Data set significance was defined as of  $p \le 0.05$  (\*); p < 0.01 (\*\*\*); p < 0.001 (\*\*\*); p < 0.001 (\*\*\*); p > 0.05 (ns).

#### Acknowledgements

J.E. acknowledges the EMBO Scientific Exchange Grant (STF reference number: 9076) for financial support to the research visit to Benoît Ladoux's lab at the Institut Jacques Monod in Paris. This work is part of the research program 'The Active Matter Physics of Collective Metastasis', project number Science-XL 2019.022, which is financed by the Dutch Research Council (NWO). J.E. acknowledges Wang Xi for the stiffness measurement of the PAA gels, and Josep-Maria Armengol-Collado for the discussions on the theoretical aspects of this work.

#### Author contributions

J.E. conducted and coordinated the research, performed the experiments, and analyzed the data. T.S., B.L. and L.G. supervised the project. All authors conceptualized the results, wrote the manuscript, and agreed on its current version.

#### 5.5 Supplementary

#### **Tables**

		experiments	samples	images	total numner of cells
	glass	3	16	226	11987
WT	25  kPa	5	8	95	9391
	$49~\mathrm{kPa}$	3	6	75	4485
	glass	3	18	216	6941
E-cad KO	25  kPa	3	7	81	5412
	$49~\mathrm{kPa}$	3	11	144	8348

Table S5.1: Number of experiments, samples, imaged monolayers, and analyzed MDCK-II WT and E-cad KO cells on non-coated glass, 25 kPa, and 49 kPa.

WT	nematic			hexatic				
p-value	D1	D2	D3	D4	D1	D2	D3	D4
D2	0.50				0.23			
D3	0.17	0.07			0.0037	0.0016		
D4	0.10	0.028	0.23		0.0001	< 0.0001	0.008	
D5	0.0024	0.0005	0.0032	0.010	0.0007	0.0010	0.041	0.26
E-cad KO	nematic				hexati	c		
p-value	D3	D4	D5		D3	D4	D5	
D4	0.20				0.27			
D5	0.33	0.24			0.22	0.34		
D6	0.39	0.23	0.43		0.39	0.35	0.27	

**Table S5.2:** Comparison of the defect densities at the crossover scale for MDCK-II WT and E-cad KO cells on glass. Cells were classified into groups D1-D6 according to their cell-cell distance. Statistical test: Dunn's test of multiple comparisons after a significant Kruskal-Wallis test. p-value > 0.05, results are not significantly different.

		WT		E-cad KO	
p-value		glass	25  kPa	glass	$25~\mathrm{kPa}$
25 kPa	D1	0.42			
	D2	0.012			
	D3	0.007		0.28	
	D4	0.012		0.19	
	D5	0.10			
49 kPa	D1	0.49	0.43		
	D2	0.07	0.18		0.005
	D3	0.0015	0.26	0.13	0.29
	D4	0.0001	0.26	0.31	0.38
	D5	0.14	0.37		

**Table S5.3:** Comparison of the shape index for MDCK-II WT and E-cad KO cells on glass, 25 kPa and 49 kPa. Cells were classified into groups D1-D6 according to their cell-cell distance. Statistical test: Dunn's test of multiple comparisons after a significant Kruskal-Wallis test. p-value > 0.05, results are not significantly different.

# CHAPTER 5

#### **Figures**

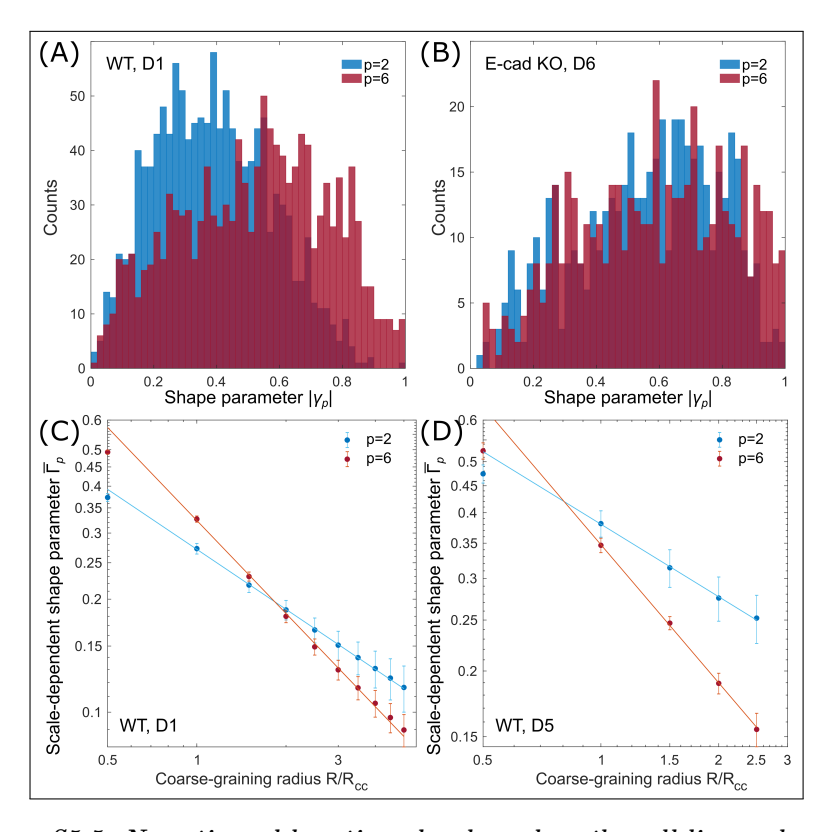


Figure S5.5: Nematic and hexatic order depend on the cell line and monolayer density. (A,B), The magnitude of the cell's shape parameters of all analyzed cells within a defined density interval, as shown in Fig.3.1D. (A), For MDCK-II WT cells at a high density, D1, the distribution of the hexatic shape parameter,  $\langle |\gamma_6| \rangle$ , is biased towards larger values compared to the nematic shape parameter,  $\langle |\gamma_2| \rangle$ , indicating a prevalence of hexatic order at small scale. (B), Conversely, at low monolayer densities, D6, the two distributions overlap. (C,D), Scale-dependent nematic and hexatic shape parameters,  $\overline{\Gamma}_2$  and  $\overline{\Gamma}_6$ , of MDCK-II WT cells associated with the same density interval D1 and D5, respectively.  $\overline{\Gamma}_2$  and  $\overline{\Gamma}_6$  decrease as power laws with the coarse-graining radius,  $R/R_{cc}$ :  $\overline{\Gamma}_p \sim (R/R_{cc})^{-\eta_p/2}$ , with  $\eta_p$  a non-universal exponent. The intersection of the fitting lines identify the hexanematic crossover scale,  $R_{\times}$ . In panel (C), the crossover scale is  $R/R_{cc} = 1.83$  for cells in the highest density interval, D1, and shifts to a smaller interval at lower monolayer densities, D5, of  $R/R_{cc} = 0.81$  (D). A combined plot is shown in Fig.5.2D-F. Error bars represent the standard error of mean.

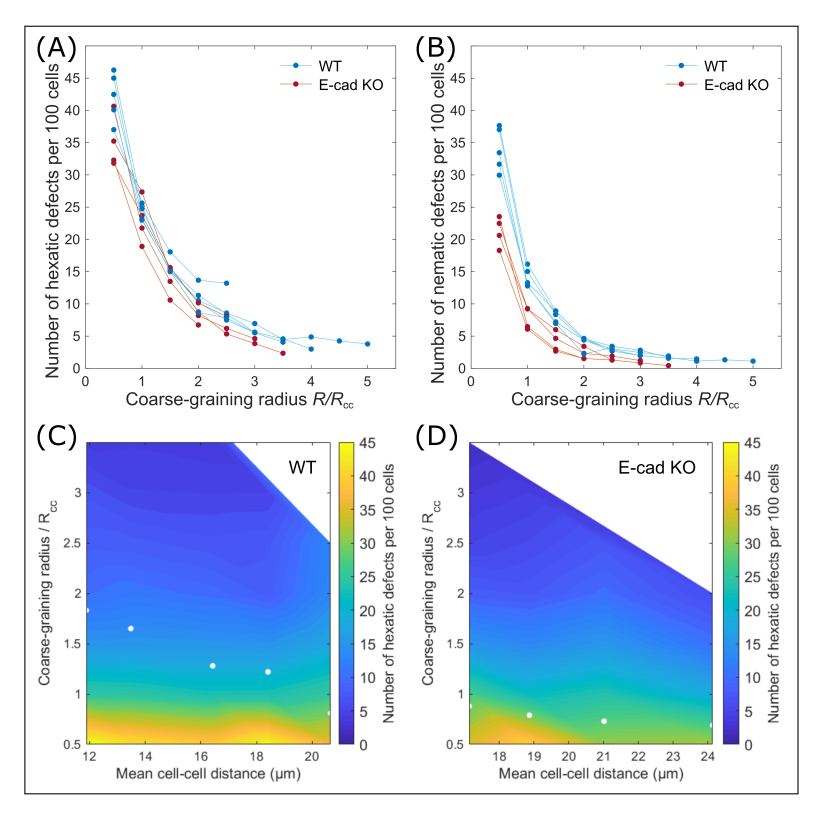


Figure S5.6: The defect density depends on the coarse-grained orientation field. (A,B), The number of nematic and hexatic defects per 100 cells decreases with increasing coarse-graining radius for MDCK-II WT and E-cad KO cells. (C,D), The number of hexatic defects per 100 cells as a function of the coarse-graining radius and the mean cell-cell distance for both MDCK-II cell lines.

123

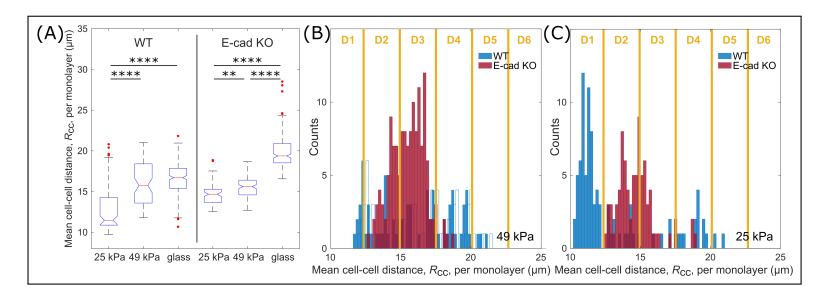


Figure S5.7: The mean cell-cell distance increases with increasing substrate stiffness. (A), Mean cell-cell distance of nearest neighbors for MDCK-II WT and E-cad KO cells cultured on non-coated glass, and PAA gels with a stiffness of 25 kPa and 49 kPa. Cells tend to be more compact on softer substrates. (B,C), Distributions of mean cell-cell distance of both cell lines cultured on 49 kPa and 25 kPa, respectively. Each bin-width is equal to 0.2  $\mu$ m. For density dependent measurements, cells were grouped in six intervals, D1-D6, of 2.6  $\mu$ m each (49 kPa:  $N_{WT}=75$  and  $N_{KO}=144$ , 25 kPa:  $N_{KO}=81$  from three independent experiments; 25 kPa:  $N_{WT}=95$  from five independent experiments). Comparisons were performed using Dunn's test of multiple comparisons after a significant Kruskal–Wallis test: \*\* p < 0.001; \*\*\*\* p < 0.0001.

- Lecuit, T., and Lenne, P.-F. (2007). Cell surface mechanics and the control of cell shape, tissue patterns and morphogenesis. *Nature Reviews Molecular Cell Biology* 8, 633–644.
- (2) Alt, S., Ganguly, P., and Salbreux, G. (2017). Vertex models: from cell mechanics to tissue morphogenesis. Philosophical transactions of the Royal Society of London. Series B, Biological sciences 372, 20150520.
- (3) Guillot, C., and Lecuit, T. (2013). Mechanics of Epithelial Tissue Homeostasis and Morphogenesis. Science 340, 1185–1189.
- (4) Bailles, A., Collinet, C., Philippe, J.-M., Lenne, P.-F., Munro, E., and Lecuit, T. (2019). Genetic induction and mechanochemical propagation of a morphogenetic wave. *Nature* 572, 467–473.
- (5) Pérez-González, C. et al. (2021). Mechanical compartmentalization of the intestinal organoid enables crypt folding and collective cell migration. Nature Cell Biology 23, 745–757.
- (6) Bertet, C., Sulak, L., and Lecuit, T. (2004). Myosin-dependent junction remodelling controls planar cell intercalation and axis elongation. *Nature* 429, 667– 671.
- (7) Salbreux, G., Charras, G., and Paluch, E. (2012). Actin cortex mechanics and cellular morphogenesis. Trends in Cell Biology 22, 536–545.
- (8) Heisenberg, C.-P., and Bellaïche, Y. (2013). Forces in tissue morphogenesis and patterning. Cell 153, 948962.
- (9) Gupta, S., Duszyc, K., Verma, S., Budnar, S., Liang, X., Gomez, G. A., Marcq, P., Noordstra, I., and Yap, A. S. (2021). Enhanced RhoA signalling stabilizes Ecadherin in migrating epithelial monolayers. *Journal of Cell Science* 134, jcs258767.
- (10) Arslan, F. N., Eckert, J., Schmidt, T., and Heisenberg, C.-P. (2021). Holding it together: when cadherin meets cadherin. *Biophysical Journal* 120, 4182–4192.
- (11) Rauzi, M., Lenne, P.-F., and Lecuit, T. (2010). Planar polarized actomyosin contractile flows control epithelial junction remodelling. *Nature* 468, 1110–1114.
- (12) Chen, D.-Y., Crest, J., Streichan, S. J., and Bilder, D. (2019). Extracellular matrix stiffness cues junctional remodeling for 3D tissue elongation. *Nature Communications* 10, 3339.
- (13) Duclos, G., Erlenkämper, C., Joanny, J.-F., and Silberzan, P. (2017). Topological defects in confined populations of spindle-shaped cells. *Nature Physics* 13, 58–62.
- (14) Kawaguchi, K., Kageyama, R., and Sano, M. (2017). Topological defects control collective dynamics in neural progenitor cell cultures. *Nature* 545, 327–331.

(15) Saw, T. B., Doostmohammadi, A., Nier, V., Kocgozlu, L., Thampi, S., Toyama, Y., Marcq, P., Lim, C. T., Yeomans, J. M., and Ladoux, B. (2017). Topological defects in epithelia govern cell death and extrusion. *Nature* 544, 212–216.

- (16) Turiv, T., Krieger, J., Babakhanova, G., Yu, H., Shiyanovskii, S. V., Wei, Q.-H., Kim, M.-H., and Lavrentovich, O. D. (2020). Topology control of human fibroblast cells monolayer by liquid crystal elastomer. Science Advances 6, eaaz6485.
- (17) Guillamat, P., Blanch-Mercader, C., Pernollet, G., Kruse, K., and Roux, A. (2022). Integer topological defects organize stresses driving tissue morphogenesis. Nature Materials 21, 588–597.
- (18) Maroudas-Sacks, Y., Garion, L., Shani-Zerbib, L., Livshits, A., Braun, E., and Keren, K. (2021). Topological defects in the nematic order of actin fibres as organization centres of Hydra morphogenesis. *Nature Physics* 17, 251–259.
- (19) Balasubramaniam, L., Doostmohammadi, A., Saw, T. B., Narayana, G. H. N. S., Mueller, R., Dang, T., Thomas, M., Gupta, S., Sonam, S., Yap, A. S., Toyama, Y., Mège, R.-M., Yeomans, J. M., and Ladoux, B. (2021). Investigating the nature of active forces in tissues reveals how contractile cells can form extensile monolayers. *Nature Materials* 20, 1156–1166.
- (20) Cetera, M., Ramirez-San Juan, G. R., Oakes, P. W., Lewellyn, L., Fairchild, M. J., Tanentzapf, G., Gardel, M. L., and Horne-Badovinac, S. (2014). Epithelial rotation promotes the global alignment of contractile actin bundles during Drosophila egg chamber elongation. *Nature Communications* 5, 5511.
- (21) Jain, S., Cachoux, V. M. L., Narayana, G. H. N. S., de Beco, S., D'Alessandro, J., Cellerin, V., Chen, T., Heuzé, M. L., Marcq, P., Mège, R.-M., Kabla, A. J., Lim, C. T., and Ladoux, B. (2020). The role of single-cell mechanical behaviour and polarity in driving collective cell migration. *Nature Physics* 16, 802–809.
- (22) Duclos, G., Garcia, S., Yevick, H. G., and Silberzan, P. (2014). Perfect nematic order in confined monolayers of spindle-shaped cells. Soft Matter 10, 2346–2353.
- (23) Saw, T. B., Xi, W., Ladoux, B., and Lim, C. T. (2018). Biological Tissues as Active Nematic Liquid Crystals. Advanced Materials 30.
- (24) Balasubramaniam, L., Mège, R.-M., and Ladoux, B. (2022). Active nematics across scales from cytoskeleton organization to tissue morphogenesis. *Current Opinion in Genetics & Development* 73, 101897.
- (25) Streichan, S. J., Lefebvre, M. F., Noll, N., Wieschaus, E. F., and Shraiman, B. I. (2018). Global morphogenetic flow is accurately predicted by the spatial distribution of myosin motors. *Elife* 7, e27454.
- (26) Hoffmann, L. A., Carenza, L. N., Eckert, J., and Giomi, L. (2022). Theory of defect-mediated morphogenesis. Science Advances 8, eabk2712.
- (27) Li, Y.-W., and Ciamarra, M. P. (2018). Role of cell deformability in the twodimensional melting of biological tissues. *Phys. Rev. Materials* 2, 045602.
- (28) Durand, M., and Heu, J. (2019). Thermally driven order-disorder transition in two-dimensional soft cellular systems. *Phys. Rev. Lett.* 123, 188001.
- (29) Pasupalak, A., Yan-Wei, L., Ni, R., and Pica Ciamarra, M. (2020). Hexatic phase in a model of active biological tissues. Soft Matter 16, 3914–3920.
- (30) Armengol-Collado, J.-M., Carenza, L. N., Eckert, J., Krommydas, D., and Giomi, L. (2022). Epithelia are multiscale active liquid crystals. arXiv:2202.00668.

(31) Armengol-Collado, J.-M., Carenza, L. N., and Giomi, L. (2022). Hydrodynamics and multiscale order in confluent epithelia. arXiv:2202.00651.

- (32) Angelini, T. E., Hannezo, E., Trepat, X., Marquez, M., Fredberg, J. J., and Weitz, D. A. (2011). Glass-like dynamics of collective cell migration. *Proceedings of the National Academy of Sciences* 108, 4714–4719.
- (33) Devany, J., Sussman, D. M., Yamamoto, T., Manning, M. L., and Gardel, M. L. (2021). Cell cycle—dependent active stress drives epithelia remodeling. Proceedings of the National Academy of Sciences 118, e1917853118.
- (34) Farhadifar, R., Röper, J.-C., Aigouy, B., Eaton, S., and Jülicher, F. (2007). The Influence of Cell Mechanics, Cell-Cell Interactions, and Proliferation on Epithelial Packing. Current Biology 17, 2095–2104.
- (35) Bi, D., Lopez, J. H., Schwarz, J. M., and Manning, M. L. (2015). A density-independent rigidity transition in biological tissues. *Nature Physics* 11, 1074–1079.
- (36) Bi, D., Yang, X., Marchetti, M. C., and Manning, M. L. (2016). Motility-driven glass and jamming transitions in biological tissues. *Physical review. X* 6, 021011.
- (37) Park, J.-A. et al. (2015). Unjamming and cell shape in the asthmatic airway epithelium. *Nature Materials* 14, 1040–1048.
- (38) Maroudas-Sacks, Y., Garion, L., Shani-Zerbib, L., Livshits, A., Braun, E., and Keren, K. (2021). Topological defects in the nematic order of actin fibres as organization centres of Hydra morphogenesis. *Nature Physics* 17, 251–259.
- (39) Schakenraad, K., Ernst, J., Pomp, W., Danen, E. H. J., Merks, R. M. H., Schmidt, T., and Giomi, L. (2020). Mechanical interplay between cell shape and actin cytoskeleton organization. *Soft Matter* 16, 6328–6343.
- (40) Choi, D., Gonzalez, Z., Ho, S. Y., Bermudez, A., and Lin, N. Y. (2022). Cell-cell adhesion impacts epithelia response to substrate stiffness: Morphology and gene expression. *Biophysical Journal* 121, 336–346.
- (41) Saraswathibhatla, A., and Notbohm, J. (2020). Tractions and Stress Fibers Control Cell Shape and Rearrangements in Collective Cell Migration. *Physical Review X 10*, 011016.
- (42) Vazquez, K., Saraswathibhatla, A., and Notbohm, J. (2022). Effect of substrate stiffness on friction in collective cell migration. *Scientific Reports* 12, 2474.
- (43) Plotnikov, S. V., Sabass, B., Schwarz, U. S., and Waterman, C. M. In *Quantitative Imaging in Cell Biology*, Waters, J. C., and Wittman, T., Eds.; Methods in Cell Biology, Vol. 123; Academic Press: 2014, pp 367–394.
- (44) Huterer, D., and Vachaspati, T. (2005). Distribution of singularities in the cosmic microwave background polarization. *Phys. Rev. D* 72, 043004.

# Summary

What feature do whales, snails, humans, flowers, and all other creatures have in common? We are all made up of the same building blocks called cells. For instance, trillions of cells ranging in size from tens of microns arrange themselves in a network to form the organs of the human body and the surrounding structure. They go through their own life cycle, communicate and coordinate to provide the characteristics of our individuality. Just the fact that you were able to open this book and hopefully enjoyed reading this thesis is thanks to your network of cells.

What is the mystery behind this network that makes our whole life possible with such small cells? Simply put, the cell network is not so different from our community. We still tend to distinguish humans by their gender, country of origin, or cultural background, even though we are all the same. Cells are classified into different cell types such as stem cells, skin cells, muscle cells, and lung cells based on their molecular structure and composition. Humans are in contact with each other in their daily lives, queuing at the supermarket, getting squeezed in the metro, crossing bridges with others, or just enjoying a soccer match in a large stadium. We interact with our community, but we can also enjoy our privacy and remain separate. Cells basically do the same thing. They are connected to each other to form small structures, monolayers, and tissues such as vesicles and organs. Cells also interact with their surrounding microenvironment and migrate through it individually or in small colonies, as is the case with cancer metastases. We see that environmental perception, communication, coordination, and collectivity play a major role at different scales. This thesis covered such topics in the fields of cell biology, biological and soft matter physics, and combined experimental observations with theoretical descriptions.

The emergence and role of interactions between cells have been discussed over the past decades and remain an urgent topic of daily research across various research disciplines. While physicists describe cell-cell adhesion in terms of tension, forces, pressure, and stress at the cell interface, biologists study the molecular composition and mechanisms within the cells

130 Summary

involved. Some molecules across the membrane connect cells to each other or the cell to the microenvironment, others form a skeletal structure, the cell's cytoskeleton, and yet others combine all internal parts. In Chapter 1, we have reviewed this topic and introduced a definition of cell-cell adhesion that provides a common base for understanding the biological and physical principles of cell-cell adhesion. When cells are in contact with each another, they experience pressure and tension of their neighboring cells, just like humans squeezed on a metro train, bumping into each other at every single turn. Cells are able to respond to forces of their microenvironment and neighboring cells. Any difference in tension experienced starts a signaling pathway within the cell. Molecules are recruited and rearranged throughout the cell to support stability at the cell-cell adhesion interface, for example, and they can lead to changes in the cytoskeleton, resulting in changes in the shape of the cells. In turn, to each action of a cell there is always opposed an equal reaction of other cells. From external point of view, cell-cell adhesion is also associated with shape changes, coordination, and collective behavior of cells.

In Chapter 2, we have studied the interaction of individual cells with their microenvironment. The internal structure of individual cells differs from that of connected cells. Individual cells adhere to the substrate solely with the support of adhesion molecules. Adhesion molecules, in turn, connect to the cytoskeleton that supports the cell's shape. This cytoskeleton is able of contracting, creating a pull on the substrate and allowing the whole cell to move, similar to the muscle contraction of a snail. Contraction, and thus the traction force applied, is a property of cells. For example, muscle cells generate high forces to pump blood through the veins. Here, we compared two different cell types based on their traction forces and studied how their shape is related to this. To measure traction forces of cells, we used a specific tool called the micropillar array. Micropillar arrays consist of hundreds of tiny elastic beams, much smaller than the cell. When a cell adheres to a bed of micropillars and applies a force, the beams bend. This bending can be measured with microscopes and software that converts the beam's deflection into a force. In our experiment, we used endothelial and fibroblast cells. Endothelial cells form tightly connective two-dimensional tissues that surround blood vessels. Fibroblasts, in turn, are motile, maintain the integrity of tissues, and are thus involved in tissue repair. In our study, we showed that endothelial cells apply half the traction forces of fibroblasts on their surroundings. This result displays the function of each cell type. Since the cell-cell adhesion is pronounced in endothelial cells for tissue formation, the contraction of the cytoskeleton is stronger at the cell-cell interface than at the cell-substrate adhesion. Fibroblasts require stronger cell-substrate interactions to remodel the cell's environment. We also have shown that the traction force distribution of endothelial cells is broader and correlate with their round morphology, whereas fibroblasts are more elongated and the traction forces are more localized. We speculate that the correlation of the force distribution-pattern with cell morphology could lead to guide the directionality of cell movements and collective behavior, an insight that may be important for the mechanism of cell and tissue migration.

During dynamic processes such as collective cell migration, cells experience rapid changes of tension at their cell-cell interface. Cell-cell adhesions must be formed to resist detachment forces and maintain tissue integrity. The following questions arise here: what is the maximum force that can be applied to break the cell-cell adhesion, and can it be measured? To answer these questions, we have developed the micropillar array technology further to exactly measure cell-cell detachment forces. In Chapter 3, we introduced our novel technology, the Cell-Cell Separation Device or CC-SD for short. The CC-SD consists of closely spaced micropillar array blocks to which cells can adhere and connect across the gap. Ideally, two cells in a doublet configuration attach to the micropillars. Bending of micropillars is again used for cell traction force measurements. The applied forces surrounding the cell doublet should balance to a mechanical equilibrium. When you hold hands with another person, you both feel the tension in your arms, standing steady on your feet without moving. This tension between cells can be measured using micropillars. We have shown that the cell-cell adhesion force in such steady conditions is proportional to the total applied traction force acting on the pillars. In order to apply a strain to the cell-cell contact, we connected the blocks to a thin layer underneath. Stretching the layer separates the blocks and increases tension on the cellcell adhesion. The tension is mainly localized at the cell-cell contact and less below the cell due to the blocks that prevent deformation of the pillar fields. In our example, when the distance to the other person in front of you increases, the tension in your arms increases too. You also feel more tension in your legs and exert more resistance on the ground. The increase in substrate forces applied by cells can be measured by the CC-SD and provides information about the increased tension between cells and even allows the contact to break. Our novel designed CC-SD opens up possibilities for analyzing cell-cell detachment forces and sheds light on the robustness of cell-cell adhesions during dynamic processes in tissue development.

As we discussed in **Chapter 1**, cells in tissues undergo dynamic pro-

132 Summary

cesses involving cell-substrate and cell-cell adhesions. The pressure and tension from neighboring cells lead to changes in the shape of individual cells and even drive collective migrations within a tissue. In a tightly packed metro train, when you are just close to the door, the train stops, and the door suddenly opens, sometimes you have no chance to stay inside the train. You are forced to follow the stream of the other passengers in a directed way. The collective behavior and directionality of cells are the current state of research and can be found in a wide variety of systems such as wound healing, cancer metastasis, and embryonic development. To explain and study the collectivity of cells during migration, scientists have mainly used a so-called nematic symmetry derived from liquid crystals, i.e. rod-like structures, in soft matter physics. Nematics describes the orientation and elongation of cells on single-cell scale and their alignment on global scale. The overall alignment can be summarized by a single value, the nematic order parameter, that represents how collectively oriented cells are. However, if you take a closer look at a tissue, you will notice that cells are not always elongated. Cells can have a rounded shape and line up with their neighbors in a hexagonal pattern where the distances to all six neighbors are nearly equal. Describing these six preferred directions requires a different kind of symmetry, namely hexatic symmetry. The description of cells in monolayers based on nematic and hexatic order was the subject in Chapter 4. Combining experimental observations with numerical simulations, we compared the hexatic and nematic order of cell systems across different length scales. Starting with the single cell level, we showed that cells have indeed a dominant hexatic order. They are more hexagonal-roundish rather than elongated. When we considered the nearest neighbors of the cells, we saw that the cell system switched from hexatic to nematic symmetry as we considered more and more neighboring cells. The results showed that our novel approach identified the coexistence of hexatic and nematic symmetry at different length scales. Knowing the correct symmetry of the system opens the possibilities to study the hierarchical structure of cells in tissues, and to find out how cells coordinate and achieve multicellular organization.

Multicellular organization is important for developmental processes and occurs in cancer metastases. We have already shown in **Chapter 2** that different cell types have different morphological properties due to their traction forces and cell-cell adhesion. The main type of tissue in our human body, covering all surfaces including organs, is epithelial tissue. Epithelia are known for their strong cell-cell adhesion. Under certain circumstances, epithelial cells can lose their cell-cell adhesion, develop stronger adhesions to the substrate, gain mobility, and even become individual. This process

is known as epithelial-to-mesenchymal transition, in which cells transform from epithelial tissue cells to invasive and active mesenchymal cells involved in wound healing, fibrosis, and cancer progression. During these processes, the entire multicellular organization changes. In Chapter 4, we have shown that the symmetry of tissues differs across different length scales and is possibly linked to multicellular organization. How does the symmetry change when cells change their adhesion properties and tissues their cellular density? We addressed these questions in **Chapter 5** by comparing epithelial cells with mesenchymal-like cells in which, unlike epithelial cells, only a specific type of cell-cell adhesion molecule has been removed. Removal of adhesion molecules results in a strong formation of the cytoskeleton to increase the cellular stability by the substrate. To follow up on our example from above, when you are on the packed metro train, you keep the balance through the other passengers. There is no space to fall down. However, when there are fewer passengers, your legs must take over and coordinate your balance. In our experiments, we showed that, indeed, mesenchymal-like cells are larger and more spread due to their highly developed cytoskeleton network. When we looked at the symmetry of individual cells in tissues, we found that independent of the existence of the certain type of cell-cell adhesion molecule, and no matter how much they were squeezed, cells always have a dominant hexatic order. They prefer to be hexagonal-roundish rather than elongated and nematic. When considering, again, more and more neighboring cells, the monolayer, again, has a higher and dominant nematic symmetry. This crossover, i.e. the number of cells considered, from hexatic to nematic does depend on the cell-cell adhesion. Removing cell-cell adhesion molecules causes a dominant nematic organization in multicellular systems on global scale. Cells with strong cell-cell contacts keep their hexatic organization for slightly longer length scales. This is also true for monolayers with higher cell density. These results indicate that the interplay between cell-substrate and cell-cell adhesion controls the length scale of the hexatic symmetry.

However, many questions remain. Is it possible to study optical features of cells, such as tissue symmetry, collective migration, and changes in cell shape, and use this information to identify intercellular mechanisms? Can we study the 'symptoms' of cells to get the correct 'diagnosis' of disordered tissue organization? Can we identify a pattern and even predict collective cell behavior and thus developmental processes?

Questions upon questions. If you have not stopped reading or fallen asleep, I hope I have convinced you that this thesis opens a chapter to

134 Summary

answer these questions. We have shown that cell mechanics and geometric properties such as cell and tissue symmetry provide information about intercellular processes and cell-cell interactions at the molecular scale. Combining the expertise from different research disciplines is essential for gapless research and opens up possibilities to put all result-pieces of the research puzzle together to complete the big picture.

 $Julia\ Eckert$ 

Welke eigenschap hebben walvissen, slakken, mensen, bloemen en alle andere levende wezens gemeen? We zijn allemaal opgebouwd uit dezelfde bouwstenen, cellen genaamd. Bijvoorbeeld, biljoenen cellen, variërend in grootte van tientallen microns, rangschikken zichzelf in een netwerk om organen van het menselijk lichaam en de omringende structuur te vormen. Ze doorlopen hun eigen levenscyclus, communiceren en coördineren om de kenmerken van onze individualiteit te bieden. Alleen al het feit dat je dit boek hebt kunnen openen en hopelijk genoten hebt van het lezen van dit proefschrift, is te danken aan je netwerk van cellen.

Wat is het mysterie achter dit netwerk dat ons hele leven mogelijk maakt met zulke kleine cellen? Simpel gezegd, het netwerk van cellen verschilt niet zo veel van onze gemeenschap. We hebben nog steeds de neiging om mensen te specificeren op basis van hun geslacht, land van herkomst of culturele achtergrond, ook al zijn we allemaal hetzelfde. Cellen worden onderverdeeld in verschillende celtypen, zoals stamcellen, huidcellen, spiercellen en longcellen op basis van hun moleculaire structuur en samenstelling. Mensen staan in het dagelijks leven met elkaar in contact, staan in de rij bij de supermarkt, worden geperst in de metro, steken bruggen over met anderen of genieten gewoon van een voetbalwedstrijd in een groot stadion. We hebben interactie met onze gemeenschap, maar we kunnen ook genieten van onze privacy en gescheiden blijven. Cellen doen in principe hetzelfde. Ze zijn met elkaar verbonden om kleine structuren, monolagen en weefsels zoals blaasjes en organen te bouwen. Cellen interageren ook met hun omringende microomgeving en migreren er individueel of in kleine kolonies doorheen, zoals het geval is bij kankermetastasen. We zien dat beleving van de omgeving, communicatie, coördinatie en collectiviteit een grote rol spelen op verschillende schalen. Dit proefschrift behandelde dergelijke onderwerpen op het gebied van celbiologie, biologische en zachte materie fysica en combineerde experimentele observaties met theoretische beschrijvingen.

Het ontstaan en de rol van interacties tussen cellen is de afgelopen decennia besproken en is nog steeds een urgent onderwerp in het dagelijkse onderzoek in verschillende onderzoeksdisciplines. Terwijl natuurkundigen

cel-cel adhesie beschrijven in termen van spanning, krachten, druk en stress op het celinterface, bestuderen biologen de moleculaire samenstelling en mechanismen in de betrokken cellen. Sommige moleculen over het membraan verbinden cellen met elkaar of de cel met de micro-omgeving, andere vormen een skeletstructuur, het cytoskelet van de cel, en weer andere combineren alle interne onderdelen. In **Hoofdstuk 1** hebben we dit onderwerp besproken en een definitie van cel-cel adhesie geïntroduceerd met een gemeenschappelijke basis voor het begrijpen van de biologische en fysische principes van cel-cel adhesie. Wanneer cellen met elkaar in contact zijn, ervaren ze druk en spanning van hun aangrenzende cellen, zoals samengeperste mensen in een metro, die bij elke bocht tegen elkaar botsen. Cellen kunnen reageren op krachten uit hun micro-omgeving en naburige cellen. Elk verschil in spanning dat wordt ervaren, begint een signaalroute in de cel. Moleculen worden gerekruteerd en herschikt door de cel om bijvoorbeeld de stabiliteit op de cel-cel adhesie-interface te ondersteunen, en ze kunnen leiden tot veranderingen in het cytoskelet, wat resulteert in vormveranderingen van cellen. Op zijn beurt staat elke actie van een cel tegenover een reactie van andere cellen. Vanuit extern oogpunt wordt cel-cel adhesie ook geassocieerd met vormveranderingen, coördinatie en collectief gedrag van cellen.

In **Hoofdstuk 2** hebben we de reactie van individuele cellen op hun micro-omgeving bestudeerd. De interne structuur van individuele cellen verschilt van die van verbonden cellen. Individuele cellen hechten zich uitsluitend aan het substraat met behulp van adhesiemoleculen. Adhesiemoleculen verbinden zich op hun beurt met het cytoskelet, dat de vorm van de cel ondersteunt. Dit cytoskelet kan samentrekken, waardoor een trekkracht op het substraat ontstaat en de hele cel kan bewegen, vergeliikbaar met de spiercontractie van een slak. De samentrekking en dus de uitgeoefende trekkracht is een kenmerk van cellen. Spiercellen genereren bijvoorbeeld hoge krachten om bloed door aderen te pompen. Hier hebben we twee verschillende celtypes vergeleken op basis van hun trekkrachten en onderzocht hoe hun vorm hieraan gerelateerd is. Om de trekkrachten van cellen te meten, gebruikten we een specifiek hulpmiddel dat de micropilaarmatrix wordt genoemd. Micropilaar-matrices bestaan uit honderden kleine elastische pilaren die veel kleiner zijn dan de grootte van een cel. Wanneer een cel zich hecht aan een bed van micropilaren en de kracht begint uit te oefenen, buigen de balken. Deze buiging kan worden gemeten met microscopen en software die de doorbuiging van de pilaar omzetten in een kracht. In one experiment gebruikten we endotheel- en fibroblastcellen. Endotheelcellen vormen nauw verbonden tweedimensionale weefsels die bloedvaten omringen. Fibroblasten zijn op hun beurt beweeglijk, behouden de integriteit van weefsels en zijn dus betrokken bij weefselherstel. In onze studie toonden we aan dat endotheelcellen de helft van de tractiekrachten van fibroblasten op hun omgeving uitoefenen. Dit resultaat geeft de functie van de afzonderlijke celtypen weer. Omdat de cel-cel adhesie uitgesproken is in endotheelcellen voor weefselvorming, is de samentrekking van het cytoskelet op het cel-cel interface sterker dan bij de cel-substraatadhesie. Fibroblasten vereisen sterkere cel-substraat interacties om de omgeving van de cel te hermodelleren. We toonden verder aan dat de trekkrachtverdeling van endotheelcellen breder is en correleert met hun ronde morfologie, terwijl fibroblasten meer langwerpig zijn en de trekkrachten meer gelokaliseerd. We speculeren dat de correlatie van het krachtverdelingspatroon met cellulaire morfologie zou kunnen leiden tot het sturen van de richting van celbewegingen en collectief gedrag, een inzicht dat belangrijk kan zijn voor het mechanisme van cel- en weefselmigratie.

Tijdens dynamische processen zoals collectieve celmigratie ervaren cellen snelle veranderingen van spanning op hun cel-cel interface. Cel-cel adhesies moeten worden gevormd om losrakende krachten te weerstaan en de weefselintegriteit te behouden. De vragen hierbij zijn: wat is de maximale kracht die kan worden uitgeoefend om de cel-cel adhesie te verbreken en is deze te meten? Om deze vragen te beantwoorden, hebben we de micropilaar matrix-technologie verder ontwikkeld om cel-cel loslatingskrachten nauwkeurig te meten. In **Hoofdstuk 3** presenteerden we onze nieuwe technologie, het Cell-Cell Separation Device of kortweg CC-SD. De CC-SD bestaat uit dicht bij elkaar geplaatste micropilaar-matrixblokken waaraan cellen kunnen hechten en verbinding kunnen maken over de opening. Idealiter hechten twee cellen in een doubletconfiguratie zich aan de micropilaren. Het buigen van micropilaren wordt opnieuw gebruikt voor celtractiekrachtmetingen. De uitgeoefende krachten die het celdoublet omringen, moeten in evenwicht zijn met een mechanisch evenwicht. Als je de hand van iemand anders vasthoudt, voel je allebei de spanning in je armen, terwijl je stevig op je voeten staat zonder te bewegen. Deze spanning tussen cellen kan worden gemeten met behulp van micropilaren. We toonden aan dat de cel-cel adhesiekracht in dergelijke stabiele omstandigheden evenredig is met de totale uitgeoefende trekkracht op pilaren. Om het cel-cel contact te belasten, hebben we de blokken verbonden met een dunne laag eronder. Het uitrekken van de laag scheidt de blokken en verhoogt de spanning op de cel-cel adhesie. De spanning is voornamelijk gelokaliseerd bij het cel-cel contact en minder onder de cel door de blokken die voorkomen dat de pilaarvelden vervormen. In ons voorbeeld, wanneer de afstand tot de

andere persoon voor je toeneemt, neemt ook de spanning in je armen toe. Ook voel je meer spanning in je benen en oefen je meer weerstand uit op de grond. De toename van substraatkrachten die door cellen worden uitgeoefend, kan worden gemeten door de CC-SD en geeft informatie over de verhoogde spanning tussen cellen en laat zelfs het contact verbreken. Onze nieuw ontworpen CC-SD opent mogelijkheden voor het analyseren van celcel losmaakkrachten en werpt licht op de robuustheid van cel-cel adhesies in dynamische processen in weefselontwikkeling.

Zoals we hebben besproken in **Hoofdstuk 1**, ondergaan cellen in weefsels dynamische processen waarin cel-substraat en cel-cel verklevingen een rol spelen. De druk en spanning van naburige cellen veroorzaken vormveranderingen van individuele cellen en veroorzaken zelfs collectieve migraties binnen een weefsel. In een dicht opeengepakte metro, als je dicht bij de deur staat, de trein stopt en de deur gaat ineens open, heb je soms geen kans om in de wagon te blijven. Je wordt gedwongen om de stroom van de andere passagiers te volgen. Het collectieve gedrag en de richting van cellen zijn de huidige stand van het onderzoek en kunnen worden gevonden in een grote verscheidenheid aan systemen zoals wondgenezing, kankermetastase en embryonale ontwikkeling. Om de collectiviteit van cellen tijdens migratie te verklaren en te bestuderen, hebben wetenschappers voornamelijk gebruik gemaakt van een zogenaamde nematische symmetrie afgeleid van vloeibare kristallen, d.w.z. staafachtige structuren, in de fysica van zachte materie. Nematics beschrijft de oriëntatie en verlenging van cellen op eencellige schaal en hun uitlijning op grote schaal. De algehele uitlijning kan worden samengevat door een enkele waarde, de nematische ordeparameter, die aangeeft in welke maten cellen collectief in een bepaalde richting uitgericht zijn. Als je echter een weefsel van dichterbij bekijkt, zul je merken dat cellen niet altijd langwerpig zijn. Cellen kunnen een afgeronde vorm hebben en met hun buren georganiseerd zijn in een zeshoekig patroon waarin de afstanden tot alle zes buren bijna gelijk zijn. Het beschrijven van deze zes voorkeursrichtingen vereist een ander soort symmetrie, namelijk hexatische symmetrie. De beschrijving van cellen in monolagen op basis van nematische en hexatische orde was het onderwerp in Hoofdstuk 4. Door experimentele waarnemingen te combineren met numerieke simulaties, vergeleken we de hexatische en nematische orde van celsystemen over verschillende lengteschalen. Beginnend met het eencellige niveau, hebben we aangetoond dat cellen inderdaad een dominante hexatische orde hebben op eencellige schaal. Ze zijn eerder zeshoekig-rond dan langwerpig. Toen we naar de naaste buren van de cellen keken, zagen we dat het celsysteem overschakelde van hexatische naar nematische symmetrie door steeds meer naburige cellen te beschouwen. De resultaten toonden aan dat onze nieuwe benadering het naast elkaar bestaan van hexatische en nematische symmetrie op verschillende lengteschalen identificeerde. Het kennen van de juiste symmetrie van het systeem opent de mogelijkheden om de hiërarchische structuur van cellen in weefsels te bestuderen, hoe cellen coördineren en meercellige organisatie bereiken.

Meercellige organisatie is belangrijk in ontwikkelingsprocessen en komt voor bij uitzaaiingen van kanker. We hebben in **Hoofdstuk 2** al laten zien dat verschillende celtypen verschillende eigenschappen hebben in termen van morfologie vanwege hun trekkrachten en cel-cel adhesie. Het belangrijkste type weefsel in ons menselijk lichaam, dat alle oppervlakken bedekt, inclusief organen, zijn epitheelweefsels. Epithelia staan bekend om hun sterke cel-cel adhesie. Onder bepaalde omstandigheden kunnen epitheelcellen hun cel-cel adhesie verliezen, sterkere verklevingen aan het substraat ontwikkelen, mobiliteit krijgen en zelfs individueel worden. Dit proces wordt epitheliale-naar-mesenchymale transitie genoemd, waarbij cellen transformeren van epitheliale weefselcellen in invasieve en actieve mesenchymale cellen die betrokken zijn bij wondgenezing, fibrose en kankerprogressie. Tijdens deze processen verandert de hele meercellige organisatie. In **Hoofdstuk 4** hebben we laten zien dat de symmetrie van weefsels verschilt over verschillende lengteschalen en mogelijk verband houdt met meercellige organisatie. Hoe verandert de symmetrie wanneer cellen hun adhesie-eigenschappen en weefsels hun celdichtheid veranderen? We hebben deze vragen beantwoord in **Hoofdstuk 5** door epitheelcellen te vergelijken met mesenchymale cellen waarin, in tegenstelling tot epitheelcellen, alleen een specifiek type cel-cel adhesiemolecuul is verwijderd. Verwijdering van adhesiemoleculen leidt tot sterke vorming van het cytoskelet om cellulaire stabiliteit door het substraat te verkrijgen. Om ons voorbeeld van hierboven aan te halen, als je in de volle metro zit, houd je het evenwicht tussen de andere passagiers. Er is geen ruimte om te vallen. Wanneer er echter minder passagiers zijn, moeten jouw benen het overnemen en jouw evenwicht coördineren. In onze experimenten hebben we aangetoond dat mesenchymaal-achtige cellen inderdaad groter en meer gespreid zijn vanwege hun sterk ontwikkelde cytoskeletnetwerk. Toen we naar de symmetrie van individuele cellen in weefsels keken, ontdekten we dat cellen, onafhankelijk van het bestaan van het bepaalde type cel-cel adhesiemolecuul, en hoe ze ook samengedrukt worden, altijd een dominante hexatische ordening hebben. Ze zijn liever zeshoekig-rondachtig dan langwerpig en nematisch. Als we opnieuw naar steeds meer naburige cellen kijken, heeft de monolaag opnieuw een hogere en dominante nematische symmetrie. Deze cross-over,

d.w.z. het aantal beschouwde cellen, van hexatisch naar nematisch hangt wel af van de cel-cel adhesie. Het verwijderen van cel-cel adhesiemoleculen veroorzaakt een dominante nematische organisatie in meercellige systemen op grote schaal. Cellen met sterke cel-cel contacten behouden hun hexatische organisatie voor iets langere lengteschalen. Dit geldt ook voor monolagen met een hogere celdichtheid. Deze resultaten geven aan dat het samenspel tussen cel-substraat en cel-cel adhesie de lengteschaal van de hexatische symmetrie regelt.

Er blijven echter veel vragen over. Is het mogelijk om visueel waarneembare kenmerken van cellen, zoals weefselsymmetrie, collectieve migratie en celvormveranderingen, te bestuderen en deze informatie te gebruiken om intercellulaire mechanismen te identificeren? Kunnen we de 'symptomen' van cellen bestuderen om de juiste 'diagnose' van verstoorde weefselorganisatie te krijgen? Kunnen we een patroon identificeren en zelfs collectief celgedrag en daarmee ontwikkelingsprocessen voorspellen?

Vragen op vragen. Als je niet bent gestopt met lezen of in slaap bent gevallen, hoop ik je ervan te hebben overtuigd dat dit proefschrift een hoofdstuk opent om deze vragen te beantwoorden. We toonden aan dat celmechanica en geometrische eigenschappen zoals cel- en weefselsymmetrie informatie verschaffen over intercellulaire processen en cel-cel interacties op moleculaire schaal. Het combineren van de knowhow van verschillende onderzoeksdisciplines is essentieel voor waterdicht onderzoek en opent mogelijkheden om alle resultaat-stukken van de onderzoekspuzzel aan elkaar te koppelen om het grote geheel te completeren.

Julia Eckert

# Zusammenfassung

Was haben Wale, Schnecken, Menschen, Pflanzen und alle anderen Lebewesen gemeinsam? Wir alle bestehen aus den gleichen Bausteinen, den Zellen. Billionen von Zellen, die gerade einmal eine Größe von wenigen Mikrometern haben, bilden ein Netzwerk und formen zum Beispiel die Organe unseres menschlichen Körpers und deren umgebende Struktur. Zellen haben ihren eigenen Lebenszyklus, kommunizieren und koordinieren sich miteinander, was am Ende unsere Individualität als Mensch ausmacht. Allein die Tatsache, dass du dieses Buch geöffnet und hoffentlich Spaß beim Lesen hattest, verdankst du deinem Netzwerk von Zellen.

Was ist das Geheimnis von diesem Netzwerk, das unser Leben durch diese kleinen Zellen ermöglicht? Im Grunde genommen ist das Zellnetzwerk nicht so sehr verschieden von den Strukturen unserer Gesellschaft. Wir tendieren immer noch dazu, Menschen nach ihrem Geschlecht, Herkunft und kulturellem Hintergrund einzuordnen, auch wenn wir im Grunde alle gleich sind. Zellen werden zum Beispiel nach ihrer molekularen Struktur oder ihren Eigenschaften klassifiziert, wie in Stammzellen, Hautzellen, Muskelzellen und Lungenzellen. Wir Menschen sind täglich in Kontakt miteinander, sei es in der Schlange an der Kasse im Supermarkt, beim Einstieg in eine überfüllte U-Bahn, bei der Überquerung einer Brücke oder im Fußballstadium. Dennoch sind wir auch unabhängig und können alleine unsere Privatsphäre genießen. Das Gleiche trifft auch bei Zellen zu. Sie bilden Strukturen und formen Gewebe wie Blutgefäße und Organe, treten mit ihrer nichtzellularen Umgebung in Kontakt und bewegen sich einzeln oder als Verband wie es zum Beispiel bei Metastasen der Fall ist. Wir sehen also, dass die Wahrnehmung der Umgebung, die Kommunikation, Koordination und die Gemeinschaft eine große Rolle in verschiedenen Größenordnungen spielen. Meine Doktorarbeit spiegelt solche Themen wider und umfasst die Bereiche der Zellbiologie, der biologischen Physik und weichen Materie. Sie kombiniert dabei experimentelle Beobachtungen mit theoretischen Beschreibungen.

Die Entstehung und die Rolle der Interaktionen zwischen Zellen wurde in den letzten Jahrzehnten breit diskutiert und ist noch immer in verschiedenen Bereichen ein aktueller Forschungsgegenstand der heutigen Wis-Während Physikerinnen und Physiker die Zell-Zell-Adhäsion durch Spannungen, Kräfte, Drücke und ausgeübten Stress an deren Grenzflächen beschreiben, studieren Biologen und Biologinnen ihre molekulare Beschaffenheit und die Mechanismen, die in den Zellen stattfinden. Einige Moleküle, die sich in der Membran befinden, verbinden Zellen miteinander oder Zellen mit deren nichtzellulären Umgebung, während andere Moleküle das Zellskelett bilden und wiederum andere alle internen Komponenten verknüpfen. In Kapitel 1 haben wir uns diesem Thema gewidmet und eine Definition der Zell-Zell-Adhäsion auf der Basis biologischer und physikalischer Erkenntnisse zusammengetragen. Wenn Zellen in Kontakt miteinander sind, erfahren sie Drücke und Spannungen von ihren Nachbarn, wie es Menschen erleben, wenn sie gequetscht in einer U-Bahn stehen und bei jeder Kurve aneinander stoßen. Zellen sind in der Lage, auf die Wechselwirkungen mit ihrer Umgebung und anderen Zellen zu reagieren. Jede Wechselwirkung ruft einen internen Prozess hervor. Dabei setzen sich Moleküle in Bewegung und gelangen an die Zell-Membran, wo sie gebraucht werden, um deren Stabilität zu unterstützen oder sie verändern das Zellskelett und damit die Form der Zelle. Somit erzeugt jede erfahrene Reaktion eine Gegenreaktion. Die erzeugten Veränderungen der Zell-Zell-Adhäsion gehen somit mit Änderungen von der Zellform, Koordination und dem kollektiven Verhalten von Zellen einher.

In Kapitel 2 haben wir die Wechselwirkungen von einzelnen Zellen mit ihrer nichtzellularen Umgebung untersucht. Dabei unterscheidet sich die interne Struktur einzelner Zellen von der von verbundenen Zellen. Einzelne Zellen haften sich nur mit der Hilfe von Adhäsionsmolekülen an das Substrat. Die Adhäsionsmoleküle wiederum verbinden sich mit dem Zellskelett, welches die Zellform unterstützt. Dieses Zellskelett ist in der Lage, sich zusammenzuziehen, wodurch eine Zugkraft auf das Substrat wirkt, was wiederum der Zelle erlaubt, sich zu bewegen. Dieser Mechanismus ähnelt dem der Schnecke, wenn ihre Muskeln sich kontrahieren, um vorwärts zu gelangen. Die Kontraktion und die damit aufgebrachte Zugkraft ist eine Eigenschaft von Zellen. So erzeugen beispielsweise Muskelzellen hohe Kontraktionskräfte, um Blut durch die Venen zu pumpen. In unserem Experiment haben wir zwei verschiedene Zelltypen anhand ihrer Zugkräfte verglichen und untersucht, wie ihre Form damit zusammenhängt. Um die Zugkräfte von Zellen zu messen, verwendeten wir ein spezielles Werkzeug, ein so genanntes Mikrosäulen-Array. Mikrosäulen-Arrays bestehen aus Hunderten von winzigen elastischen Balken, die viel kleiner sind als die Zelle. Wenn eine Zelle sich auf einem Bett aus Mikrosäulen haftet und beginnt, an diesem Balken Zugkräfte auszuüben, biegen sich diese. Diese Biegung kann mit Hilfe von Mikroskopen gemessen und durch Programme in eine Kraft umgerechnet werden. In unserem Experiment verwendeten wir Endothel- und Fibroblastenzellen. Endothelzellen bilden eng verbundene zweidimensionale Gewebe, die Blutgefäße umgeben. Fibroblasten hingegen sind beweglich, erhalten die Integrität von Geweben aufrecht und sind somit an der Gewebereparatur beteiligt. Wir haben gezeigt, dass Endothelzellen im Vergleich zu Fibroblasten nur halb so viel Zugkraft auf ihre Umgebung ausüben. Dieses Ergebnis spiegelt die Eigenschaften der einzelnen Zelltypen wider. Da die Zell-Zell-Adhäsion in Endothelzellen zur Gewebebildung ausgeprägter ist, zieht sich das Zellskelett an der Zell-Zell-Verbindungsfläche stärker zusammen als an der Zell-Substrat-Fläche. Fibroblasten hingegen benötigen stärkere Zell-Substrat-Wechselwirkungen, um das Bindegewebe aufzubauen und geschädigtes abzubauen. Wir haben weiterhin gezeigt, dass sich die Zugkräfte von Endothelzellen mehr verteilen und durch ihre rundliche Form gleichmäßiger verteilt sind, während Fibroblasten lang gestreckt und die Zugkräfte dadurch lokalisierter sind. Wir vermuten, dass die Korrelation zwischen der Verteilung der ausgeübten Zugkräfte mit der Zellform dazu dient, die Richtung der Bewegungen und das kollektive Verhalten von Zellen im Gewebe zu steuern.

In dynamischen Prozessen wie der kollektiven Zellbewegung kommt es sehr schnell zu Spannungsänderungen an der Zell-Zell-Kontaktfläche. Neue Zell-Zell-Adhäsionen müssen gebildet werden, um Trennungen von Zellverbänden zu vermeiden und die Integrität des Gewebes aufrechtzuerhalten. Dadurch ergeben sich folgende Fragen: Was ist die maximale Kraft, die aufgebracht werden kann, um die Zell-Zell-Adhäsion zu brechen, und kann diese gemessen werden? Zur Beantwortung dieser Fragen haben wir die Mikrosäulen-Array-Technologie weiterentwickelt, um die beteiligten Kräfte an der Trennung von Zellen genauer zu messen. In Kapitel 3 haben wir unsere neue Technologie, das Zell-Zell-Trennverfahren oder im Englischen das Cell-Cell Separation Device (CC-SD), vorgestellt. Das CC-SD besteht aus eng benachbarten Blöcken, auf denen sich die Mikrosäulen befinden. Es erlaubt den Zellen sich an die Spitzen der Säulen zu heften und sich über die Lücke zwischen den Blöcken miteinander zu verbinden. Idealerweise handelt es sich dabei um zwei Zellen. Die Biegung der Mikrosäulen gibt auch hier wieder Aufschluss über die aufgewendeten Zugkräfte. Die Kräfte befinden sich dabei in einem mechanischen Gleichgewicht und addieren sich zu null. Wenn du die Hände einer anderen Person ergreifst, spürst du dabei die Spannung in deinen Armen, stehst jedoch fest auf deinen Beinen, ohne dich zu bewegen. Diese Spannung zwischen den Zellen kann durch die

Mikrosäulen gemessen werden. Wir haben gezeigt, dass sich die Zell-Zell-Adhäsionskräfte unter solchen Gleichgewichtsbedingungen gleichmäßig mit der gesamten aufgebrachten Zugkraft erhöht. Um eine Spannung an dem Zell-Kontakt hervorzurufen, haben wir die Blöcke mit einer dünnen Schicht verbunden. Im Experiment wird diese Schicht gedehnt, was den Abstand der Blöcke erhöht. Dabei lokalisiert sich die erzeugte Spannung hauptsächlich am Zell-Zell-Kontakt und lässt die Zellen auf den Blöcken nahezu unberührt. In unserem Beispiel nimmt die Spannung in deinen Armen zu, wenn du die Händen der anderen Personen hältst und Schritt für Schritt zurück gehst. Außerdem übst du dabei einen größeren Wiederstand mit deinen Beinen auf den Boden aus. Die Erhöhung der von den Zellen auf das Substrat aufgebrachten Zugkräfte kann von unserem CC-SD gemessen werden. Es gibt Auskunft über die schrittweise erhöhte Spannung zwischen den Zellen und trennt sogar den Zell-Zell-Kontakt. Unser neu entwickeltes CC-SD eröffnet Möglichkeiten zur Analyse von maximalen Adhäsionenskräften, welche Zellen im Gewebe aushalten können und gibt Aufschluss über die Robustheit von Zell-Zell-Adhäsionen während dynamischer Prozesse in der Gewebeentwicklung.

Wie wir bereits in **Kapitel 1** besprochen haben, durchlaufen Zellen in Geweben dynamische Prozesse, bei denen Zell-Substrat- und Zell-Zell-Adhäsionen eine wichtige Rolle spielen. Die Drücke und Spannungen von benachbarten Zellen verursachen Formveränderungen einzelner Zellen und treiben sogar kollektive Zellbewegungen innerhalb eines Gewebes voran. Wenn du in einer dicht gedrängten U-Bahn in der Nähe einer Tür stehst, der Zug anhält und die Tür plötzlich aufgeht, hast du manchmal keine Chance, im Wagen zu bleiben. Du bist gezwungen, dem Strom der anderen Passagiere zu folgen. Das kollektive Verhalten und die gemeinschaftliche Ausrichtung von Zellen sind aktueller Forschungsgegenstand und finden sich in den unterschiedlichsten Systemen wie bei der Wundheilung, Krebsmetastasierung und der Embryonalentwicklung wieder. Um die Kollektivität von Zellen während der Bewegung zu erklären und zu untersuchen, haben Wissenschaftler in der Physik der weichen Materie hauptsächlich die sogenannte nematische Symmetrie verwendet, die von Flüssigkristallen, d.h. stäbchenförmigen Strukturen, abgeleitet ist. Die Nematik beschreibt die Orientierung und Ausdehnung von einzelnen Zellen und ihre kollektive Ausrichtung auf globaler Ebene. Die kollektive Ausrichtung kann durch einen einzigen Wert beschrieben werden, dem nematischen Ordnungsparameter. Dieser stellt dar, wie gleichmäßig alle Zellen ausgerichtet sind. Wenn du dir ein Zellgewebe jedoch genauer ansiehst, stellst du fest, dass Zellen nicht immer länglich sind. Zellen können eine abgerundete Form haben und sich gemeinsam mit ihren Nachbarn in einem sechseckigen Muster ausrichten, in dem die Abstände zu allen sechs Nachbarn nahezu gleich sind. diese sechs Vorzugsrichtungen zu berücksichtigen, bedarf es einer anderen Art von Symmetrie, nämlich der hexatischen Symmetrie. Die Beschreibung von Zellen in zweidimensionalen Schichten basierend auf der nematischen und hexatischen Ordnung war das Thema in Kapitel 4. kombinierten experimentelle Beobachtungen mit numerischen Simulationen und verglichen die hexatische und nematische Ordnung von Zellsystemen über verschiedene Längenskalen hinweg. Auf der Einzelzellebene haben wir gezeigt, dass Zellen tatsächlich eine dominante hexatische Ordnung haben. Sie sind eher sechseckig-rundlich als länglich. Als wir die Zellen ihrer nächsten Nachbarn mit in Betracht zogen, sahen wir, dass das Zellsystem von der hexatischen zur nematischen Symmetrie wechselte, je mehr benachbarte Zellen berücksichtigt wurden. Die Ergebnisse zeigten, dass unser neuartiger Ansatz die Koexistenz von hexatischer und nematischer Symmetrie auf unterschiedlichen Längenskalen identifiziert. Die Kenntnis der korrekten Symmetrie des Systems eröffnet die Möglichkeit, die hierarchische Struktur von Zellen in Geweben zu untersuchen, wie Zellen sich koordinieren und eine multizelluläre Organisation erreichen.

Die multizelluläre Organisation ist wichtig für Entwicklungsprozesse und kommt in Krebsmetastasen vor. Wir haben bereits in Kapitel 2 gezeigt, dass verschiedene Zelltypen aufgrund ihrer Zugkräfte und Zell-Zell-Adhäsion unterschiedliche morphologische Eigenschaften haben. Der wichtigste Gewebetyp in unserem menschlichen Körper, der alle Oberflächen einschließlich der Organe bedeckt, ist das Epithelgewebe. Epithelien sind für ihre starke Zell-Zell-Adhäsion bekannt. Unter bestimmten Umständen können Epithelzellen ihre Zell-Zell-Adhäsion verlieren, stärkere Adhäsionen zum Substrat entwickeln, an Mobilität gewinnen und sogar vereinzelt auftreten. Dieser Prozess wird als Epithel-Mesenchym-Übergang bezeichnet, bei dem sich Zellen von epithelialen Gewebezellen in invasive und mobile mesenchymale Zellen verwandeln, die an der Wundheilung, Fibrose und Krebsentstehung beteiligt sind. Während dieser Prozesse verändert sich die gesamte multizelluläre Organisation. In Kapitel 4 haben wir gezeigt, dass die Symmetrie von Geweben auf verschiedenen Längenskalen unterschiedlich ist und möglicherweise mit der multizellularen Organisation zusammenhängt. Wie verändert sich die Symmetrie des Gewebes, wenn Zellen ihre Adhäsionseigenschaften und Gewebe ihre zelluläre Kompaktheit ändern? Diesen Fragen sind wir in Kapitel 5 nachgegangen, indem wir Epithelzellen mit mesenchym-ähnlichen Zellen verglichen haben. Bei den mesenchym-ähnlichen Zellen sind im Gegensatz zu Epithelzellen nur eine bestimmte Art von Zell-Zell-Adhäsionsmolekülen entfernt worden. Die Entfernung der Adhäsionsmoleküle führt zu einer starken Ausbildung des Zellskeletts, um die Stabilität der Zelle auf dem Substrat zu erhöhen. Um bei unserem obigen Beispiel zu bleiben: Wenn du in einer überfüllten U-Bahn stehst, hältst du das Gleichgewicht durch die anderen Fahrgäste. Es gibt keinen Platz zum Hinfallen. Wenn jedoch weniger Fahrgäste anwesend sind, müssen deine Beine das Gleichgewicht halten und koordinieren. In unseren Experimenten konnten wir zeigen, dass mesenchymal-ähnliche Zellen aufgrund ihres stark ausgeprägten Zellskelett-Netzwerks größer sind und sich tatsächlich stärker ausbreiten. Als wir die Symmetrie der einzelnen Zellen im Gewebe untersuchten, stellten wir fest, dass die Zellen unabhängig von der Existenz des bestimmten Typs von Zell-Zell-Adhäsionsmolekülen eine dominante hexatische Anordnung aufweisen. Dies ist auch der Fall, unabhängig davon, wie stark sie im Gewebe zusammengedrückt sind. Die Zellen ziehen es vor, hexagonal-rundlich zu sein, anstatt länglich und nematisch. Betrachtet man wiederum mehr und mehr benachbarte Zellen, so weist die zweidimensionale Schicht wiederum eine höhere und dominante nematische Symmetrie auf. Dieser Übergang von hexatisch zu nematisch, d. h. wie viele benachbarte Zellen berücksichtigt werden, hängt von der Zell-Zell-Adhäsion ab. Das Entfernen von Zell-Zell-Adhäsionsmolekülen führt zu einer dominanten nematischen Organisation in multizellulären Systemen auf globaler Ebene und ihre geminschaftliche Ausrichtung dominiert. Zellen mit starken Zell-Zell-Kontakten behalten ihre hexatische Organisation für etwas längere Längenskalen bei. Dies gilt auch für zweidimensionale Schichten mit höherer Zelldichte. Diese Ergebnisse deuten darauf hin, dass das Zusammenspiel von Zell-Substrat- und Zell-Zell-Adhäsion die Längenskala der hexatischen Symmetrie kontrolliert.

Es bleiben jedoch viele Fragen offen. Ist es möglich, optische Merkmale von Zellen wie die Gewebesymmetrie, die kollektive Bewegung und Zellformänderungen zu untersuchen und diese Informationen zu verwenden, um interzelluläre Mechanismen zu identifizieren? Können wir die 'Symptome' von Zellen untersuchen, um die korrekte 'Diagnose' einer gestörten Gewebeorganisation zu erhalten? Können wir ein Muster erkennen und sogar das kollektive Verhalten von Zellen und damit verschiedene Entwicklungsprozesse vorhersagen?

Fragen über Fragen. Wenn du nicht aufgehört hast zu lesen und immer noch wach bist, hoffe ich, dich davon überzeugt zu haben, dass diese Doktorarbeit ein Kapitel zur Beantwortung dieser Fragen eröffnet. Wir haben gezeigt, dass die Zellmechanik und die geometrischen Eigenschaften

wie die Zell- und Gewebesymmetrie Informationen über die interzelluläre Prozesse und der Zell-Zell-Interaktionen auf molekularer Ebene liefern. Das Verbinden von Wissen aus verschiedenen Forschungsdisziplinen ist für eine lückenlose Forschung unerlässlich und eröffnet Möglichkeiten, alle Puzzlestücke der Wissenschaft zu einem Gesamtbild zusammenzufügen.

Julia Eckert

### **Publications**

- (1) **Eckert, J.**, Ladoux, B., Giomi, L., Schmidt, T. (2022). Hexanematic crossover in epithelial monolayers depends on cell adhesion and cell density. bioRxiv 2022.10.07.511294.
- (2) Hoffmann, L. A., Carenza, L. N., **Eckert, J.**, and Giomi L. (2022). Theory of defect-mediated morphogenesis. *Science Advances* 8, eabk2712.
- (3) Armengol-Collado, J.-M.\*, Carenza, L. N.\*, **Eckert**, **J.\***, Krommydas, D.\*, and Giomi, L. (2022). Epithelia are multiscale active liquid crystals. arXiv:2202.00668.
- (4) Rodrigues de Mercado, R., van Hoorn, H., de Valois, M., Backendorf, C., **Eckert**, **J.\***, and Schmidt, T.\* (2022). Characterization of cell-induced astigmatism in high-resolution imaging. *Biomed. Opt. Express* 13, 464-473.
- (5) **Eckert, J.\***, Abouleila, Y.\*, Schmidt, T., and Mashaghi, A. (2021). Single Cell Micro-Pillar-Based Characterization of Endothelial and Fibroblast Cell Mechanics, *Micro* 1, 242-249.
- (6) Arslan, F. N.\*, **Eckert, J.\***, Schmidt, T., and Heisenberg, C.-P. (2021). Holding it together: when cadherin meets cadherin. *Biophysical Journal* 120, 4182-4192.
- (7) Eckert J., van Loon, J. J. W. A., Eng, L. M., and Schmidt T. (2021). Hypergravity affects cell traction forces of fibroblasts. *Biophysical Journal* 120, 773-780.
- (8) Woodcock, E. M., Girvan, P., Eckert, J., Lopez-Duarte, I., Kubánková, M., van Loon, J. J. W. A., Brooks, N. J., and Kuimova, M. K. (2019). Measuring Intracellular Viscosity in Conditions of Hypergravity. Biophysical Journal 116, 1984-1993.

<sup>\*</sup> Equal contribution

# Curriculum Vitae

From 2023	Postdoctoral research position Alpha Yap Lab – Institute for Molecular Bioscience, University of Queensland, Australia
2018 – 2022	Ph.D. in mechanobiology   cell- and tissue mechanics Thomas Schmidt Lab – Physics of Life Processes, Leiden Institute of Physics, Leiden University, The Netherlands
08/2021 - 01/2022	Visiting student & EMBO Scientific Exchange Fellow Benoît Ladoux / René-Marc Mège Lab – Cell Adhesion & Mechanics, Institut Jacques Monod - Université Paris Diderot / CNRS, France
10/2015 - 09/2018	<ul> <li>M.Sc. in Physics</li> <li>Technische Universität Dresden, Germany</li> <li>Specialization: Soft condensed matter and biological physics</li> <li>Thesis: 'Influence of Hypergravity on Cell Traction Forces of 3T3 Fibroblasts'</li> </ul>
07/2017 – 08/2018	Internship Thomas Schmidt Lab – Physics of Life Processes, Leiden Institute of Physics, Leiden University, The Netherlands - Master thesis project in collaboration with with TU Dresden and ESA/ESTEC - Funding: ERASMUS+ of the European Union

152 Curriculum Vitae

#### 07/2017 – Internship

O1/2018 Physical Science Instrument Section, Mechatronics & Optics Division, Mechanical Engineering Department, Directorate of Technology, Engineering and Quality, European Space Agency (ESA)/ European Space Research and Technology Centre (ESTEC), The Netherlands

- Master thesis project in collaboration with TU Dresden and Leiden University
- Funding: ERASMUS+ of the European Union

#### 07/2016 - Student assistant

12/2016 Stefan Diez Group – Biophysics of Single Motor Proteins, B CUBE – Center of Molecular Bioengineering at TU Dresden, Germany

#### 08/2015 – Internship

Diology & Env. Monitoring Science Office, Science Department, Directorate Human Spaceflight & Operations, European Space Agency (ESA)/ European Space Research and Technology Centre (ESTEC), The Netherlands

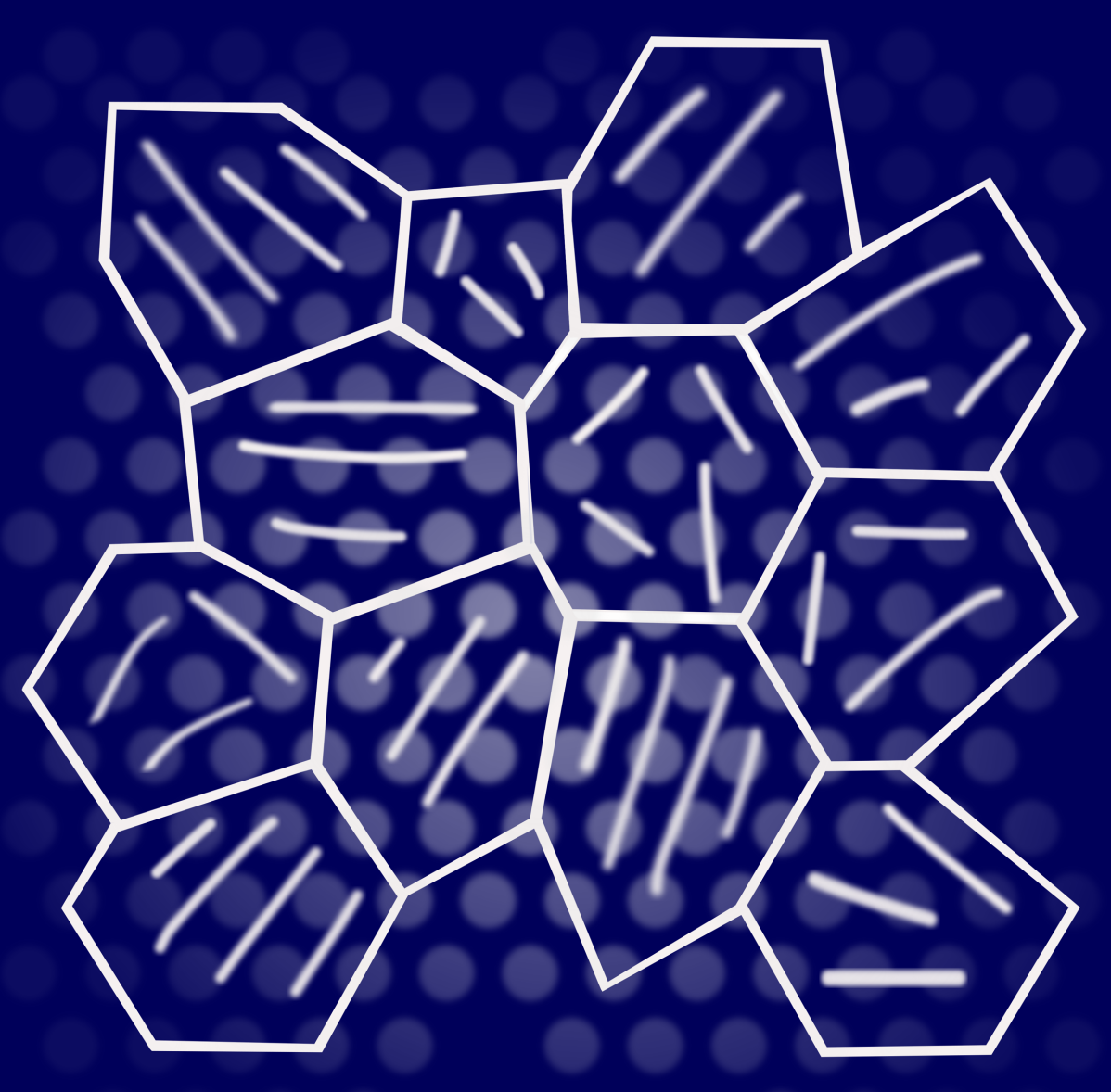
- Contributed to the Bio-X experiment | measurements of cell height changes under hypergravity and microgravity conditions
- Participated in the 63rd ESA parabolic flight campaign, granted by the European Low Gravity Research Association (ELGRA)

#### 10/2011 – B.Sc. in Physics

09/2015 Technische Universität Dresden, Germany Thesis: 'Indirect determination of Jupiter's position using gravitational light deflection as part of ESA's Gaia space mission'



The interplay between cell-substrate and cell-cell adhesion regulates the arrangement, shape, and topology of cells and tissues. This thesis covers topics ranging from method development to combining experimental observations with theoretical descriptions.



ISBN 978-90-8593-536-0 Casimir Series 2022-28